INTRINSIC AND SYNAPTIC MEMBRANE RESPONSES OF MURINE SPIRAL GANGLION NEURONS

by

WENKE LIU

A dissertation submitted to the

Graduate School-New Brunswick

Rutgers, The State University of New Jersey

and

The Graduate School of Biomedical Sciences

In partial fulfillments of the requirements

For the degree of

Doctor of Philosophy

Graduate Program in Neuroscience

Written under the direction of

Robin L. Davis, PhD

And approved by

_____

_____

_____

_____

_____

New Brunswick, New Jersey

OCTOBER 2015

ABSTRACT OF THE DISSERTATION

Intrinsic and Synaptic Membrane Responses of Murine Spiral Ganglion Neurons

by WENKE LIU

Dissertation Director:

Robin L. Davis, PhD

As the first neuronal element in the auditory pathway, spiral ganglion neurons are responsible for the initial signal encoding of complex sound information. Experiments presented in this dissertation explore the physiological basis of coding capacity in the murine postnatal spiral ganglion using electrophysiological and immunocytochemical techniques. Three separate and complete studies are presented. First, heterogeneity within each tonotopic region of the ganglion was characterized by the distribution patterns of calretinin and calbindin, two widely used markers for neuronal subpopulations (Liu and Davis, 2014). Second, the developmental establishment of diverse firing patterns in the spiral ganglion was investigated in embryonic cochlear epithelial cells in which neurogenic transcription factors were overexpressed (Nishimura et al., 2014). Finally, recordings made from acute cochlear whole-mounts preparations were made to assess the diverse intrinsic firing features in comparison to invading action potentials and passively-propagated synaptic potentials (Liu and Davis, in preparation). Results from

these studies suggest that the physiological heterogeneity within the spiral ganglion may contribute to a population code essential for conveying the rich content of auditory information.

Acknowledgements

Throughout the years of my graduate study I have received tremendous help from mentors, collaborators and colleagues, without whom this dissertation could never be possible. I could only try my best here to express my deep gratitude to them.

My dissertation committee members, Drs. Mark Plummer, Cheryl Dreyfus, Mengqing Xiang and Elizabeth Olson provided me with suggestions and guidance all the way through. It was a great fortune of me to have their insights and good judgment on my side.

I'm grateful to Drs. Kenneth Paradiso, Shu-Chan Hsu and Lunjun Wu in the department of neuroscience and cell biology at Rutgers University. They have shared with me their expertise and experiences, on science and broader topics as well. I learned a lot from them and enjoyed the conversations with them outside the seminar rooms, in the hallway and beside the water fountain. I also benefited greatly from my experience as a teaching assistant for the Advance Neurobiology Lab course Drs. Plummer and Paradiso instructed. I heartily appreciate this opportunity they have provided me. As the physicist John Wheeler put it, one can only learn by teaching.

My gratitude also goes to the Neuroscience graduate program, particularly to Dr John Pintar and Ms Joan Mordes, who have been extremely supportive throughout my study. Ms Virgina Marano and Ms Pamela Woronoff in the department chairman's office

and Ms Jana Curry in the office of undergraduate instructions have guided me through the labyrinth of paper work, and their help is much appreciated.

I'm also indebted to Dr Alain Dabdoub at Toronto University, Canada. Chapter 4 of this dissertation presents the results of our fruitful collaboration, which was also a great learning experience for me.

Current and former members of the Davis lab have been as helpful as one could ever hope. Drs. Robert Crozier and Qing Liu initiated the project that comprises Chapter 5 of this dissertation. They have generously shared with me their experimental tricks and professional experiences, which I would rely on even in the days to come. For years I have worked alongside Drs. Felicia Smith and John Chen and learned the nuts and bolts of image analysis from them. Lab technician Huizhong (Susan) Xue is the master hand behind all tissue preparations, and I, as everybody else, deeply appreciate her generosity and caring nature. Qing (Sarah) Hsu and Anna Hader in the Plummer lab would kindly offer their help whenever I asked for it. I have enjoyed the time I spent in the Davis lab and will always remember everyone I met here as great colleagues and good friends.

My advisor Dr Robin L. Davis brought to me the best of everything the word 'mentor' stands for. If in the end of my graduate study I start to understand what research is all about, it is only possible with her training, and it is only through her example that I recognize the hard working and hard thinking required for the scientific endeavor. As a scientist she pays attention to the details while at the same time never loses sight of the big picture. I will always bear her advice in mind and see her as my role model.

Finally I would like to thank my family and friends, whose unconditional support helped me get through moments of frustration, anguish and self-doubt, which is just an unavoidable part of every graduate experience. I would like to dedicate this dissertation to my grandparents, Professors Bicheng Xie and Shifang Shen, who enlightened me, early in my childhood, that the search for knowledge is one of the things that make a life worth living.

Table of Contents

List of Tables

List of Figures

Chapter 1

Introduction

Perception of the external world begins with the transduction of physical stimuli into neural signals, which are then relayed through sophisticated pathways ascending to higher brain centers. Contrary to the naïve view that signals are transmitted faithfully but passively, efforts in the field of sensory neuroscience have demonstrated that at each step along the afferent pathway, intensive coding and processing were carried out by neurons with diverse cellular properties and connection patterns. The infrastructure of sensory pathways, therefore, shapes the information even before it reaches the brain, and mechanisms of signal processing are implemented at the very initial steps in these pathways.

In the mammalian auditory system, the analytical processing of input begins at the peripheral hearing organ, the cochlea. Within this snail-shaped bony structure, the cochlear duct, which spirals from the base to the apex, is partitioned into three compartments: scala vestibuli, scala media and scala tympani. Scala vestibuli and scala tympani connect at the apex of the cochlea, and scala media between them encapsulates the auditory sensory receptors and primary neurons (Slepecky, 1996). After sound waves were captured by the external ear, the tympanum and the ossicles in the middle ear transmit the mechanical energy to oval window at the base of cochlea, which in turn pass

the vibration to the fluid-filled cochlear duct and cause movement of basilar membrane, and excite the hair cell receptors residing on it (Robles and Ruggero, 2001). When activated by displacement, the hair cells release glutamate and depolarize the fiber terminals of spiral ganglion neurons, which code the acoustic stimuli into firing of action potentials and relay the information to the brain (Glowatzki and Fuchs, 2002).

There are two categories of hair cell receptors and two corresponding classes of spiral ganglion neurons. Inner hair cells that are aligned in one single row on the modiolar side of the basilar membrane each connects with 10~30 type I spiral ganglions, which comprise about 95% of the neuronal population, each innervating their targets in a one-to-one manner. The remaining 5% of the ganglion is composed of type II spiral ganglion neurons, which extend their peripheral fibers to three rows of outer hair cells to form *en passant* synapses on multiple targets (Berglund and Ryugo, 1987; Ryugo, 1992). Thus the type I and type II spiral ganglion neurons innervate their receptors with divergent and convergent patterns, respectively, and form separate pathways for auditory information. Type I and type II neurons differ morphologically and functionally. For example, type I myelinated neurons have a bipolar shape and are primarily responsible for the sensation of sound stimuli (Liberman, 1982; Keithley and Schreiber, 1987; Ruggero, 1992). In contrast, unmyelinated type II neurons are pseudo-monopolar; their sensory contribution, still under dispute, extends from threshold detection to pain perception (Robertson, 1984; Brown, 1994; Reid et al., 2004; Weisz et al., 2009). A

recent investigation utilizing a mouse model that lacked type II neurons suggested that type II afferents may be part of the feedback loop controlling the cochlear amplifier gain (Froud et al., 2015).

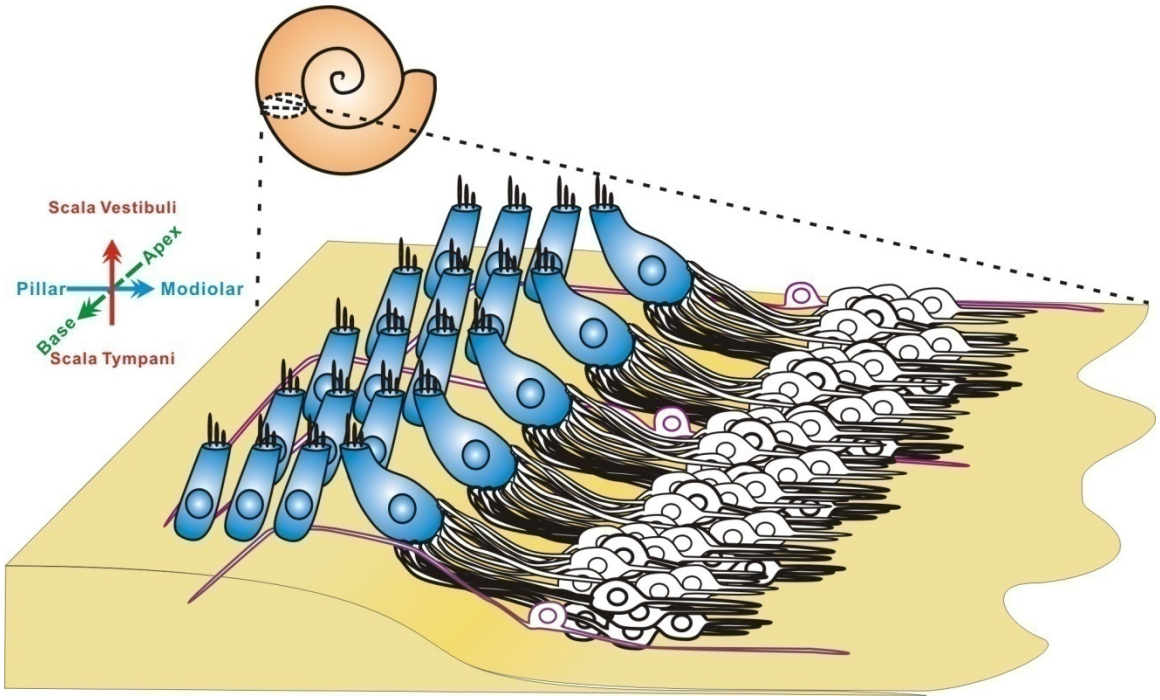

Figure 1.1: Anatomy of mammalian cochlea. Schematic of the cochlear duct showing the anatomical organization in the sensory receptors and spiral ganglion neurons. One row of inner hair cells are innervated by the bipolar type I spiral ganglion neurons (white) and three row of outer hair cells connect with the pseudomonopolar type II spiral ganglion neurons (gray). Cell bodies of type I fibers that innervate the hair cells on the pillar side cluster on the scala tympani side of the ganglion and have thicker axon diameter.

One challenge imposed on all sensory systems is to reflect different aspects of the stimulus by conveying information with different sub-modalities (Gardner and Martin, 2000). For auditory system, the perception of sound involves major sub-modalities such as pitch, loudness, timbre and location (Bizley and Walker, 2010), all of which are spectral- and temporal-related, and may require complex central processing as well as detailed peripheral encoding. Ever since the seminal work by Georg von Békésy (von Békésy, 1970), mechanisms that contribute to the coding of frequency information in the cochlea have been relatively well-understood. It was demonstrated that the mechanical properties of basilar membrane are graded systematically from the base to the apex of the cochlear duct, thus sound vibration produces traveling waves in the basilar membrane, such that different frequency tones induce maximum displacement in separable locations. As a result the cochlea functions as a frequency analyzer, such that the frequency spectrum of sound stimuli is coded in a spatial map in the cochlear duct with the apex responding optimally to low frequency sound and the base responding optimally to high frequency sound (Robles and Ruggero, 2001). Recordings made *in vivo* from cat auditory nerve axons have revealed that each auditory nerve fiber is most sensitive to sound stimuli with a specific frequency, termed the characteristic frequency (Kiang, 1965). The properties of hair cells and the ribbon synapses between hair cells and spiral ganglion neurons are also tuned accordingly along the cochlea to respond optimally to a defined frequency sound (Slepecky, 1996; Meyer et al., 2009). The tonotopic organization established in the cochlea is retained in every relay station along the auditory pathway

(Reale and Imig, 1980; Kandler et al., 2009; Mann and Kelley, 2011) .

The initial coding of loudness, or sound intensity information also occurs in the cochlea. Auditory nerve fibers have been shown to discharge spontaneously without applied sound stimuli (Kiang, 1965). The spontaneous firing rate of multiple fibers showed high, medium and low levels across the characteristic frequency range, and correlation was observed between spontaneous rate and other intensity-related properties of the nerve fiber, such as threshold and dynamic range (Liberman, 1978; Taberner and Liberman, 2009). Overall, fibers with higher levels of spontaneous activity exhibited lower levels of threshold, and this results in categories of fibers that form different pathways with high and low sensitivity to sound intensity levels, respectively, which are all responsible for the transduction of the same pitch. Further studies showed that the difference between the two intensity groups is associated with morphological features. The high-spontaneous rate fibers have a larger diameter and contact the hair cells on the side facing the pillar cells, whereas the low and medium-spontaneous rate fibers are smaller and innervate hair cells at the modiolar side (Liberman, 1982). The same topographic organization is also observed in the spiral ganglion, where the cell bodies of the primary nerve fibers reside. The cell bodies of neurons with high spontaneous rate tend to cluster on the scala tympani side of the ganglion, while neurons with low and medium spontaneous are more likely to be found on the scala vestibuli side (Leake and Synder, 1989). Therefore, the functional organization responsible for the coding of

frequency and intensity information is represented as two orthogonal spatial patterns in the spiral ganglion, the first neural element of the auditory pathway.

The firing properties, ion channel levels and synaptic protein distributions of spiral ganglion neurons have been systematically characterized using *in vitro* cultures (Davis, 2003; Davis and Liu, 2011). Not surprisingly, intrinsic properties of spiral ganglion neurons are also tuned according to the tonotopic map of the cochlea. In postnatal murine spiral ganglion, overall, the kinetics-related parameters of neuronal firing are progressively faster in the base compared to the apex, consistent with the requirement for the coding of higher frequency sound in the basal region. Basal neurons showed shorter action potential latency and duration, and less firing accommodation, which is quantified by AP_{max}, the maximum number of spikes the neuron could fire in response to sustained depolarization (Adamson et al., 2002b). On the other hand, the excitability-related intrinsic features such as resting membrane potential and voltage threshold of action potential firing has been shown to exhibit a non-linear tonotopic trend, such that the apical and middle region showed lower firing threshold and higher resting membrane potential than the basal region (Liu and Davis, 2007; Liu et al., 2013), which is consistent with the fact that the mid-cochlear region displays the lowest hearing threshold in behavior tests (Müller et al., 2005). Thus, the intrinsic properties of spiral ganglion neurons could contribute to the physiological organization committed to frequency and intensity coding, as revealed by *in vivo* recordings at the auditory nerve.

Beyond the frequency and intensity map briefly reviewed above, very little is known about whether other processing and coding mechanisms are present in the cochlea. In the light of the coding strategies employed by other sensory systems, the coding capacity of peripheral organs is highly dependent on the diversity of cell types and connection patterns that they possess. In the retina, for example, there are distinct cell types and separate neural circuits organized to restructure visual information into light intensity, color contrast and motion (Gollisch and Meister, 2010). In the olfactory system, in addition to the classic chemotopic organization in which mitral/tufted cells in different glomeruli of olfactory bulb receive projections from olfactory sensory neurons expressing different types of odorant receptors, an additional dimension of parallel processing is represented by mitral/tufted cells in each glomerulus that encode non-redundant odor information (Dhawale et al., 2010). In the somatosensory system, parallel processing is represented by different receptors and afferent fibers that code distinct sub-modalities of body senses such as touch, pain, itch, and temperature (Reed-Geaghan and Maricich, 2011). In the spiral ganglion, however, although diversity of firing features has been observed across the tonotopic axis (Adamson et al., 2002b; Reid et al., 2004; Liu and Davis, 2007), there is still much to learn about potential subpopulations within each cochlear region and type I-type II categories. Studies presented herein further the characterization of the subpopulations and function diversity in the spiral ganglion, which contribute new insights into the understanding of parallel pathways and coding mechanisms in the cochlea.

Chapter 2

Methods

in vitro culture of spiral ganglion explants

Procedures performed were approved by the Rutgers University Institutional Review Board for the Use and Care of Animals. Postnatal tissues were dissected from P6-P7 CBA/CaJ mice. Cochlear whole-mounts were subjected to fixation and staining immediately after dissection. For neuronal cultures, uncoiled spiral ganglion from P6-7 mice was divided into five parts and three of them, from the apical, middle and basal regions were isolated onto poly-L-Lysine coated culture dishes and maintained in growth medium: DMEM (Sigma) supplemented with 10% fetal bovine serum, 4 mM L-glutamine, and 0.1% penicillin–streptomycin.

Dissociated culture of spiral ganglion neurons

Dissociated cultures were prepared based on previous reports (Wei et al., 2007; Lv et al., 2010) with modifications. Spiral ganglion tissue from apex, middle or base regions was dissected in the following solution: Minimum Essential Medium with Hank's salts (Invitrogen), 0.2 mg/mL kynurenic acid (Sigma), 10 mM $MgCl_2$, 2% fetal bovine serum (FBS; v/v), 6 g/l glucose. Tissues were digested with 1mg/ml type I collagenase (sigma) and 1mg/ml DNase I (Roche) dissolved in digestion solution, which was identical to the dissection solution except for FBS was replaced by 2% B27 (Invitrogen). After the tissue

was incubated in the digestion solution for 20min at 37°C, the enzymes were quenched by adding equal volume of FBS. The tissues were then titrated with fire polished glass pipettes and the cell suspension was seeded into culture dishes (0.5ml/dish). 2ml of growth medium described above was added after the 1h. All types of culture dishes were maintained at 37°C in a humidified incubator with 5% CO_2 until used on desired DIV.

Acute OC-SGN preparation

Cochlae were dissected from P0-8 mice and the modiolar bone was removed. Care was taken to ensure that both the spiral ganglion and the organ of Corti were intact.The preparation was then uncoiled and mounted on coverslips using Cell-Tak (Corning) and then transferred immediately to the recording chamber.

Immunohistochemistry for cultures

For cochlear whole-mounts and neuronal cultures, preparations were fixed and permeabilized with 100% methanol at -20°C for 6 min and rinsed three times with 0.01M PBS (pH 7.4). Before the application of antibodies, specimens were incubated with 5% normal goat serum (NGS) for 1h at RT or 4°C overnight. Specimens were incubated with primary antibodies at either 4°C overnight (peripherin, calretinin and calbindin) or at RT for 1h (β-tubulin). Monoclonal mouse anti-β-tubulin (1:200, Covance, MMS 435P) was used to label all neurons and monoclonal mouse anti-peripherin (Chemicon, MAB1527) antibody to specifically identify putative type II spiral ganglion neurons. Polyclonal rabbit anti-calretinin (Millipore, AB5054) was used at 1:200. Polyclonal rabbit anti-calbindin (Swant, CB38) and monoclonal mouse anti-calretinin (Millipore)

antibodies were used at 1:100. After washing 3X with PBS the preparations were incubated with 5% NGS for 1h at RT and then with one of the following secondary antibodies at 1:100 for 1h at RT: Alexa Fluor 594 conjugated goat anti-mouse; Alexa Fluor 488 conjugated goat anti-rabbit, Alexa Fluor 350 conjugated goat anti-mouse (Invitrogen). Multi-antibody-labeling was done sequentially. At the end of all the staining steps the preparations were washed with 0.01M PBS and mounted in DABCO medium (Sigma-Aldrich).

Immunohistochemistry for the acute preparation

All preparations were fixed in 4% PFA at 4°C overnight and rinsed with 0.01M (1X) PBS. For diaminobenzidine (DAB)-based processing, the samples were quenched in 3% H_2O_2 and then permeabilized with 2% Triton for 1h at RT. Chromogen reaction was carried out using vectastain ABC kit (Vector Laboratories, PK-6100) and Impact DAB EqV substrate (Vector Laboratories, SK-4103) following manufacturer's instructions. For fluorescent intracellular labeling, Alexa 594-conjugated streptavdin was used at 1:100 for 2h at RT after fixation and permeabilization. Polyclonal rabbit anti-Myosin-7a antibody (Proteus) was used at 1:200 as a hair cell marker. For antibody labeling, the same method used for culture staining was adapted.

Image acquisition

Images of neuronal cultures were acquired with a fluorescent microscope (Zeiss) and camera (Hamamatsu 1394 ORCA-ER) using IPLab Scientific Imaging software (BD Biosciences). Immunolabeled cochlear whole-mounts were visualized using a LSM 510

confocal microscope (Zeiss) with 10X and 63X water immersion DIC objectives. Some images were adjusted by brightness and contrast using IPLab, LSM Image Browser (Zeiss) and Adobe Photoshop software for presentation purposes as previously described (Flores-Otero et al., 2007).

Staining irradiance analysis

At least 3 experiments were used for each quantitative evaluation. A single experiment was composed of multiple measurements from individual neurons (usually more than 200 per experiment) from apical, middle and basal explants isolated from two cochleae. Immunostaining irradiance against the protein of interest was quantified and combined using the following analysis: Exposure time of each color channel was fixed within a single experiment to enable internal comparison. Staining against the neuronal marker β-tubulin, which exhibited a relatively uniform pattern throughout the ganglion, was used in all experiments to obtain a general reference image. For cytoskeleton anti-peripherin staining, the fluorescence intensity was sampled by a box tool with an area of 36 pixels in the region of interest on an acquired image using IPLab software. The staining irradiance value of a neuron was determined by subtracting the average of four surrounding background measurements from the average of three measurements in the brightest area in the soma. For antibodies that stain both the cytoplasm and the nucleus, the staining irradiance value of each cell was determined by the average irradiance over the entire soma (Fig. 2.1) and then subtracting the average of four surrounding background measurements with the box tool. The normalized staining irradiance of a neuron was

represented by the ratio of its measured fluorescent intensity to that obtained from the brightest neuron in the same experiment. In some of the experiments, electrophysiological recordings were made prior to immunostaining. Hoffman modulation contrast images of each recorded neuron were taken to document cell position and care was taken to re-identify the recorded neurons in the staining images with the aid of unique marking on the dish (Reid et al., 2004). All dishes within a single experiment from which recordings were obtained were visualized for immunostaining with the same exposure time. In order to compare levels across individual experiments, the staining irradiance of each neuron was normalized to the brightest cell in the group of samples that underwent the same staining procedure.

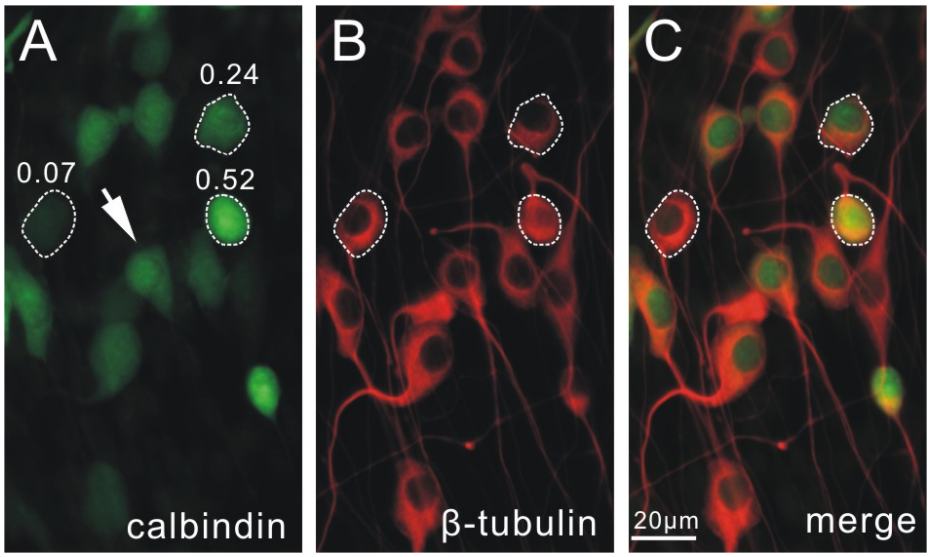

Figure 2.1: Subcellular distribution and characterization of immunostaining levels. Representative double immune-stained images of neuronal cultures using anti-calbindin (**A**) and anti-β-tubulin (**B**) antibodies. **C**, merged image. Note that calbindin staining was heterogeneous while anti-β-tubulin staining level was relatively uniform in all cells. Arrow, a neuron stained with anti-calbindin antibody showed brighter spots in the nuclei, suggesting differential staining levels within different sub-cellular compartments. Three cells with high, intermediate and low levels were circled with dashed line, and the normalized calbindin staining irradiance values was indicated on top of each cell in **A**.

Electrophysiology

All data were collected at room temperature from neuron somata, and pipette offset currents were zeroed just before contacting the cell surface. Recordings were made with Axopatch 200A amplifier (Axon Instruments) and I_{fast} circuitry was used for whole-cell current clamp mode. Data were digitized at 5kHz and filtered at 1kHz. Programs of data acquisition and analysis were generously contributed by Dr. Mark Plummer, Rutgers University. For recordings made from cultures, glass pipettes (Sutter Instruments, cat.# BF 150-110-10) were pulled on a vertical puller (Narishige, model# PP-83) and coated with Sylgard (Dow Corning). Pipette tips were fire-polished immediately before use and resistances ranged from 3 to 10MΩ. Pipettes were filled with the following internal solution: 112mM KCl, 0.1mM $CaCl_2$, 2mM $MgCl_2$, 11mM EGTA, 10mM HEPES, pH 7.5. Neurons were exposed to the following bath solution: 136.9mM NaCl, 5.4mM KCl, 1.67mM $CaCl_2$, 0.98mM $MgCl_2$, 16.7mM glucose, 50mM sucrose, 10mM HEPES, pH 7.5. Current clamp recordings were considered of acceptable quality if they met the following criteria: the amplitude of the first action potential exceeds 70mV, stable membrane potentials, low noise levels and discernible membrane time constant on step current injection. If any of the parameters changed during a recording, the remainder of the data was excluded due to an indication of compromised cell integrity. For recordings made in acute preparation, experiments were visualized under infrared differential interference contrast (IR-DIC) microscopy (Olympus BX50WI). Glass pipettes with 1.2mm outer diameter (Sutter Instruments, cat.# BF 120-69-10) were used and Sylgard

was not applied. Pipette resistances ranged from 5 to 15MΩ. Pipettes were filled with internal solution as follows: 112mM KCl, 0.1mM $CaCl_2$, 2mM $MgCl_2$, 2mM Mg-ATP, 2mM Na-ATP, 0.2mM Na-GTP, 11mM EGTA, 10mM HEPES, pH 7.5. The preparations were exposed to bath solution: 128mM NaCl, 4mM KCl, 1.5mM $CaCl_2$, 1.3mM MgSO4, 1.25mM $NaH2PO_4$, 10mM glucose, oxygenated to pH 7.4. In some experiments, 5mg/ml biocytin (Life Technologies) was included in the pipette solution for intracellular labeling. After recording, the pipette was carefully withdrawn and the neuron culture was fixed and evaluated with immunohistochemistry.

Measurement of intrinsic firing parameters

Prior to entering the whole-cell current clamp configuration, the endogenous resting membrane potential of each neuron was assessed non-invasively (Verheugen et al., 1999). In brief, single K^+ channel activity was recorded to voltage steps from -100mV to -20mV from a holding potential of -60mV, with standard internal solution in the pipette (Fig. 2.2A-B). Due to the relatively high concentration of K^+ across the cell membrane, the resting membrane potential was determined as the reversal potential from the I-V relationship of a K^+ channel (Fig. 2.2C). K^+ selective channels with conductances in the range of 35-50pS, which were observed most frequently in our recordings, were used to calculate the resting membrane potential. In some recordings, channel openings with large amplitudes (Fig. 2.2B) were also observed and reversed at a similar potential as the 35-50pS channels (Fig. 2.2C, arrow), consistent with the reported presence of the BK channel in the murine spiral ganglion (Adamson et al., 2002b). Subsequent to single

channel recording and on-line resting membrane potential calculation, the cell was held at its endogenous resting membrane potential in current clamp mode. Threshold level was reached when the same depolarization conditions fluctuated between just sub-threshold activity and an action potential. Voltage threshold was determined as the peak voltage level (Fig. 2.2D, arrow) of the just sub-threshold trace (Fig. 2.2D, black); differential voltage was defined as the voltage difference between holding potential and voltage threshold. Onset tau was determined from a double-exponential fit to the sub-threshold trace. Width of a supra-threshold action potential (Fig. 2.2D, gray) measured at the mid height between the peak and nadir was measured as duration (half-width) and the time difference between stimulus onset and the peak of the action potential was determined as firing latency. The neuron was then depolarized to supra-threshold voltage levels until the maximum number of spikes occurred and AP_{max} was documented (Mo and Davis, 1997) .

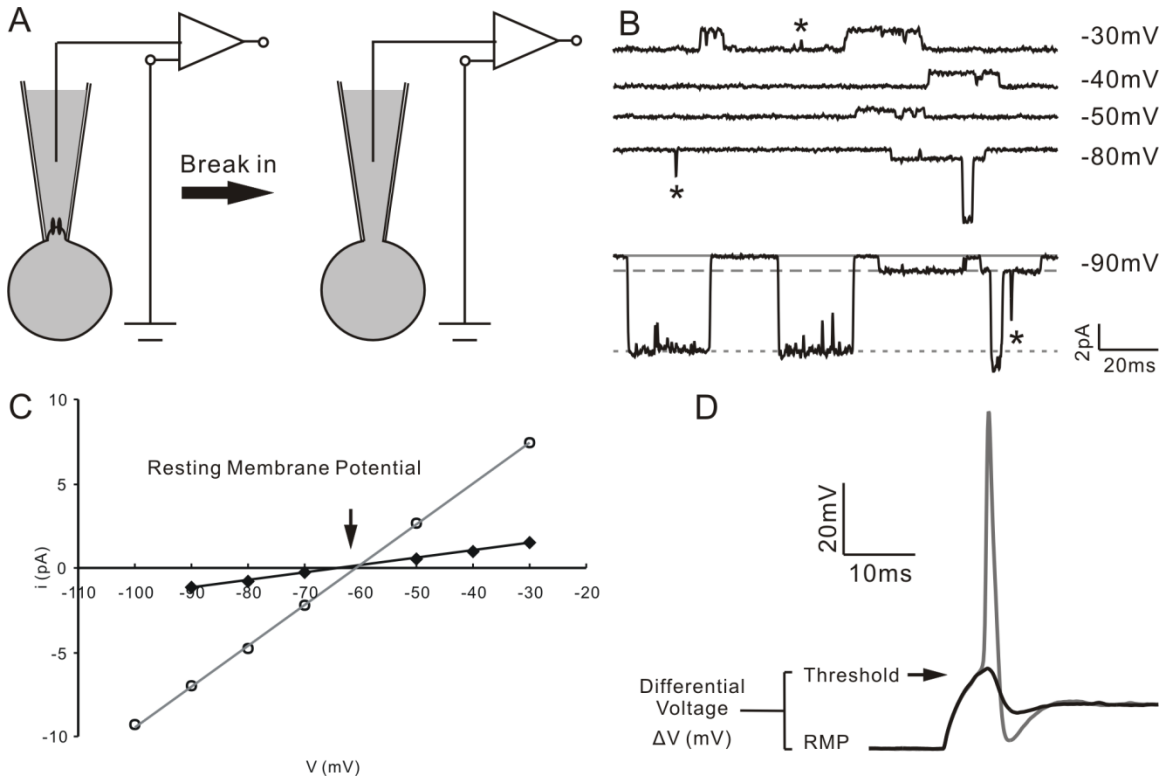

Figure 2.2: Non-invasive measurement of resting membrane potential. A, Diagram of the recording procedure. Cell-attached single channel recording was used to non-invasively assess the resting membrane potential (left). Additional suction was applied to break-in for subsequent whole-cell current clamp recording (right). **B**, Single channel traces at the indicated test potentials from -60mV holding potential. Based on relative amplitude, two types of channel openings with small and large amplitudes could be observed. Solid line, closed state; dashed line, opening of the small-conductance channel; dotted line, opening of the large-conductance channel. Transient currents (asterisk) were due to incomplete channel opening events and were not used for the analysis of conductance. **C**, I-V relation of two channels plotted from the recordings in **B**. The two channels exhibited distinctive conductances (43.7pS and 240.6pS) but comparable reversal potentials (-63.5mV and -60.3mV, respectively). **D**, Superimposed exemplary traces showing sub-threshold (black) and threshold (gray) measurements of voltage threshold and differential voltage. The cell was held at the endogenous resting membrane potential calculated on-line from cell-attached recording.

Electroporation

Electroporation of acutely dissected embryonic cochlear whole-mounts was performed following previous reports (Jones et al., 2006). In brief, cochlear explant were dissected from mice on embryonic day 13-14, each cochlea was transferred to a 10μl drop of construct DNA dissolved in 1XPBS, with final concentration of 1~3μg/μl. The tissue was placed such that the cochlear disk was perpendicular to the dish surface. Microelectrodes (Harvard Apparatus, catalog No. 45-0115) were placed across the cochlear disk and square wave pulses were applied using an elctroporator (BTX, catalog No. 45-0052) with following parameters: 25V, pulse duration 30ms, interval duration 950ms, 9 pulses per cochlea. After electroporation, the cochlae were collected and incubated in growth medium (DMEM with 10% FBS) for 10 min, and treated with 0.25% trypsin (Life Technologies) for 10 min. The tissue was then titrated in growth medium and the cell suspension was transferred to culture dishes and maintained for future experiments.

DNA constructs

The *pCIG-Ascl1*, *pCLIG-NeuroD1* constructs and the *pCIG* empty vector were kindly provided by Dr Alain Dabdoub (University of Toronto).

Statistical analysis

Average data were presented as mean ± standard error of means (SEM). One-way ANOVA was carried out to determine differences among groups of data followed by *post hoc* analysis. Student's *t*-test (for comparing two groups) or Tukey's honestly significant difference (HSD) test (for the comparison of multiple groups) were used to calculate *p*

values. The Kolmogorov-Smirnov test was used to compare the distribution of two samples and the *p* value calculation was based on a two-sided assumption.

Chapter 3

Subpopulations of spiral ganglion neurons specified by calcium binding proteins

Primary auditory afferents are classified into categories of type I and type II neurons, which innervate inner and outer hair cells, respectively (Ryugo, 1992). Interestingly, in contrast to the visual, olfactory and somatosensory systems in which distinct receptor types and local circuitry are explicitly committed to different modalities, the functional significance of two distinct type I and type II pathways remains largely unknown. Most *in vivo* recordings have been made from the type I fibers that compose 95% percent of the neuronal population, while very little data has been obtained from the small, unmyelinated type II fibers. It is clear that it is the type I neurons that are primarily responsible for auditory sensation (Liberman, 1982; Keithley and Schreiber, 1987; Ruggero, 1992), whereas the exact contribution of the type II neurons to audition is under dispute (Robertson, 1984; Brown, 1994; Reid et al., 2004; Weisz et al., 2009). Beyond the type I and II dichotomy, very little is known about potential subpopulations in each category. This is in contrast to the striking heterogeneity of cell types with distinct morphological and physiological features in other sensory organs (Wässle, 2004; Marmigère and Ernfors, 2007; Angelo et al., 2012). Thus, much remains to be learned about this primary afferent element and the fundamental characteristics of possible neuronal subtypes that could underlie processing of auditory stimuli.

Toward this goal we utilized the calcium binding proteins calretinin and calbindin, which have been used to characterize cell subtypes in the brain as well as in sensory systems. In the retina, heterogeneous levels of calretinin and calbindin immunocytochemical labeling reflect the highly organized and complex structure in the inner plexiform layer (Haverkamp and Wässle, 2000; Wässle, 2004). Moreover, there is evidence that calretinin and calbindin are differentially distributed in rat amacrine cells and retinal ganglion cells (Mojumder et al., 2008) suggesting that these calcium binding proteins subserve different functions. Therefore, examination of the distribution of calretinin and calbindin may help to elucidate the structural and physiological basis for possible parallel pathways in the spiral ganglion.

In this study we sought to determine the relationship between the amount and type of calcium binding protein present in spiral ganglion neurons and the accompanying functional impact. Our results show that both calretinin and calbindin are distributed heterogeneously in the postnatal spiral ganglion *in vitro*, the relative amounts of which correlate with one intrinsic firing parameter, the onset tau of sub-threshold responses. Calretinin is highest in the type I neurons in the mid-cochlear region and type II spiral ganglion neurons in the apex were shown to possess the highest levels of calbindin and lowest levels of calretinin. Thus, anti-calretinin and anti-calbindin immunolabeling revealed an additional layer of heterogeneity in both type I and type II spiral ganglion neurons, indicating another dimension of specification that may contribute to the complex

signaling capacity of the spiral ganglion.

Heterogeneous distribution of calretinin and calbindin in the spiral ganglion

Calretinin and calbindin, widely used as markers for neuronal subpopulations in the central nervous system and in the vestibular ganglion, (DeFelipe, 1997; Kevetter, 2002; Leonard and Kevetter, 2002) are also present in the embryonic and postnatal mouse spiral ganglion (Dechesne and Thomasset, 1988; Dechesne et al., 1994). In order to determine whether sub-classes of auditory afferents could be identified by calcium binding protein distributions we characterized the distribution patterns of calretinin and calbindin within and throughout the ganglion in postnatal day 6-7 (P6-7) CBA/CaJ mice, at a well-characterized stage of development (Mo and Davis, 1997; Adamson et al., 2002b; Reid et al., 2004) when afferent innervation in the cochlea has been established (Huang et al., 2007).

As a first step, acute preparations were utilized to determine the intra-ganglion spatial organization and intracellular co-localization of anti-calretinin and anti-calbindin antibodies. Observations of anti-calretinin antibody in postnatal cochlear sections in which the structural detail of the cochlea was retained showed that the hair cells (Fig. 3.1A) and neuronal cell bodies in the spiral ganglion and afferent fibers (Fig. 3.1B-E) were strongly labeled. By comparison, anti-calbindin antibody labeling had distinctly lower irradiance levels in the cell bodies of spiral ganglion neurons compared to the hair cells within the same section (Fig. 3.1F-J). Despite their relatively different staining

levels when compared to the hair cells, we found that both calretinin and calbindin labeling was heterogeneous in spiral ganglion neurons. Neighboring neurons in the same region of the ganglion exhibited low, intermediate and high levels of calretinin or calbindin staining without any discernible spatial organization, while anti-β-tubulin antibody staining levels of these neurons were largely uniform (Fig. 3.1B-E, G-J). Notably, when neurons in different tonotopic regions were compared in the low magnification image, overall level of anti-calretinin staining irradiance in the mid-cochlea appeared to be higher than that of the very basal region (Fig. 3.1A). Anti-calbindin staining levels also showed a slightly decreasing trend from the middle to the base, but only very limited difference was observed (Fig. 3.1F).

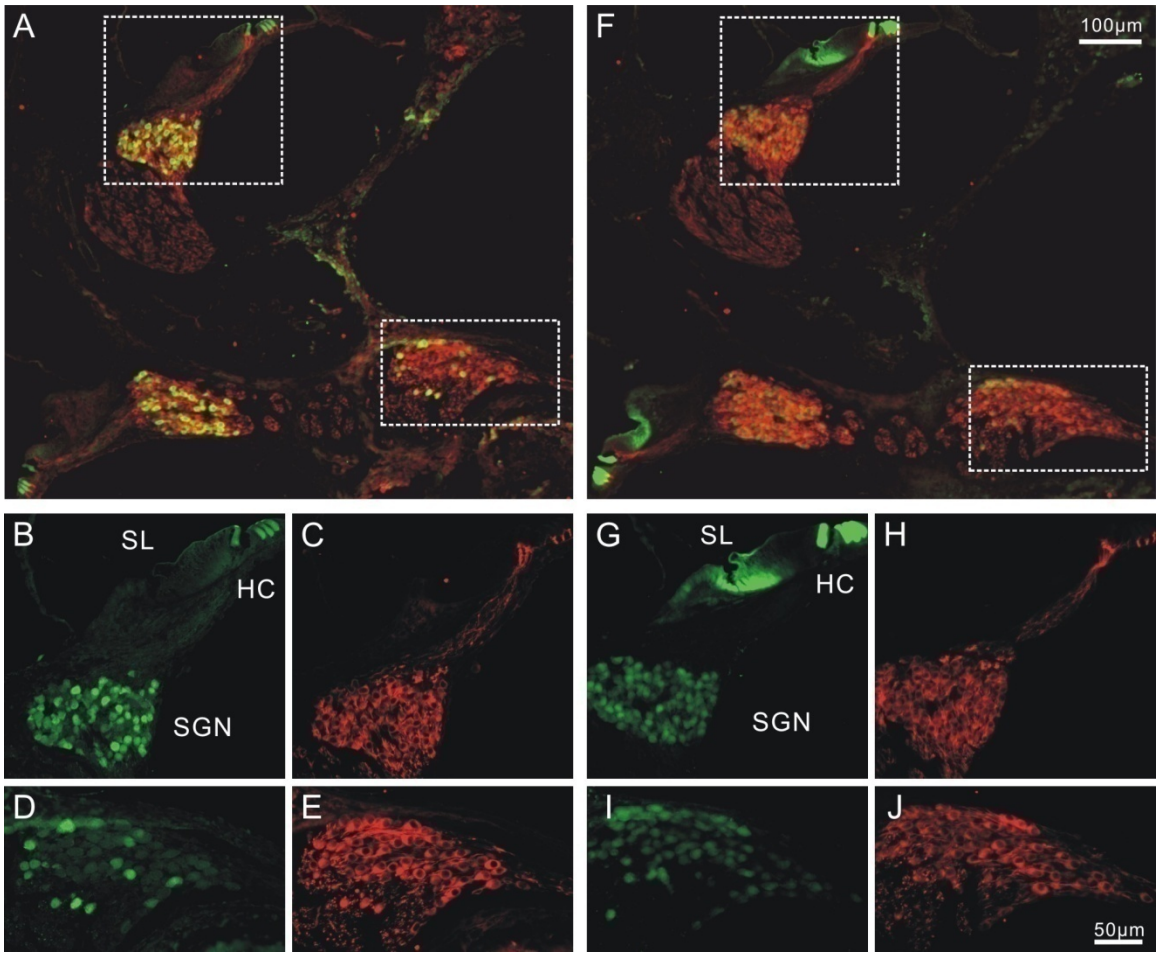

Figure 3.1: Distribution patterns of calretinin and calbindin in P6 mouse cochlea. Two cochlear sections in close proximity were stained with anti-calretinin (**A-E**) and anti-calbindin antibodies (**F-J**) respectively. Both anti-calretinin and anti-calbindin antibody staining showed heterogeneous patterns in the spiral ganglion. HC, hair cell. SGN, spiral ganglion. SL, spiral limbus. **A**, Low magnification image of cochlear sections double labeled with anti-β-tubulin (red) and anti-calretinin (green) antibodies **B**-**E,** High magnification images of middle (**B-C**) and basal (**D-E**) neuronal regions enclosed by dotted line in **A**. **F,** low magnification image of a cochlear section showing double labeling of anti-calbindin (green) and anti-β-tubulin (red) antibodies. Prominent calbindin staining was also observed in the spiral limbus **G-J**, High magnification image of the middle (**G, H**) and basal (**I,J**) regions as squared in **F**. Scale bar in **F** applies to **A, F**. Scale bar in **J** applied to **B-E, G-J.**

In order to examine the distribution of the two calcium binding proteins we co-labeled acutely prepared cochlear whole-mounts with anti-calretinin and anti-calbindin antibodies (Fig. 3.2A and B, respectively). We found that the heterogeneous distribution patterns of each calcium binding protein labeling showed varying degrees of overlap. While the majority of neurons possessed relatively low levels of both proteins with a continuum of combinations (Fig. 3.2A-C, arrow), high levels of calretinin (red) and calbindin (green) staining irradiance were mainly present in distinct, non-overlapping subpopulations of cells (Fig. 3.2A-C, arrowheads). Neurons labeled with high levels of both calcium binding proteins were relatively rare (Fig. 3.2A-C, asterisk). This pattern was quantitated from an in vitro neuronal culture system which showed essentially identical staining patterns (Fig. 3.2D) and provided the opportunity to evaluate electrophysiological firing patterns.

Calretinin and calbindin distributions were quantified from immunostained images, normalized, and plotted in frequency histograms (Figs. 3.2E and F, respectively). Each was well fitted with the sum of three Gaussians, yet with distinct means (calretinin: 0.10, 0.22, 0.42 and calbindin: 0.08, 0.15, 0.24). When the irradiance values for calretinin were plotted against calbindin from each location (Fig. 3.2G) the data confirmed our observations that the majority of cells exhibited low levels of calretinin and calbindin staining irradiance (category III in Fig. 4G and inset; n=148) and that the high calretinin (category IV, n=74) and calbindin (category II, n=87) staining irradiance was relatively

non-overlapping since only 11 neurons were observed in category I. Thus, the intracellular distribution of calretinin and calbindin distribution mainly fell into three broad categories in which either calretinin or calbindin irradiance predominated or there was relatively low levels of both calcium binding proteins.

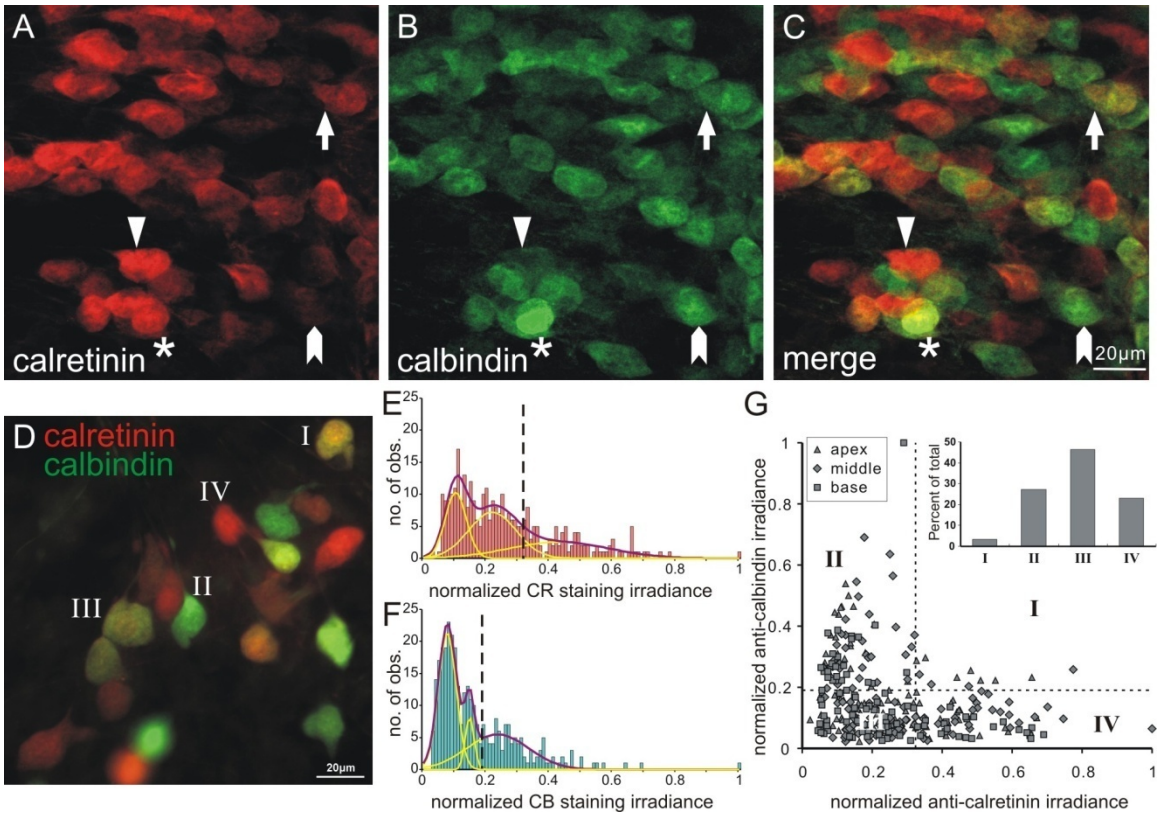

Figure 3.2: Calretinin and calbindin exhibited differential distribution patterns in murine spiral ganglion. A-C, The mid-cochlear region of a whole-mount preparation of P7 mouse spiral ganglion labeled with mouse anti-calretinin (**A**) and rabbit anti-calbindin (**B**) antibodies. **C,** The merged image of **A** and **B**. Most cells were labeled by mainly calretinin (triangle), mainly calbindin (arrowhead), or a low level of both (arrow). Only a few neurons possessed a high level of both staining (asterisk). Scale bar in **C** (20µm) applies to **A-C**. **D**, Superimposed image of *in vitro* culture shows heterogeneous distribution pattern of calretinin and calbindin that range from mainly calretinin-staining cells (red) to mainly calbindin staining cells (green) similar to **A-C**. Example cells were labeled according to the four categories in **G**. Frequency histograms of normalized calretinin staining irradiance (**E**) and normalized calbindin staining irradiance (**F**) were constructed from measurements of the same single experiment as shown in D (total number of measurements = 320). Both histograms were composed of multiple populations with distinct staining irradiance levels which could be fit by the sum of three Gaussians with discrete means. The vertical dashed lines (**E** and **F**, respectively) delineate the mid points between high and medium means of Gaussian fits of normalized calretinin (0.32) and normalized calbindin (0.19) staining irradiance used in **G** inset. **G**, scatter plot of normalized calretinin and calbindin staining measurements in each neuron. **Inset**, Cells were divided into four categories to highlight relative irradiance patterns based on both x and y cutoffs (dotted lines in **E-F**).

Tonotopic variation of calretinin and calbindin staining levels *in vitro*

The spiral ganglion exhibits a tonotopic gradient of neuronal firing patterns, neurotrophin levels, voltage-gated ion channel density, and synaptic protein distribution (Davis, 2003; Flores-Otero et al., 2007). It has also been shown that calbindin levels in hair cells vary with tonotopic position in both mammalian (Pack and Slepecky, 1995) and chick cochlea (Hiel et al., 2002). To determine whether the heterogeneous distribution of calretinin and calbindin in mouse spiral ganglion is also related to tonotopic organization, we compared quantitative staining irradiance measurements of calretinin and calbindin in three separate frequency regions.

For calretinin, the heterogeneity is present in each of the tonotopic locations that we evaluated (Fig. 3.3A-C) in contrast to a relatively uniform neuronal β-tubulin staining pattern (Fig. 3.3D-F). This local heterogeneous pattern was quantified by histograms of normalized staining irradiance measurements in each tonotopic region pooled from seven individual experiments (Fig. 3.3G-I, dark bars). Histograms constructed from the staining measurements of base, middle and apex neurons in all seven individual experiments could be best fitted with the sum (Fig. 5G-I, purple fitted curves) of three Gaussians (Fig. 3.3G-I, yellow, cyan and pink fitted curves) with distinct means (base: 0.064, 0.174, 0.428; middle: 0.097, 0.220, 0.407; apex: 0.043, 0.125, 0.251), indicating the presence of multiple populations with differential staining levels in each region. This heterogeneity could also be observed in histograms of data from a single experiment as a subset of the

group data (Fig. 3.3G-I, light bars), which did not capture the full extent of complexity due to the necessarily limited number of observations (100~200 for each region). Interestingly, we found that the average calretinin staining irradiance for individual experiments was significantly higher in the middle region (0.214±0.011) compared with the base (0.139±0.011) and apex (0.134±0.015) regions (n=7, $p<0.01$, Fig. 5J). This quantitative result was also consistent with our qualitative observation in the paraffin embedded sections as described above (Fig. 3.1A).

Calbindin staining irradiance, similar to calretinin, was heterogeneously distributed in neuronal cultures from all tonotopic regions (Fig. 3.4A-F) with different fitted Gaussian mean values (base: 0.110, 0.187, 0.364; middle: 0.132, 0.276, 0.477; apex: 0.121, 0.251, 0.379, Fig. 3.4G-I). However, in contrast to the calretinin staining pattern, average calbindin staining irradiance in cultured neurons did not display significant difference within different tonotopic location (base, 0.233±0.024; middle, 0.236±0.018; apex, 0.234±0.020, n=7, $F(2,18)= 0.0027$, Fig. 3.4J).

In summary, the heterogeneous staining patterns of anti-calretinin and anti-calbindin antibodies were not attributable to tonotopy since they were observed throughout the apical, middle and basal regions. Nevertheless, we did find that the immunostaining levels for one of the calcium binding proteins, calretinin, was significantly higher overall in the mid-cochlear region, while calbindin exhibited comparable staining irradiance in all regions.

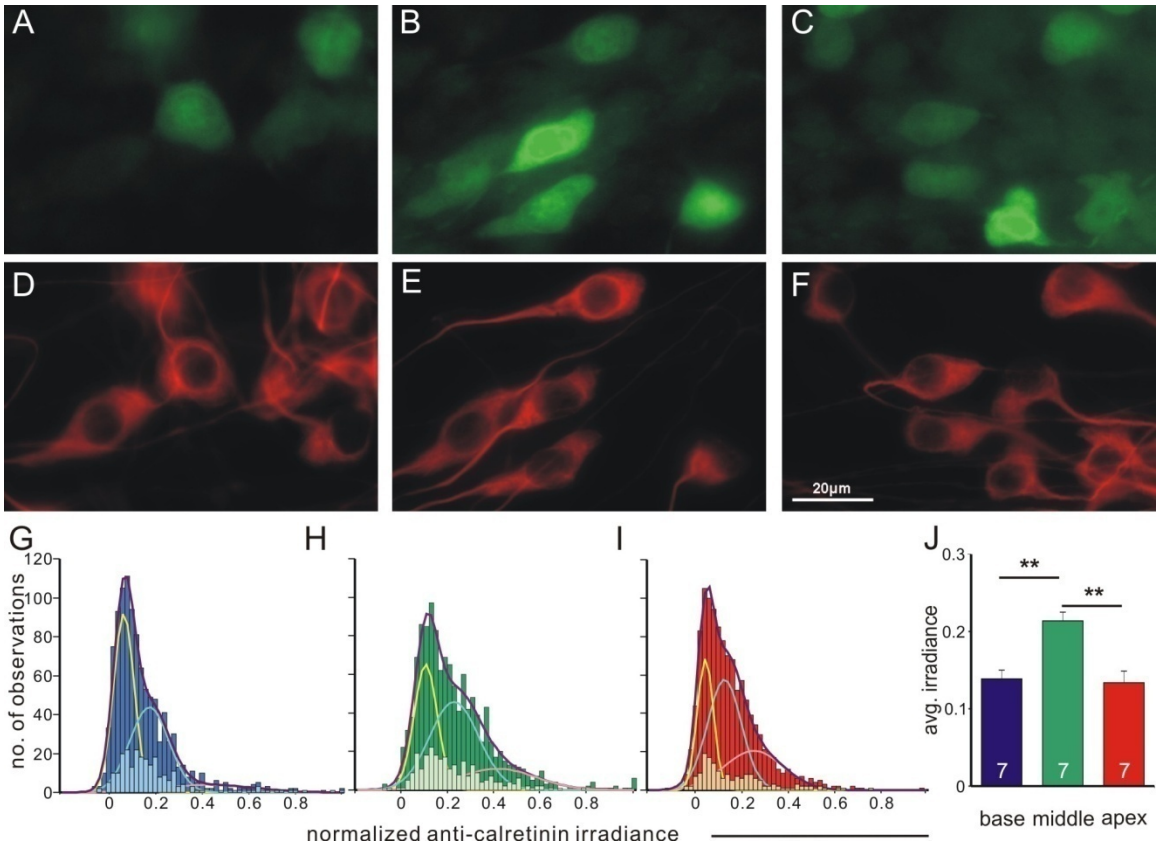

Figure 3.3: Calretinin staining irradiance is heterogeneous in all tonotopic regions and shows higher average values in the middle region. A-C, Cultured neurons isolated from base, middle and apex respectively, labeled with polyclonal anti-calretinin antibody. **D-F**, same neurons in **A-C** labeled with neuron-specific anti-β-tubulin antibody. Scale bar in **D** applies to **A-F**. **G-I**, Frequency histograms of all data in the seven individual experiments pooled for base (**G**, dark blue bars, total No. of measurements, 1057), middle (**H**, dark green bars, total No. of measurements, 1262) and apex (**I**, dark red bars, total No. of measurements, 1162), fitted by the sum (purple curves) of three Gaussians (yellow, cyan and pink curves) with distinct means, indicating the presence of multiple populations with different calretinin staining levels within each region. Measurements from one representative individual experiment shown as subsets of the pooled data (**G**, light blue bars; **H**, light green bars; **I**, light red bars) displayed similar heterogeneity in all tonotopic positions. **j**, Average calretinin staining irradiance is significantly higher (p<0.01) in the middle (n=7).

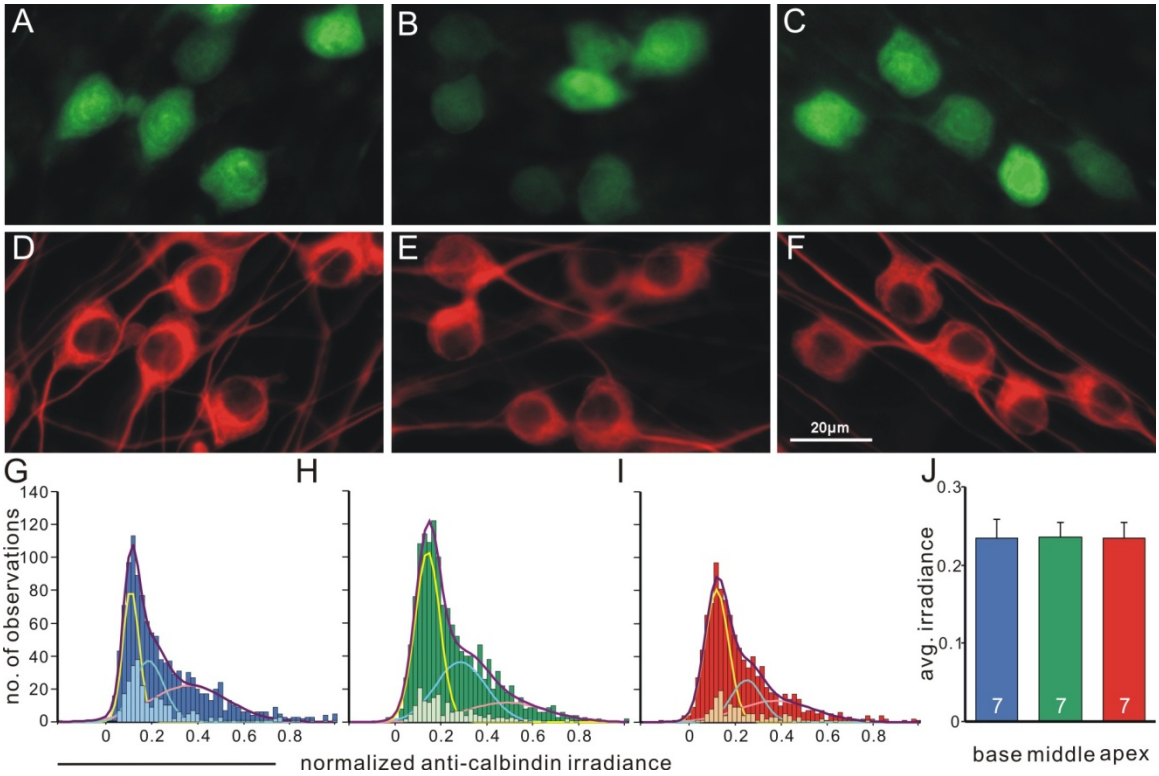

Figure 3.4: Calbindin staining pattern displays local heterogeneity but is generally even across different tonotopic regions. A-C, Cultured neurons isolated from base, middle and apex respectively, labeled with polyclonal anti-calbindin antibody. **D-F**, Same neurons in **A-C** labeled with neuron-specific anti-β-tubulin antibody. Scale in **F** applies to **A-F**. **G-I**, Frequency histograms of normalized calbindin staining irradiance measurements from seven combined experiments were best fitted by the sum (purple curves) of three Gaussians (yellow, cyan and pink curves) with distinct means for base (**G**, dark blue bars, total No. of measurements, 1156), middle (**H**, dark green bars, total No. of measurements, 1463) and apex (**I**, dark red bars, total No. of measurements, 1018). Data points obtained from a single experiment exhibited as subsets of the full data set in each region and displayed heterogeneity. **J**, average calbindin staining irradiance is comparable in each region (n=7).

Calretinin and calbindin staining levels and neuronal intrinsic firing properties

The role of calretinin and calbindin as calcium buffers that regulate intracellular calcium levels and neuronal excitability has been well characterized (Schwaller et al., 2002). The non-linear calretinin distribution within the ganglion opened up the possibly that it might reflect the enhancement of synaptic transmission in the mid-cochlear region (Meyer et al., 2009) or, alternatively, correlate with the higher overall threshold sensitivity of some neurons in the mid-cochlea within a population displaying significant threshold heterogeneity (Liu and Davis, 2007). In order to directly assess whether levels of calretinin and calbindin are correlated with and potentially responsible for these observations, we took advantage of the accessibility of our *in vitro* neuronal culture and related the calretinin and calbindin staining profiles to electrophysiological features. Recordings were made from *in vitro* neuronal cultures isolated from basal, middle and apical regions of the spiral ganglion. To accurately measure excitability and kinetics parameters, we determined the resting membrane potential using the previously described non-invasive method (Verheugen et al., 1999) and measured the voltage threshold, action potential latency, duration and time constant in whole-cell current clamp mode. Differential voltage, defined as the difference between holding potential and the voltage threshold, was also calculated to probe the intrinsic excitability of each neuron. A total of 88 recordings were used for subsequent analysis (base n=32, middle n=31, apex n=25).

First we established that when held at their endogenous resting membrane potentials,

the population of spiral ganglion neurons used for the study exhibited the full range of heterogeneous and tonotopically-related firing patterns observed previously (Adamson et al., 2002b; Liu and Davis, 2007). As expected, we found that in base, middle and apex (Fig. 3.5A-C), the maximum number of spikes a neuron could fire (AP_{max}) increased from base to apex (base 2.72±0.82, middle 10.74±1.77, apex 14.24±1.92; Fig. 3.5D, black bars). Furthermore, consistent with previous findings, both intrinsic excitability and firing kinetics were heterogeneous in each region and were generally graded along the tonotopic axis. Onset time constant (base 3.48±0.20ms, middle 6.81±0.66ms, apex 9.13±0.91ms, $p<0.01$ for base and middle, base and apex; $p<0.05$ for middle and apex; Fig. 3.5E, black bars), action potential latency (base 6.39±0.23ms, middle 9.20±0.42ms, apex 11.59±0.90ms, $p<0.01$ for all pairwise comparisons) and action potential duration (base 1.07±0.03ms, middle 1.11±0.03ms, apex 1.18±0.04ms, base and apex, $p<0.05$) all showed tonotopic trends that increased from base to apex. In contrast to this, and in accord with previous findings (Liu and Davis, 2007), excitability-related parameters showed non-linear trends such that resting membrane potential, voltage threshold and differential voltage (Fig. 3.5F, black bars) were comparable in the middle and the apex (resting membrane potential: middle -64.86±0.31mV, apex -64.90±0.41mV; voltage threshold: middle -45.30±0.62mV, apex -44.98±0.95mV; differential voltage: middle 19.48±0.66mV, apex 20.00±1.07mV) but neurons from the base displayed significantly ($p<0.01$) lower resting membrane potential (-66.74±0.38mV), higher voltage threshold (-41.07±0.65mV) and higher differential voltage (25.74±0.82mV).

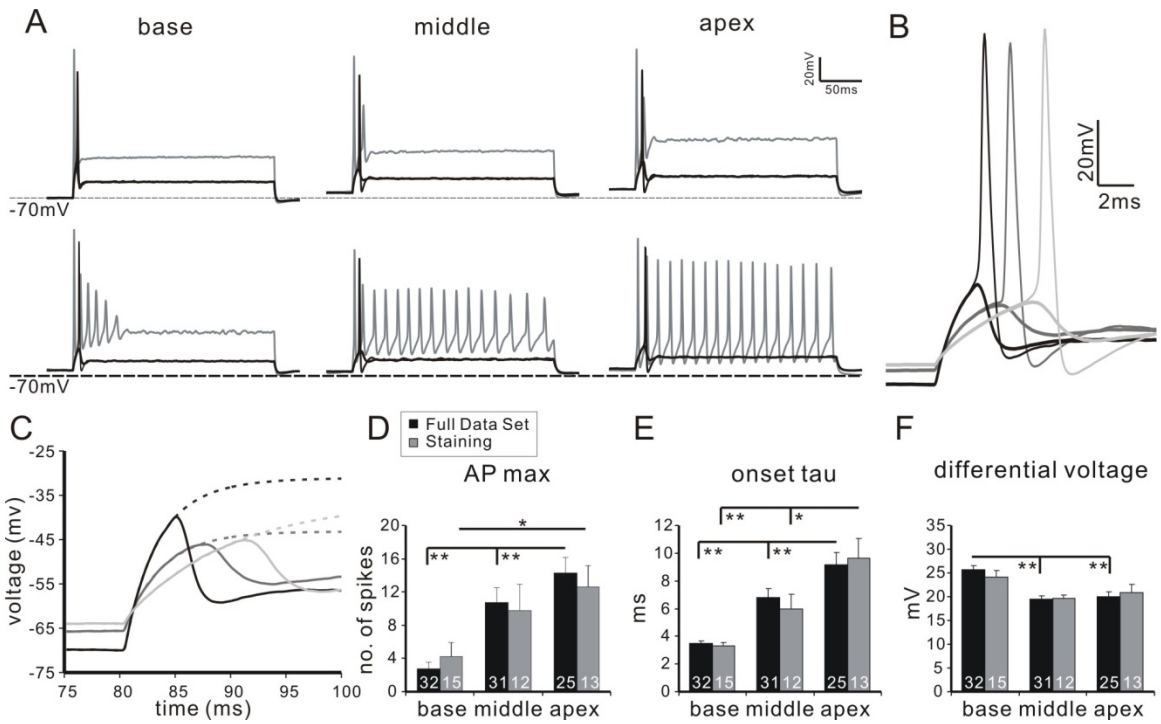

Figure 3.5: Characterization of spiral ganglion neuron firing properties. A, example traces from base (left panel), middle (middle panel) and apex (right panel) neurons. Both rapidly (upper traces) and slowly (bottom traces) accommodating types of neurons were observed in each region. For each recording, sub-threshold (thick black line), threshold (thin black line) and AP max (gray line) traces are shown as overlay. **B**, overlay of just sub-threshold (thick line) and threshold (thin line) traces from base (black), middle (dark gray) and apex (light gray). **C**, Sub-threshold traces in **B** could be fitted with double exponential functions (dotted line). **D-F**, Tonotopic variation of representative intrinsic firing features. Consistent with previous reports, the accommodation of neuronal firing characterized by AP max (**D**) and the kinetics-related parameter time constant (**E**) was graded linearly from base to apex while excitability-related parameter differential voltage (**F**) showed a non-linear trend across different regions. The full data set (**D-F**, black bars) and a subset of recordings associated with immunostaining measurements (**D-F**, gray bars) showed the same tonotopic trend. *, $p<0.05$; **, $p<0.01$.

To correlate calretinin/calbindin content with electrophysiological phenotype, patch-clamp recordings were made from neurons that were subsequently examined with immunocytochemistry. The characteristics of these neurons (base n=15, middle n=12, apex n=13) were representative of the overall electrophysiological patterns (Fig. 3.5D-F, gray bars) and calcium binding protein staining profiles (Fig. 3.6F-G), described above, thus incorporating the full complexity of phenotypes within the ganglion. Comparisons were made with normalized fluorescence intensity; however, non-normalized irradiance levels showed similar results. Of the parameters examined, none correlated with individual comparisons of either calretinin or calbindin staining irradiance levels (Fig. 3.6A-B. R^2 of each parameter with calretinin or calbindin, respectively: time constant, 0.008 and 0.008; differential voltage, 0.071 and 0.041; latency, 0.002 and 0.015; duration, 0.058 and 0.006; AP max, 0.022 and 0.050; resting membrane potential, 0.017 and 0.038; voltage threshold, 0.067 and 0.019). Representative examples of two parameters, differential voltage and onset tau, which represent excitability- and timing-related parameters, are shown in Figure 8A and 8B, respectively.

Interestingly, however, when we utilized the calbindin/calretinin ratio rather than simple levels of individual factors, a striking correlation with electrophysiological properties did emerge (Fig. 3.6D). For the action potential onset tau, neurons with slow kinetics showed normalized calbindin/calretinin staining irradiance ratio values scattered around 1.0 with relatively small deviation. This was quite unlike the calbindin/calretinin

staining irradiance ratio values for fast onset neurons which showed a much wider diversity of labeling patterns. A quantitative comparison between slow onset neurons (onset tau > 7.0 ms) and that of the fast onset neurons (onset tau < 7.0 ms) showed distinct distributions (Kolmogorov-Smirnov test, $p<0.05$), indicating that spiral ganglion neurons with slow-kinetics possess comparable relative levels of calbindin and calretinin proteins, while the relative levels of calretinin and calbindin in neurons with fast-kinetics vary within a broader range (Figure 3.6E). Of the electrophysiological parameters that we examined, latency, another parameter that is closely related to onset tau, showed a similar but less organized pattern. The other parameters unrelated to the firing kinetics did not show an obvious correlation with the calbindin/calretinin ratio (e.g. Fig. 3.6C).

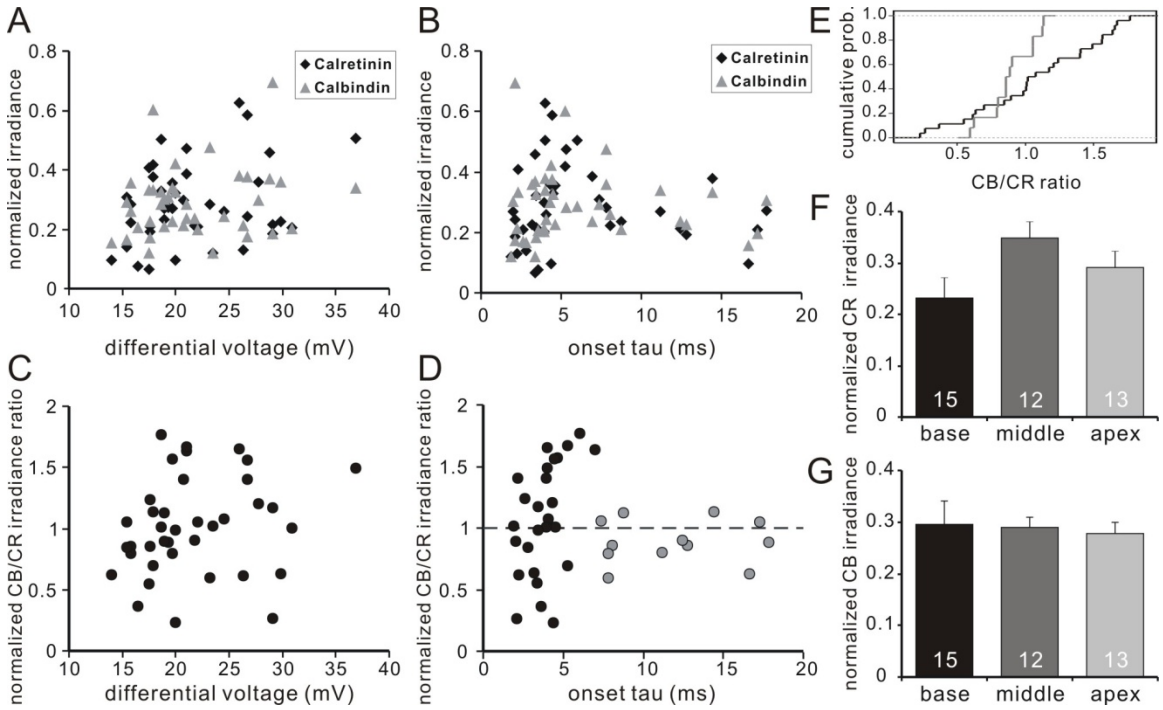

Figure 3.6: Normalized calbindin/calretinin staining irradiance ratio correlates with action potential kinetics. A-B, relation of calretinin (black diamond) and calbindin (gray triangle) staining irradiance with differential voltage (**A**) and threshold onset time course (**B**). Each data point represents a single recording from one neuron. Neither calretinin nor calbindin staining irradiance correlate with the tested neuronal intrinsic firing properties. **C-D**, Relationship between the ratio of normalized calbindin to calretinin staining irradiance with differential voltage (**C**) and onset tau (**D**). Data from neurons with fast (onset tau< 7.0ms) and slow (onset tau>7.0ms) kinetics were color coded in black and gray, respectively. **E**, Cumulative probability of the normalized calbindin/calretinin staining irradiance of fast (black curve) and slow (gray curve) neurons shown in **D**; two sample Kolomgorov-Smirnov test, $p<0.05$. **F-G**, average calretinin (**F**) and calbindin (**G**) staining irradiance of recorded neurons from different tonotopic regions show a similar trend as in Fig. 3.3 and Fig. 3.4.

Heterogeneity of anti-calretinin and anti-calbindin staining in type II neurons

While calretinin and calbindin do not appear to regulate intrinsic firing properties of spiral ganglion neurons directly, the complexity of the spiral ganglion revealed by their differential distribution patterns may be associated with other aspects of functional diversity. Thus, similar to the calretinin and calbindin co-labeling pattern in the retina that indicates separate parallel pathways demarked by calcium binding protein distribution (Mojumder et al., 2008), we wondered whether this was also the case in the spiral ganglion. To explore this possibility further, we took advantage of the type II neuron marker peripherin (Hafidi, 1998) , which has been previously validated to stain type II spiral ganglion neurons specifically (Mou et al., 1998). Co-labeling of peripherin with either calretinin or calbindin was characterized in individual experiments to obtain unequivocal profiles calretinin and calbindin distributions in type I and type II neurons *in vitro.*

Putative type II neurons strongly labeled by anti-peripherin antibody exhibited low levels of calretinin staining *in vitro* (Fig. 3.7A-D), a finding consistent with our observations in acute preparations (data not shown). Pooled data from the seven experiments previously examined (Fig. 3.3) showed that even after putative type II neurons were removed from the analysis they retained their heterogeneous pattern and could still be fitted with the sum of three Gaussians (mean 0.071, 0.178, 0.343). The putative type II neurons, overall, had lower anti-calretinin staining levels (Fig. 3.7E),

which were best fitted by a single Gaussian with relatively low mean value (0.036). When the average calretinin staining irradiance of putative type I and putative type II neurons obtained from seven individual experiments were compared, putative type I neurons showed a significantly higher value than the type II neurons (type I, 0.171±0.010; type II, 0.091±0.015; n=7, $p<0.01$, Fig. 3.7F).

In order to determine whether the total results reflected the staining patterns in all or a sub-set of type II spiral ganglion neurons we made systematic comparisons between different tonotopic regions (Fig. 3.7G). From our observations of individual experiments, an example of which is shown in figure 3.7G, we noted that a preponderance of the putative type II neurons with the lowest anti-calretinin labeling were from the apex (Fig. 3.7G, red symbols). This observation is also seen in the group data from seven experiments analyzed by tonotopic location (Fig. 3.7H). Type I neurons consistently showed the same trend as the overall data, such that the highest average calretinin levels appeared in the middle. Type II neurons, although with the expected fewer numbers of neurons, displayed significantly lower calretinin levels in the apex ($p<0.05$). Taken together, it appears that the greatest difference between type I and type II neurons was manifested in the apical region, thus, revealing a sub-class of type II neurons when evaluated for anti-calretinin immunolabeling.

The relationship between neuronal classes described above is reversed for calbindin-containing putative type II neurons. In this case we noted that

peripherin-stained neurons co-labeled with anti-calbindin antibody (Fig. 3.8A-D), while showing an overall broad range of intensity levels (Fig. 3.8E) the average of which was significantly higher than putative type I neurons (Fig. 3.8F) due to the higher levels in apical type II neurons (Fig. 3.8G, red symbols). Average data from seven experiments analyzed from different tonotopic regions (Fig. 3.8G) showed that while the average calbindin staining irradiance for type I neurons remained comparable in all tonotopic locations (base 0.235±0.025, n=7; middle 0.235±0.017, n=7; apex 0.211±0.021, n=7) and for the base and middle type II neurons (0.200±0.031, n=7 and 0.258±0.065, n=5, respectively), only the apical type II neurons were significantly higher in their anti-calbindin staining irradiance (0.390±0.024, n=7; $p<0.05$). Thus, similar to calretinin, differences between type I and type II calbindin staining levels were only statistically significant in the apex, reaffirming that based on calcium binding protein levels the apical type II neurons have a distinct phenotype.

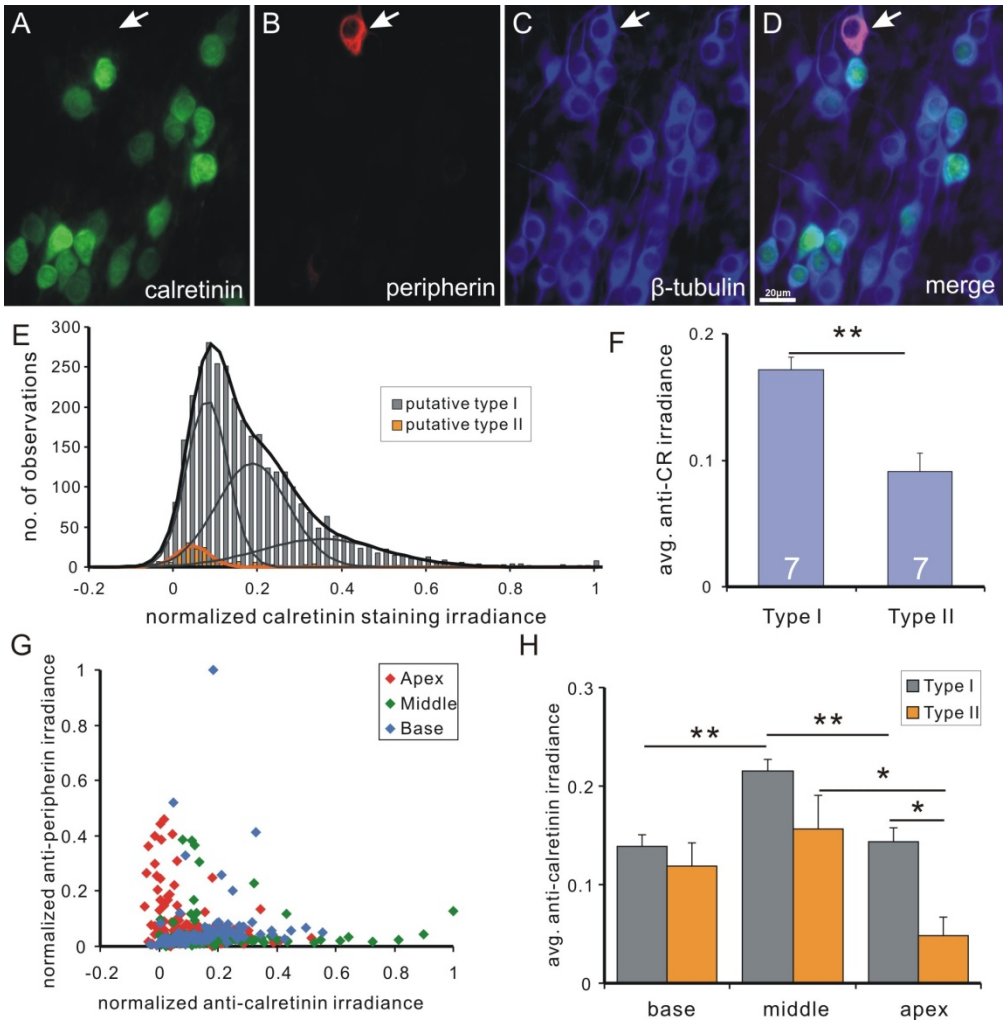

Figure 3.7: Calretinin staining irradiance is consistently low in putative type II spiral ganglion neurons. A-D, spiral ganglion neurons in a neuronal culture triple-labeled with polyclonal anti-calretinin (**A**), anti-peripherin (**B**) and anti-β-tubulin (**C**) antibodies (**D**, merged image). Calretinin staining irradiance is undetectable in a putative type II neuron (arrow) with high peripherin staining irradiance. **E**, frequency histogram of calretinin staining irradiance measurements from seven pooled experiments. Cells with the highest 5% of peripherin staining irradiance (relative to the total number of neurons) were defined as putative type II neurons. Putative type I neurons (gray bars) are best fitted by the sum (black curve) of three Gaussians (gray curves) and histogram of putative type II neurons (orange bars) is best fitted by a single Gaussian (orange curve). **F**, average calretinin staining irradiance of type I neurons in an entire experiment is significantly higher than that of type II neurons ($p<0.01$, n=7). **G**, scatter plot of normalized calretinin staining irradiance and normalized peripherin staining irradiance from the same experiment as in **E**. **H**, Average calretinin staining irradiance level for type I (gray bars) and type II (orange bars) in different tonotopic regions. *, $p<0.05$, **, $p<0.01$.

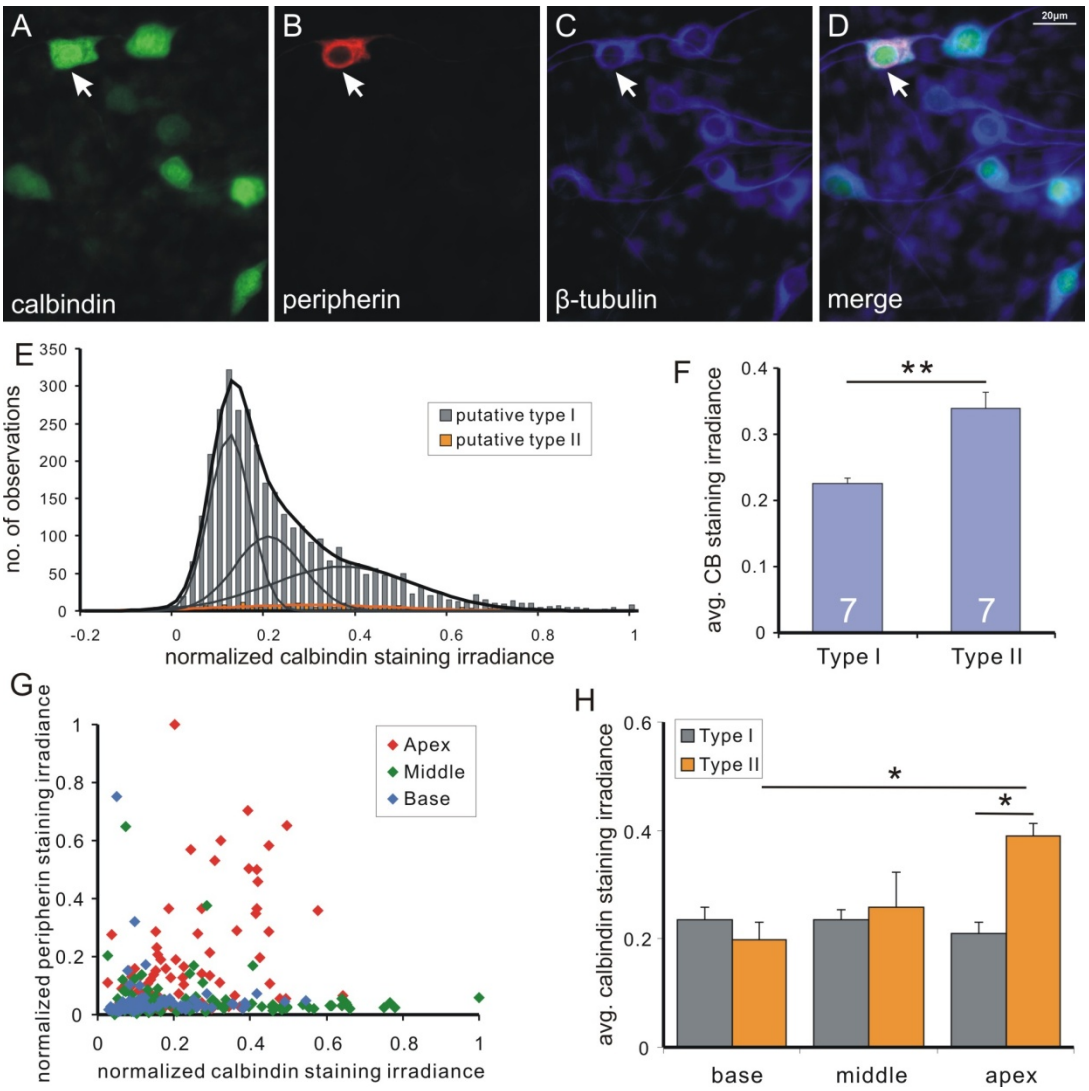

Figure 3.8: Heterogeneous and generally higher levels of calbindin staining irradiance were observed in type II spiral ganglion neurons. A neuronal culture triple-labeled with polyclonal anti-calbindin (**A**), anti-peripherin (**B**), and anti-β-tubulin (**C**) antibodies (**D**, merged). In contrast to calretinin staining, a putative type II neuron (arrowhead) with high peripherin staining irradiance also had high calbindin staining irradiance. Highest 5% peripherin labeled cells were defined as putative type II neurons. **E**, frequency histogram of calbindin staining irradiance data from seven pooled experiments. Putative type I neurons (gray bars) is best fitted by sum (black curve) of three Gaussians (gray curves) and histogram for putative type II neurons (orange bar) is best fitted by a single Gaussian (orange curve). **F**, average calbindin staining irradiance of type I neurons across all experiments is significantly lower than that of type II neurons ($p<0.01$, n=7). **G**, scatter plot of normalized calbindin and peripherin staining irradiance from an example experiment. **H**, average calbindin staining irradiance level for type I (gray bars) and type II (orange bars) in different tonotopic regions. *, $p<0.05$, **, $p<0.01$.

Discussion

Although the presence and abundance of calcium binding proteins in specific cell types is routinely utilized as a cell-type marker (DeFelipe et al., 1999; Markram et al., 2004), only when it has been found to be causal for a specific firing pattern has their functional significance been unequivocally identified within a particular class of neurons (Klapstein et al., 1998; Gall et al., 2003). We noted that antibodies against the calcium binding proteins calretinin and calbindin showed clear categories of low, medium, and high immunolabeling in the spiral ganglion and, thus, herein sought to determine the significance of this observation. We recognized that because the spiral ganglion is composed predominately of a single class of cells, 95% of which are classified as type I spiral ganglion neurons based on their one-to-one innervation of inner hair cells (Ryugo, 1992), one might hypothesize that the obviously different staining levels would most likely correspond to functional, rather than cellular markers. Thus, by studying the neurons within a system in which the electrophysiological profile has been documented, a direct exploration can be made of whether endogenous firing patterns are related to the abundance of calretinin and/or calbindin. Furthermore, because the location of neurons along two dimensions of the cochlear axis has significance for sensory coding (frequency along the cochlear axis, intensity orthogonal to the tonotopic map), the distribution of a protein, should it correspond to one or both of these patterns, would help to unravel its functional significance. Therefore, the spiral ganglion provides an ideal opportunity to explore the neuron-specific role of calcium binding proteins and, in turn, documenting

the distribution of calcium binding proteins in these cells could also reveal more about the neurons within this seemingly simple peripheral sensory ganglion.

Taking this approach, we determined that there is an intricate pattern of calcium binding protein labeling superimposed on the known distributions of intrinsic electrophysiological properties (Adamson et al., 2002b; Liu and Davis, 2007) and synaptic protein distributions (Flores-Otero et al., 2007; Flores-Otero and Davis, 2011). Overall, different levels of anti-calretinin and anti-calbindin labeling are documented within each region of the cochlea for type I spiral ganglion neurons, showing that calretinin levels were significantly higher in the middle while calbindin levels were relatively uniform across different regions. Surprisingly, we also noted that type II spiral ganglion neurons isolated from the apex with their distinct calcium binding protein profile having high calbindin and little to no calretinin, differed from type II neurons in the mid and basal regions. These observations indicate that within both classes of spiral ganglion neuron there resides additional dimensions of complexity revealed by their calretinin and calbindin levels, which adds to the rich diversity displayed by postnatal spiral ganglion neurons.

Calretinin and calbindin levels and intrinsic firing features

Both gain-of-function and loss-of-function studies have demonstrated the important roles that calretinin and calbindin have in shaping action potential parameters. For example, in the cerebellum, it was shown in knockout animals that endogenous calretinin elongates

the duration of action potentials and decreases the rate of sustained firing (Gall et al., 2003). Conversely, calbindin in hippocampal neurons attenuates the rapid afterhyperpolarization and reduces adaption of firing (Klapstein et al., 1998). Therefore, although the two calcium binding proteins have very similar structure and calcium binding kinetics (Cheung et al., 1993; Nägerl et al., 2000; Faas and Mody, 2012), they may play differential or even opposite roles in a neuron. If the same principles hold true for neurons within the spiral ganglion, one might expect that calretinin levels would be higher in the fast-accommodating basal neurons whereas calbindin would be higher in the slowly-accommodating apical neurons. Yet this was unequivocally not what we observed. Instead we found that calretinin staining levels were higher in the mid-cochlea region, which is also the most behaviorally sensitive region in the spiral ganglion. This finding suggested that levels of calretinin and calbindin were unlikely to be associated with firing accommodation of spiral ganglion neurons, but immediately raised the question of whether calretinin or calbindin levels were directly related to the intrinsic excitability.

To address this question, we compared the endogenous firing features and the levels of calretinin and calbindin in the same cell. Taking advantage of an established *in vitro* culture system that enabled the combination of electrophysiological recordings with immunocytochemical staining and analysis, we showed that staining levels of calretinin and calbindin alone were not correlated with excitability parameters such as resting membrane potential and firing threshold. Furthermore, no associations were noted

between the two calcium binding proteins and kinetic features of neuronal firing, such as action potential duration, time constant, latency and APmax. We did, however, find that the ratio of normalized calbindin staining irradiance to normalized calretinin staining irradiance showed a recognizable pattern that neurons with comparable relative levels of calretinin and calbindin tended to have longer time constants, while the calbindin/calretinin ratio of short-time constant neurons spanned a broader range. Therefore, the relative staining levels of calretinin and calbindin, but not their staining levels alone, may help distinguish slow-kinetics neurons from the fast-kinetics neurons in the spiral ganglion.

In the vestibular ganglion of the inner ear, calretinin and peripherin marked calyx-only and bouton-only afferent terminals and corresponding cell bodies, respectively, while calbindin labeled bouton-only and bimorph afferents (Kevetter, 2002; Leonard and Kevetter, 2002). Interestingly, a recent study showed that although calretinin labeled calyx-only fibers which are believed to be irreglular-firing and have a transient firing response to current steps, the protein itself may not be involved in the regulation of endogenous firing patterns of these neurons. Firing patterns of vestibular ganglion neurons of calretinin knockout mice showed no clear difference with that of wild type mice (Li and Eatock, 2013). Given the distribution of both calretinin and calbindin proteins in the spiral ganglion, we have taken the approach of directly assessing the relation between endogenous firing features and the levels of calretinin and calbindin in

wild type tissues, nevertheless, our findings are consistent with the results in the vestibular system, indicating that in the inner ear, levels of either calretinin or calbindin alone in primary neurons is unlikely to be directly associated with categories of intrinsic firing features.

It is known that the average time constant of spiral ganglion neurons increases from base to the apex (Liu and Davis, 2007). Consistent with this, 9 out of 12 neurons in the slow category, which exhibited longer time constants and comparable relative calbindin/calretinin staining levels, were obtained from the apical region. Although it was not possible to examine the identity of the neurons in these experiments with peripherin labeling due to the experimental protocol to stain both calcium binding proteins, it is interesting to ask how the calbindin/calretinin ratio correlates with the difference between type I and type II neurons since the slow-kinetics neurons make up a relatively small population. Nevertheless, because the neurons within this category possess comparable calretinin and calbindin levels, and clearly distinct from the high calbindin and low-calretinin profile of apical type II neurons that resulted in a relatively high calbindin/calretinin ratio, we surmise that it is unlikely that the subpopulation of slow time constant neurons could be solely attributed to type II neurons. Thus, the relationship between the calbindin/calretinin ratio and onset tau of a neuron may reflect heterogeneity amongst type I as well as type II neurons in all tonotopic regions.

Tonotopic variation of type II neurons

In this study, we have shown that type II neurons in the apex of the spiral ganglion possessed higher levels of calbindin and lower levels of calretinin than type II neurons from the middle and base. This observation is consistent with the distinctive nature of apical type II neurons which differ from type II neurons in other regions in the cochlea. For example, the peripheral fibers of apical type II neurons turn both apically and basally when they reach the outer hair cell region and form synapses with both outer hair cells and support cells, while type II afferents in the middle and base region consistently turn towards the base and connect only with outer hair cells (Burgess et al., 1997; Fechner et al., 2001; Nayagam et al., 2011). Furthermore, the intrinsic properties of type II neurons in cultures prepared from isolated regions of the spiral ganglion showed that type II neurons were not all identical. The apical type II neurons exhibited firing features with faster kinetics and higher firing threshold than basal type II neurons (Reid et al., 2004). Taken together, the distribution patterns of calretinin and calbindin highlighted another aspect of the tonotopic difference among type II neurons, further indicating that type II neurons may also possess specific features that may enable this relatively small population to convey complex sensory information to higher centers.

Local heterogeneity superimposed on tonotopic and intensity map

In addition to the well-known tonotopic specializations within the cochlear duct, the spiral ganglion possesses another orthogonal dimension of spatial organization consistent with the parameters required to build an intensity map. In the cat, neuronal cell bodies of

auditory nerves with different spontaneous rates showed a topographic organization in the spiral ganglion such that low and medium spontaneous rate neurons tended to cluster in the scala vestibuli side, and high spontaneous rate neurons were more likely to reside in the scala tympani side (Leake and Synder, 1989; Leake et al., 1992). Because the endogenous features of voltage threshold and resting membrane potential that contribute to neuronal excitability might logically contribute to intensity coding, we reasoned that the lack of a clear correlation between neuron excitability and calcium binding protein irradiance levels would make it unlikely that calretinin or calbindin would be distributed systematically along the scala tympani-vestibuli axis. This is what we found, which is consistent with the idea that calretinin and calbindin levels do not relate to the distinctive categories of spontaneous rate displayed by spiral ganglion neurons (Liberman, 1978; Taberner and Liberman, 2009).

The presynaptic protein, synaptophysin, was previously shown to be graded in both tonotopic and scala vestibuli to scala tympani axes, such that an orthogonal scala vestibuli to scala tympani gradient was superimposed on the average levels of anti-synaptophysin staining irradiance that increased from base to apex (Flores-Otero and Davis, 2011). Therefore, in a restricted tonotopic region, the level of synaptophysin may correlate with the location of neuronal cell body in the ganglion, and, thus, with spontaneous rates of the auditory nerve. To further confirm that levels of calretinin or calbindin were not associated with spontaneous rate of the auditory nerve in mouse

cochlea, we also examined the spatial organization of anti-calretinin and anti-calbindin antibody staining irradiance and their co-labeling patterns with anti-synaptophysin antibody staining. Co-labeling of either calretinin or calbindin antibodies with synaptophysin antibody in neuronal cultures, expectedly, did not reveal any association of staining levels (data not shown). Therefore, both our electrophysiological and immunocytochemical results indicate that neither calretinin nor calbindin levels are associated with spontaneous rate in the murine spiral ganglion.

Although we have shown that the local heterogeneity revealed by anti-calretinin and anti-calbindin staining patterns of calretinin and calbindin could not be related to the known intensity map, it remains possible that calretinin and calbindin could associate with other functional features or differentially regulate electrophysiological events beyond membrane responses at neuronal cell soma. There is growing evidence that spiral ganglion neurons are heterogeneous in terms of their protein profile (Romand et al., 1990; Järlebark et al., 2000; Khan et al., 2002; Khalifa et al., 2003; Inoue et al., 2006), and that type I and type II neurons could possess distinct distribution patterns of proteins crucial to the membrane properties, such as Na/K ATPase and sodium channels (Fryatt et al., 2009; McLean et al., 2009). In this context, the distribution of calretinin and calbindin may be related to, or be indicative of, a repertoire of functional differences within the spiral ganglion independent of the known tonotopic and intensity maps.

For example, in addition to their direct role of shaping neuronal firing in cerebellar

granular cells and hippocampal neurons, as described above, calretinin and calbindin are also involved in indirect regulation of cellular function. Loss of calretinin impairs synaptic plasticity in dentate gyrus without affecting basal synaptic transmission (Schurmans et al., 1997), and tissue specific calbindin overexpression in the same region leads to an increase of presynaptic strength and reduction of long-term potentiation (Dumas et al., 2004). The central projections of spiral ganglion neurons form connections with highly diverse targets in the cochlear nucleus, and the morphological features of their fiber endings could vary independent of their characteristic frequency and spontaneous rate (Rouiller et al., 1986; Ryugo and Rouiller, 1988; Liberman, 1991; Ryugo, 1992).

In summary, this study suggests that different levels of calretinin and calbindin do correlate with specific subpopulation of cells, and may lead to a better understanding of the functions in apical type II neurons in particular. Moreover, the door is still open for an association with the heterogeneity of intrinsic and synaptic properties among spiral ganglion neurons, and our findings may help to reveal a novel dimension of complexity that may serve as the cellular basis for additional neuronal processing in the primary auditory nerve.

Chapter 4

Induction and characterization of neuronal-like phenotype in cochlear epithelial cells

The past decade has witnessed ground-breaking progress in the field of cell fate reprogramming. It has been shown that in fully differentiated mammalian cell types, overexpression of defined combinations of transcription factors is sufficient to either induce retrodifferentiation and enable the cells to regain pluripotency (Takahashi and Yamanaka, 2006), or evoke transdifferentiation that directly convert the cells into another distinctive lineage (Zhou et al., 2008; Vierbuchen et al., 2010). The therapeutic potential of these findings is that samples obtained with non-invasive methods from human patients could be used to generate a variety of cell and tissue types, thus providing *in vitro* models for disease mechanism and potential source of cell replacement (Ming et al., 2011). Additionally, the concept and the approach of cell fate reprogramming may also contribute to the investigation of the molecular mechanism underlying cell fate specification (Rouaux and Arlotta, 2013).

During the development of mammalian inner ear, spiral ganglion neurons are derived from precursors in the embryonic otocyst, under the regulation of a hierarchy of transcription factors such as Neurogenin1 (Neurog1) and NeuroD1 (Kelley, 2006; Appler and Goodrich, 2011; Bermingham-McDonogh and Reh, 2011). It has been shown that,

non-sensory epithelial cells in the cochlea, which originate from a lineage closely related to the spiral ganglion neurons (Fig. 4.1), can be redirected to a neuronal-like identity *in vitro* when the transcription factor Neurog1 or NeuroD1 were overexpressed in embryonic tissues using electroporation. Of the cochlear epithelial cells transfected with *Neurog1* or *NeuroD1*, 73% and 26% respectively, were positive of the neuronal marker β-III-tubulin (Puligilla et al., 2010). Thus, neuronal-like cells could be made from an abundant cell pool in the inner ear, and the comparison of these induced cells with endogenous spiral ganglion neurons would further the understanding of requirements for specific firing features in the auditory primary afferents.

About 30% of cochlear epithelial cells transfected with *Neurog1* showed sodium channel mediated inward current in whole-cell voltage clamp recordings, which is characteristic of a neuronal-like membrane response (Puligilla et al., 2010). Due to the relatively low efficiency of Neurog1 and NeuroD1 to induce neuronal-like phenotype, other factors may be used to enable a systematic comparison with the well characterized firing features of endogenous spiral ganglion neurons. It was reported that overexpression of the bHLH transcription factor Ascl1 alone was sufficient to induce neuronal-like electrophysiological properties in murine fibroblasts (Vierbuchen et al., 2010). Therefore we characterized the electrophysiological effect of *Ascl1* overexpression in embryonic cochlear epithelial cells in comparison with firing features of endogenous spiral ganglion neurons.

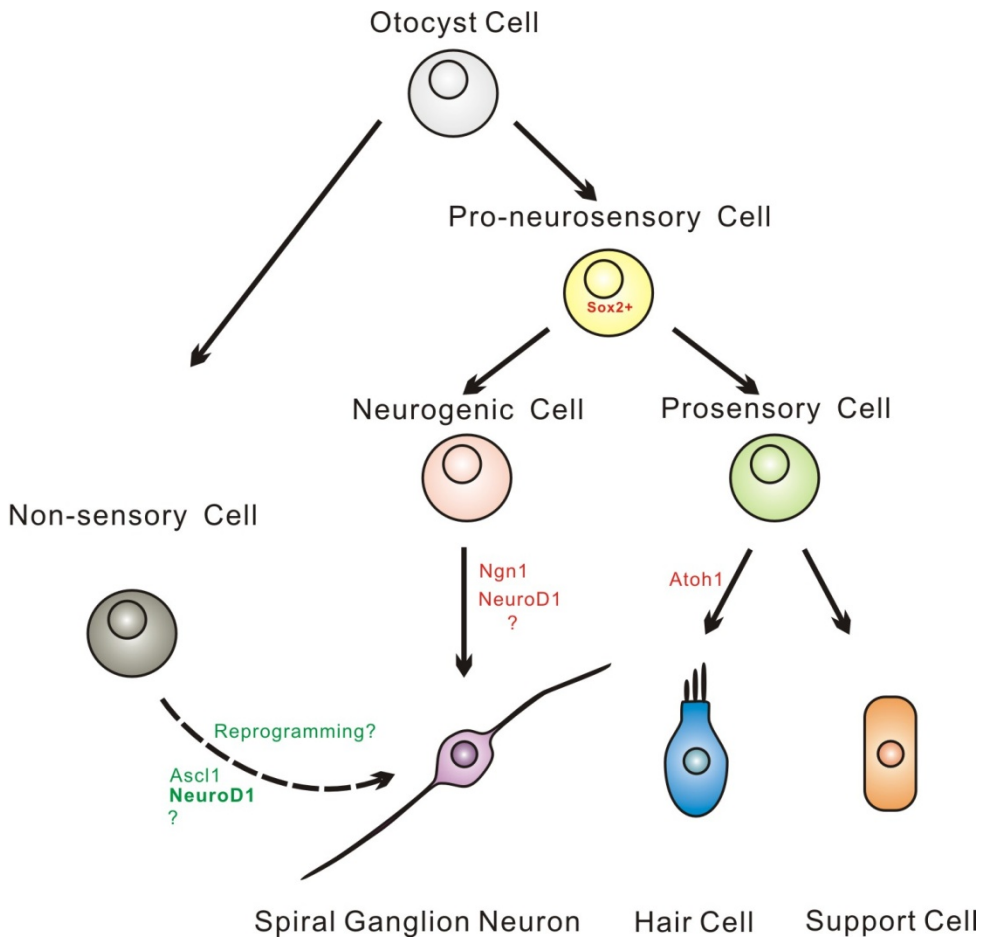

Figure 4.1: Cochlear non-sensory epithelial cells may be reprogrammed into spiral ganglion neurons. Spiral ganglion neurons derive from the pro-neurosensory region of the otocyst and require a series of specific factors such as Neurogenin 1 and NeuroD1 to acquire neuronal fate. The cochlear non-sensory epithelial cells, which are from a lineage closely related to the neuronal lineage, may be engineered into a neuron-like cell type by overexpression of transcription factors. The efficiency of neuronal induction may be improved using refined combination of different factors.

To investigate whether the overexpression of *Ascl1* in cochlear epithelial cells induces membrane properties resembling that of endogenous spiral ganglion neurons, we compared electrophysiological recordings of *pCIG-Ascl1* transfected cells and control recordings made from cells transfected with *pCIG* empty vector. A total number of 13 control recordings consistently showed limited or no voltage-dependent whole-cell currents (n=8; Fig. 4.2B) under voltage clamp configuration. This observation was substantiated by ohmic responses observed in current clamp mode (Fig. 4.2C), which are consistent with passive membrane properties. In contrast, *Ascl1* transfected cells exhibited significant voltage dependent whole cell conductances (Fig. 4.2E-F). All recorded cells exhibited voltage-dependent outward currents and 16 out of a total of 22 recordings (72.7%, Table 4.1) showed inactivating inward currents characteristic of an excitable cell. Whole-cell conductance measurements could be made from a sub-set of the recordings and revealed an average inward conductance of 3.84±0.82 nS (n=9) and average outward conductance of 17.63±2.30 nS (n=14) and 9.34±1.75 nS at the peak and plateau, respectively. Moreover, action potential profiles were observed in *Ascl1* transfected cells in current clamp mode (Fig. 4.2G). Action potentials (n=5) in the *Ascl1* transfected cells showed longer overall latency (50.0±10.8ms) and duration (7.7±2.1ms) than endogenous postnatal spiral ganglion neurons (Adamson et al., 2002; Latency: 14.2±0.7ms in the base, 31.1±3.0 ms in the apex; duration: 1.72±0.1 ms in the base, 2.2±0.2 ms in the apex).

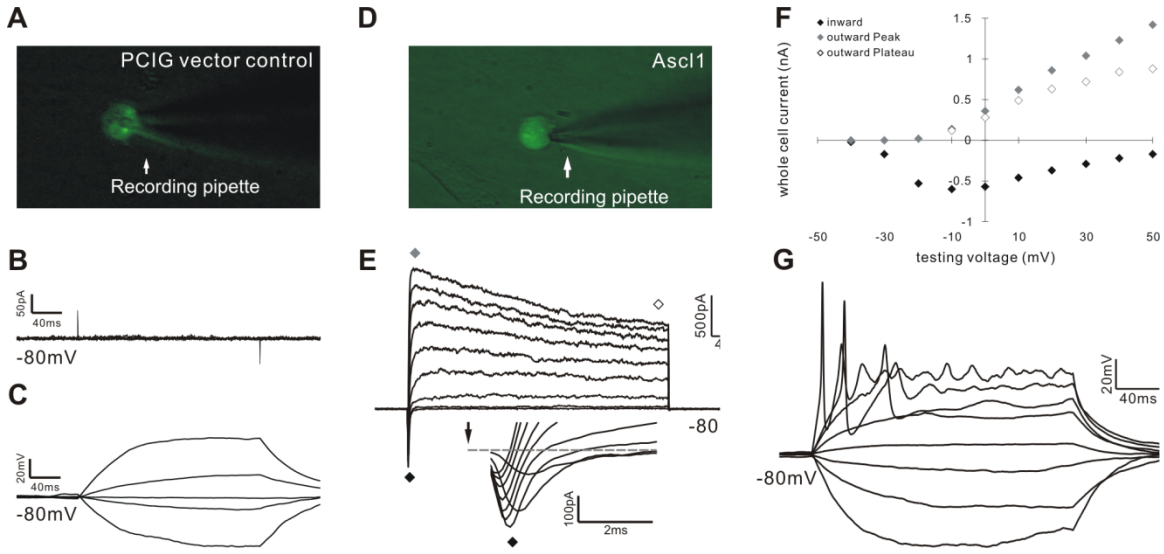

Figure 4.2: Ascl1 induced neuronal-like phenotype in cochlear non-sensory epithelial cells. Dissociated E13 cochlear epithelial cells overexpressing Ascl1 or empty vector were recorded on DIV 4. **A**, A merge image of Hoffman contrast and green fluorescence shows a recording pipette patching on a GFP positive cell transfected with an empty vector. **B**, The same cell in **A** showed very limited whole cell currents when depolarized with steps of -30mV to 50mV from -80mV holding potential. **C**, Whole cell current clamp recordings from the same cell showed ohmic passive membrane responses to current injections of -4pA to 4pA at -80mV holding potential. **D**, A merge image of Hoffman contrast and green fluorescence shows an Ascl1 transfected GFP positive cell with an attached recording pipette. **E**, Both voltage-dependent whole cell outward currents and inactivating whole cell inward currents (black diamond) were observed in the cell in **D** when depolarized with steps of -30mV to 50mV from -80mV holding potential. **Inset**, A high magnification view of the inward currents in **E**. Arrow indicates the onset of stimulus. Initial portion of the traces with capacitive transients were removed. **F**, Whole cell voltage-current relation of the recording shown in **E**. The peak (gray diamond) and plateau (open diamond) of outward currents were measured at different positions of the traces as indicated in **E**. **G**, Immature action potentials were revealed in current clamp recording from the same cell as in **D** and **E**. The cell was held at -80mV and injected with currents ranging from -3pA to 22pA.

The basic helix-loop-helix family transcription factor *NeuroD1* is a key factor required for the development of auditory neurons (Kim et al., 2001; Appler and Goodrich, 2011), and overexpression of *NeuroD1* is sufficient to induce TuJ1 staining in cochlear epithelial cells (Puligilla et al., 2010). To examine whether *NeuroD1* overexpression would also induce neuronal membrane properties, we recorded from cochlear epithelial cells transfected with a *pCLIG-NeuroD1* vector. Nine out of 12 recordings showed voltage-dependent whole cell currents; while 8 cells exhibited different levels of outward currents, only 2 cells displayed a slow, low amplitude inward current (Table 4.1). Whole-cell conductance measurements were made when possible and revealed average whole cell outward conductance of 13.6±6.4nS (n=5) and 6.8±4.0nS (n=5) at the peak and plateau, respectively. Both fast-inactivating and slow-inactivating kinetics of the outward currents were observed (Fig. 4.3). Overall, unlike *Ascl1*, overexpression of *NeuroD1* alone was not able to induce neuronal-like membrane properties in cochlear epithelial cells.

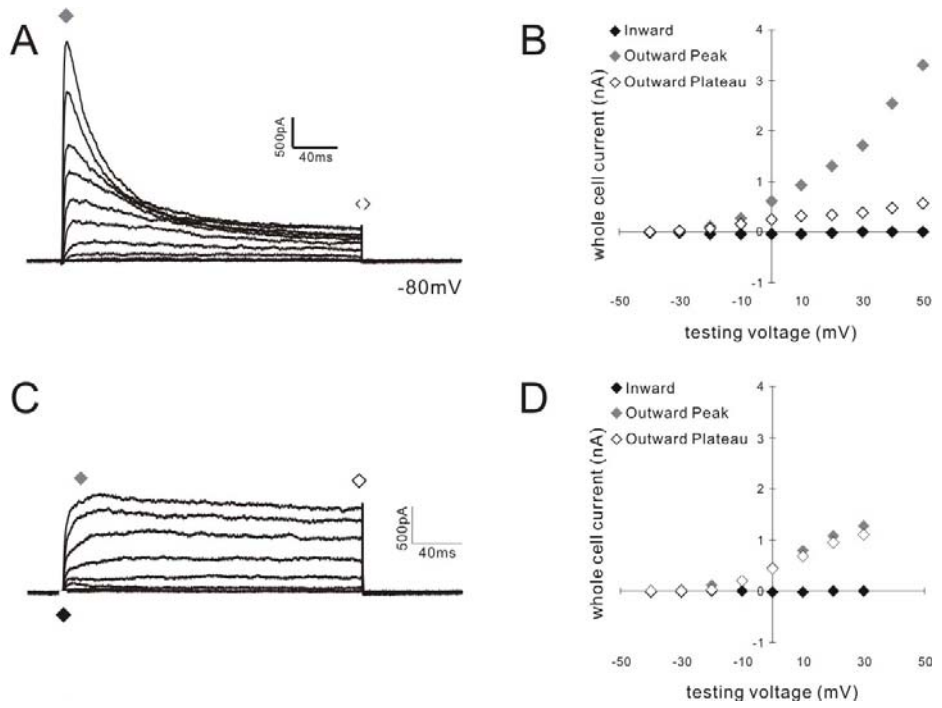

Figure 4.3: NeuroD1 transfection induced different types of outward currents. A, Recording from a NeuroD1 transfected cell on DIV4 showed large inactivating outward currents but no inward currents in response to depolarization from -40mV to 50mV. **B,** current-voltage relation of the recording in **A**. **C**, Another example of a recording from a NeuroD1-transfected cell that displayed slowly inactivating outward currents under voltage steps from -40mV to +30mV. **D**, current-voltage relation of the recording in **C**.

It was recently reported that the overexpression of *NeuroD1* alone in human fibroblasts did not have a notable effect; however, its combination with other factors significantly improved the efficiency of neuron induction (Pang et al., 2011). Therefore we asked whether the combination of *NeuroD1* with *Ascl1* could improve the induction of neuron-like membrane properties in cochlear epithelial cells. Whereas as slightly lower percentage of *Ascl1-NeuroD1* double transfected cells (57.7%, Table 4.1) showed inward currents (Fig. 4.4B) compared to those transfected with *Ascl1* only, the average inward whole cell conductance (4.26±1.03 nS, n=11) and average outward conductance at peak (22.72±3.90 nS, n=19) and plateau (15.68±3.34 nS, n=19) in the double transfected cells

showed a slight trend toward larger conductances but were not significantly different (p>0.10). Action potential profile of the *Ascl1-NeuroD1* double transfected cells (latency: 52.9±14.4ms; duration: 5.1±1.9ms; n=4; Fig. 4.4E) was comparable to that of the *Ascl1* transfected cells described above. Inward currents could be abolished by the application of tetrodotoxin (Fig. 4.4C), suggesting that a robust Na^+ current contributes to the action potential profiles observed in whole-cell current clamp recordings (Fig. 4.4E). Furthermore, in both *Ascl1* and *Ascl1-NeuroD1* transfected cells there were clear indications of hyperpolarization-induced voltage sag and, in an example with double transfection (Fig. 4.4F), rebound action potentials were also observed. Both results are suggestive of the presence of I_h, which were also reported in spiral ganglion neurons (Chen, 1997; Mo and Davis, 1997; Liu and Davis, 2007).

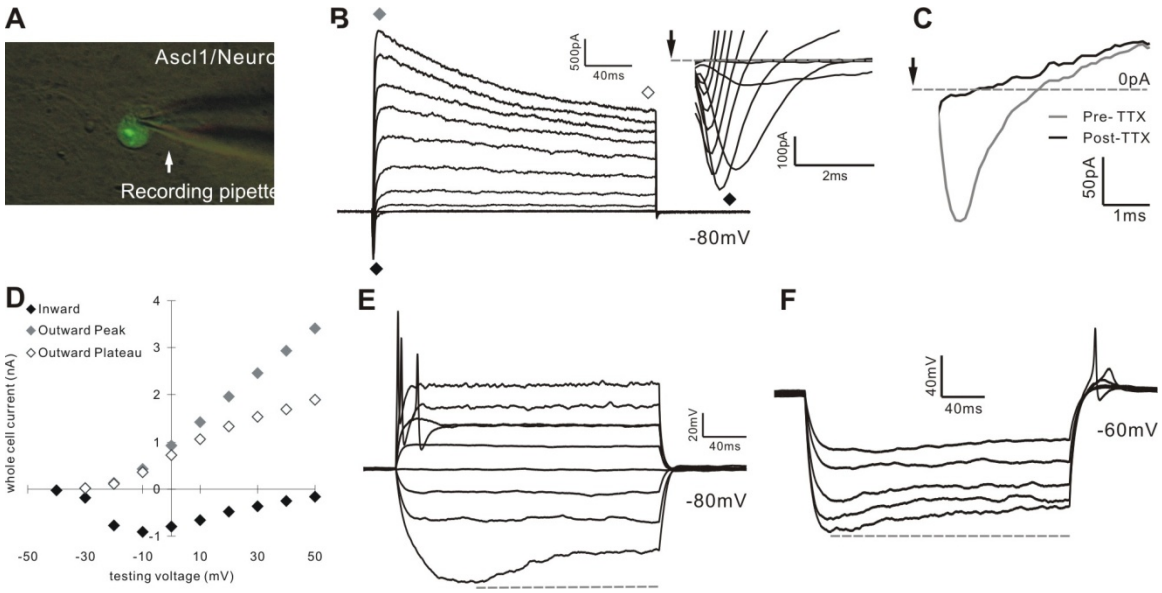

Figure 4.4: The combination of Ascl1 with NeuroD1 could induce neuronal-like phenotype. Representative recording from an E13 cochlear cell transected with *Ascl1* and *NeuroD1* (DIV 8). **A**, Merge image of Hoffman contrast and green fluorescence shows a recording pipette patching on a GFP positive cell. **B**, Whole cell voltage clamp traces from the same cell as in **A**. The cell exhibited large inward and outward whole cell current when depolarized with steps of -50mV to 50mV from -80mV holding potential and. **Inset**, Inactivating inward currents shown in a high magnification view of the traces in **B.** **C**, Inward currents at the peak level (with depolarization to -10mV from -80mV holding potential) could be completely abolished by 1uM TTX. Gray, before drug application; black, after drug application. In **B inset** and **C**, arrow indicates the onset of stimulus. Initial portion of the traces with capacitive transients were removed. **D**, Whole-cell voltage-current relation of the recording shown in **B**. The peak (gray diamond) and plateau (open diamond) of outward currents were measured at different positions of the traces as indicated in **B**. **E**, Whole cell current clamp recordings from the same cell. Currents ranging from -65pA to 420pA were injected while the cell was held at -80mV. **F**, Hyperpolarizing sag and a rebound spike was observed in an exemplifying current clamp recording from an *Ascl1-NeuroD1* double transfected cell, which was held at -60mV and hyperpolarized by -60pA to -190pA current injection.

Table 4.1: Efficiency of neuronal-like phenotype induction of different factors

transfection	pCIG vector	Ascl1	NeuroD1	Ascl1-NeuroD1
total No. of recordings	13	22	12	24
cells with inward current	0	16	2	14
percentage	0	72.73%	16.7%	58.33%

With either *Ascl1* single or *Ascl1-NeuroD1* double overexpression, action potentials were unequivocally induced in cochlear epithelial cells, most of which had relatively immature features compared to postnatal spiral ganglion neuron *in vitro*. However, more than 30% of all available current clamp recordings (3 out of the 9, Table 2), showed action potential latency comparable to early postnatal spiral ganglion neurons, the average latency of which was 14.8±1.5ms in the base and 30.7±2.8ms in the apex (Adamson et al., 2002b). Furthermore, although 8 recordings showed prolonged action potential duration compared to postnatal spiral ganglion neurons, one cell exhibited brief action potential duration that could match the profile of an average basal neuron (Fig. 4.5A). This observation suggested that, although the overexpression of *Ascl1* and *NeuroD1* may not be sufficient to implement cochlear epithelial cells with the repertoire of whole cell conductances of endogenous spiral ganglion neurons, it could induce excitable membrane properties that closely resemble a spiral ganglion neuron with fast firing kinetics. To evaluate this more closely we compared the action potentials parameters and whole cell conductances from eight recordings transfected with either *Ascl1* alone or in combination with *NeuroD1*, and found that those with the largest whole-cell peak outward conductances displayed firing parameters with the fastest latency (R^2=0.81; Fig. 4.5B), and those with the largest inward conductance possessed the greatest action potential amplitudes (R^2=0.45; Fig. 4.5C). There is also a trend that the latency is negatively correlated with inward conductance (R^2=0.40; Fig. 4.5D). We therefore expect that with larger whole cell inward and outward conductances, the

electrophysiological profile of the induced neuronal-like cells will progressively resemble that of a typical spiral ganglion neuron. Moreover, we also noted recordings with prominent hyperpolarizing sags, suggesting that these induced neuronal-like cells may also possess I_h currents that play important roles in the regulation of firing threshold in endogenous postnatal neurons (Liu et al., 2012). No significant correlation was observed between latency and voltage threshold (R^2=0.07; Fig. 4.5E), indicating that the timing-related parameters and excitability-related parameters may be regulated separately in these cells, consistent with the findings of others (Liu et al., 2014).

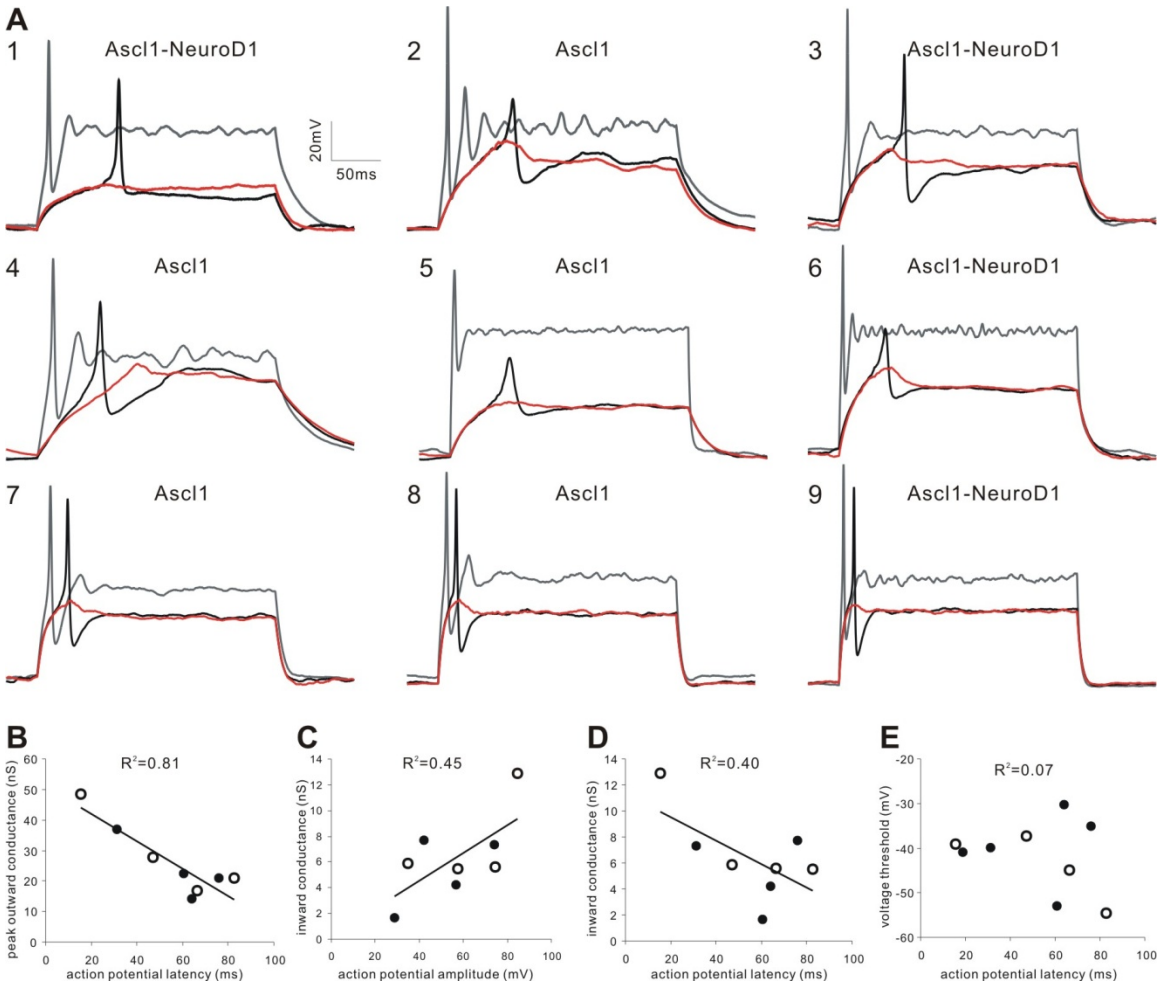

Figure 4.5: Diverse range of firing features in non-sensory epithelial cells with Ascl1 or Ascl1-NeuroD1 overexpression. A, Examples of whole cell current clamp recordings from non-sensory epithelial cells transfected with *Ascl*1 or *Ascl1* and *NeuroD1*, showing sub-threshold response (red), threshold action potential (black) and supra-threshold trace with the maximum number of spikes (gray). Recordings are numbered according to their action potential latency, from the longest (1) to the shortest (9); indicated in **Table 2**. Scale in panel 1 applies to all recordings. **B-D**, Action potential latency plotted against peak outward conductance (**B**), voltage threshold (**D**) and whole cell inward current conductance (**E**). **C**, Action potential amplitude plotted against whole cell inward conductance. Closed circles represent data points from cells transfected with *Ascl1*; open circles represent data from cells double transfected with *Ascl1-NeuroD1*. R^2 values of linear fits for each relation were calculated from the combined data set. All electrophysiological parameters were measured at threshold with -80mV holding potential. Conductance measurements were made in 7 out of 8 recordings.

Table 4.2: Membrane properties of Ascl1 or Ascl1-NeuroD1 transfected cells.

No.	transfection	action potential properties				Whole-cell conductance(nA)			inward current peak amplitude (nA)
		latency (ms)	threshold (mV)	duration (ms)	amplitude (mV)	inward	outward peak	outward Plateau	
1	Ascl1-NeuroD1	**82.70**	-54.66	4.00	57.29	5.50	21.04	16.91	-0.54
2	*Ascl1*	***75.80***	*-35.06*	*12.60*	*42.01*	*7.69*	*20.86*	*17.19*	*-0.58*
3	Ascl1-NeuroD1	**66.30**	-44.97	3.90	74.50	5.61	16.97	13.70	-0.41
4	Ascl1	**64.00**	-30.17	6.80	56.49	4.22	14.12	11.30	-0.31
5	Ascl1	**60.60**	-52.93	12.70	28.76	1.64	22.39	19.52	-0.16
6	Ascl1-NeuroD1	**47.10**	-37.34	10.50	34.93	5.90	27.89	25.85	-0.45
7	Ascl1	**31.10**	-40.00	3.50	74.07	7.32	37.03	21.38	-0.59
8	Ascl1	**18.70**	-40.87	2.80	82.03	N.A	N.A	N.A	-0.08
9	*Ascl1-NeuroD1*	***15.50***	*-39.03*	*2.00*	*84.69*	*12.90*	*48.41*	*31.88*	*-0.88*

Chapter 5

Firing Features of Spiral Ganglion Neurons in Acute Preparation

Previous work from our lab has taken a reductionist approach to break the system apart and closely examine the properties of isolated spiral ganglion neurons. After dissecting out the spiral ganglion and the organ of Corti from the bony walls, we further remove the hair cells and support tissues, isolated explants of neurons in different tonotopic position, and keep them in culture for 6-7 days. Taking advantage of this highly defined and accessible culture system, we have been able to document systematic patterns of firing features, based on an array of different parameters, which, interestingly, could be changed by adding exogenous growth factors (Mo and Davis, 1997; Adamson et al., 2002a, 2002b; Liu and Davis, 2007; Liu et al., 2013). A recent study from the lab reported a composite snapshot of spiral ganglion neuron firing in a variety of different conditions, in which the highly diverse firing behaviors of spiral ganglion neurons coalesced *in vitro* into three accommodation categories (Crozier and Davis, 2014). Slow accommodation (SA) group fired action potentials throughout a sustained current injection (240ms) whereas rapidly accommodation (RA) group ceased firing during the pulse. A special sub-group of the rapidly accommodation category only fired a single spike at the beginning of the depolarization, and were thus termed unitary accommodation (UA). The relative proportion of the three classes was regulated during

development and could be shifted by the application of neurotrophin-3 (NT-3), suggesting that the spiral ganglion may possess coding capacities that are both diverse and dynamic.

Intrinsic Firing Properties of Spiral Ganglion Neurons in an Acute OC-SGN Preparation

A question that immediately followed this observation is that whether the rich repertoire of firing features observed in cultured isolated neurons reflect the conditions in the animal. To address this question, we recorded from neuron somata in acute spiral ganglion preparations, in which the afferent connection to the Organ of Corti was intact (Fig. 5.1). In a subset of experiments, the recorded neuron could be intracellularly labeled and stained *post hoc* to assess its structural integrity. This preparation will be referred to as OC-SGN in the following sections.

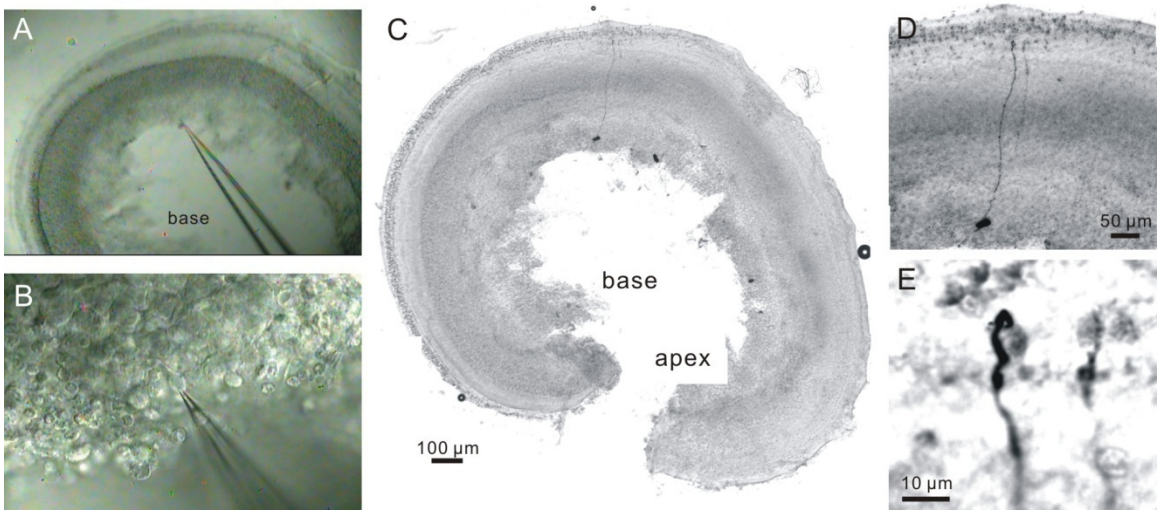

Figure 5.1: A representative recorded neuron from the acute OC-SGN preparation. **A-B**, Low (**A**) and high (**B**) magnification images of a recording electrode patched on P2 mid-turn neuron in the acute OC-SGN preparations. **C-E**, Intracellular labeling of the same neuron shown in **A-B** using biocytin filling and streptavidin mediated horseradish peroxide (HRP) reaction (see Chapter 2). **D**, The neuronal somata and the afferent fiber approaching the hair cell region. **E**, High magnification image of the afferent synaptic bouton.

We first utilized the acute OC-SGN preparation to systematically examine the intrinsic firing properties of spiral ganglion neurons and compare them to the known patterns observed in cultured neurons. Interestingly, when the relationship between accommodation (represented by AP_{max}, see Chapter 2) and inter-spike interval (ISI) was examined, a pattern very similar to that observed in the neuronal culture has emerged (Figure 5.2A). Regardless of animal age, tonotopic position and holding potential settings during recording, spiral ganglion neurons in the acute preparation exhibited firing patterns that could be classified into the slowly accommodation (SA), rapidly accommodation (RA) and unitary accommodation (UA) groups. The SA and RA groups spanned the same broad range of inter spike interval (5-30ms) while the ISI and AP_{max} of

SA neurons displayed a negatively correlated function. This result validated our previous *in vitro* data and strongly suggested that the membrane properties of spiral ganglion neurons were comparable between acute preparations and culture conditions (DIV 6-7).

We also investigated the age related change of firing features for early postnatal spiral ganglion neurons. To highlight the diverse firing patterns in a comparable manner, we focused on recordings obtained at -60 mV holding potential. When the data was split into age groups of postnatal 0 to 3 days (P0-3) and P4-8, a progression of firing features could be observed (Fig. 5.2B-F). Compared to P0-3 neurons, P4-8 neurons showed significantly smaller interspike interval (average ISI: P0-3, 13.23±0.45ms, n=104; P4-8, 7.61±0.31ms, n=86. $P<0.01$), fired more action potentials during the test pulse (Fig 5.2C, average AP_{max}: P0-3, 9.37±0.62, n=104; P4-8, 13.35±0.68, n=86. $P<0.01$) with faster time constants (Fig 5.2D, average latency: P0-3, 15.35±0.42ms, n=95; P4-8, 9.63±0.55ms, n=81, $P<0.01$) and shorter durations (Fig 5.2E, average duration: P0-3, 2.06±0.07ms, n=95; P4-8, 1.34±0.08ms, n=81. $P<0.01$), and elicited spikes at more hyperpolarized voltages (Fig. 5.2F, average voltage threshold: P0-3,-44.23±0.37mV, n=95; P4-8,-46.82±0.42mV, n=81. $P<0.01$). However, percentage of neurons in each of the accommodation categories did not show a significant difference between the two age groups (P0-3, 4.8% UA, 42.3% RA, 52.9% SA; P4-8, 9.3% UA, 43.0% RA, 47.7% SA. Chi-square test for homogeneity, $P=0.43$).

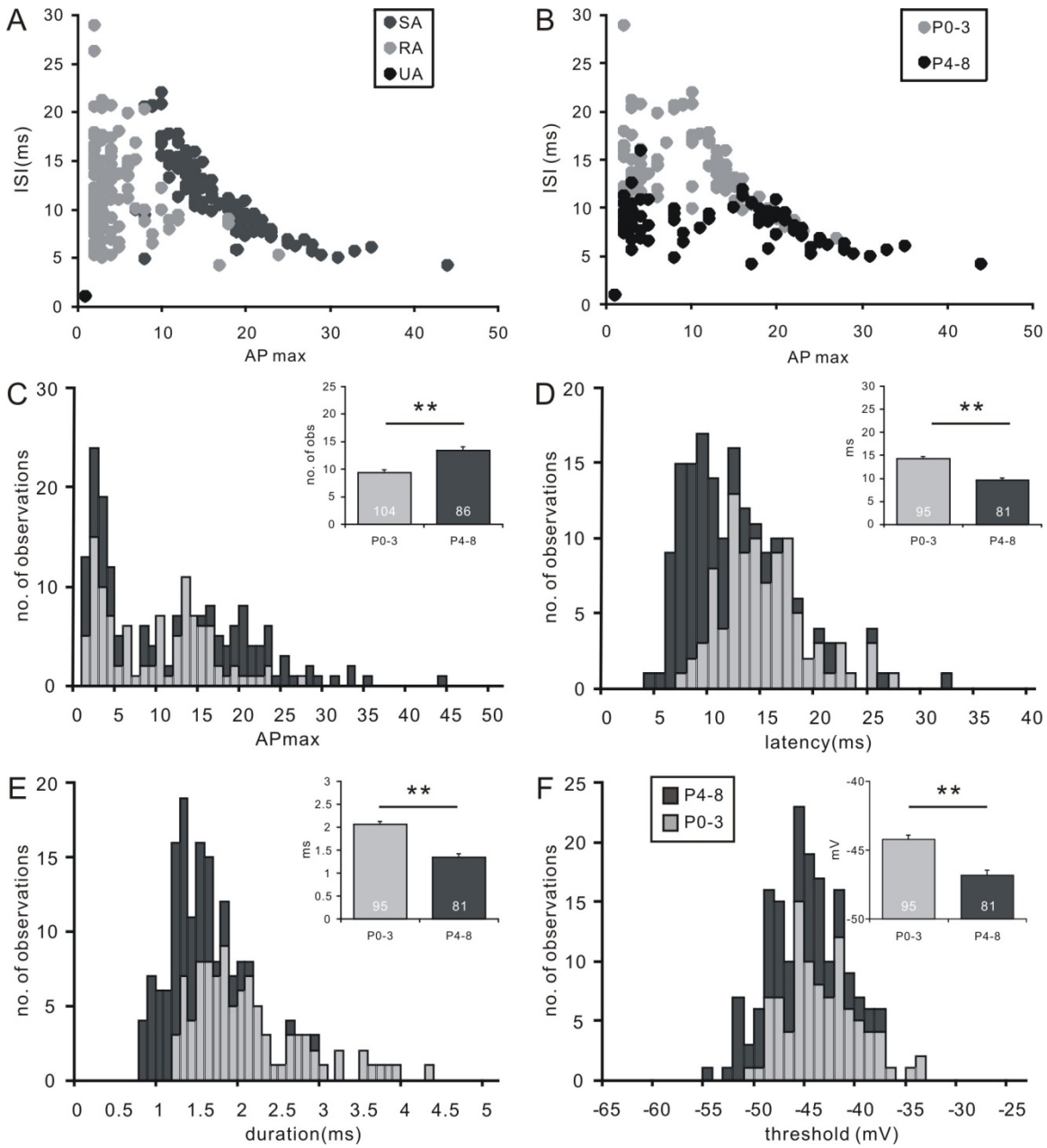

Figure 5.2: Intrinsic firing features of spiral ganglion neurons in the acute OC-SGN preparation. A, The relation between maximum number of spikes (AP_{max}) and the temporal difference between the first and second spike (interspike interval, ISI) for 332 experimental paradigms obtained from neurons in P0-8 OC-SGN preparations. Recordings with both -80mV and -60mV holding potentials were included. **B**, Relation between ISI and AP_{max} revealed a developmental shift of the proportion of cells in different accommodation modes. All recordings were made under -60mV holding potential. **, P<0.01. **C-F**, Frequency histograms and average values (inset) of AP_{max} (**C**),

voltage threshold (**D**), latency (**E**) and duration (**F**) of recordings obtained from OC-SGN preparations displayed differences between P0-3 and P4-8 groups.

Based on the structural integrity of the acute preparation, we were also able to characterize the difference of intrinsic membrane properties between type I and type II spiral ganglion neurons. With intracellular labeling, the innervation patterns of recorded cells could be unequivocally determined *post hoc*. In one such example (Fig. 5.3), a type I neuron and a type II neuron were recorded from the middle region of a P7 cochlea. Both neurons displayed slow accommodation at -60mV holding potential. At -80mV holding potential, however, the type I neuron converted to the rapidly accommodating category while the type II neuron still retained the firing features at more depolarized baseline. Moreover, as demonstrated in the example recording, the type II neuron exhibited large afterhyperpolarization during the repolarizing phase of the action potential compared to the type I counterparts. The distinctive firing features of type I and type II neurons could be recognized in greater detail when both the shape of action potential and the rate of voltage change were compared between the two categories at each neuron's threshold level (Fig. 5.4A). To render this information, we constructed phase plots for each action potential, in which voltage change was plotted against membrane voltage, giving a measurement of net current across the cell membrane at different voltage levels (Fig. 5.4C). Ten recordings obtained from P6-7 preparations each showed consistent firing profiles that were distinctive between neurons, and the category of each cell was identified by biocytin staining (Fig. 5.4B-C). Type I cells showed shorter spike latency,

larger action potential amplitude and faster kinetics in both depolarizing and repolarizing phases at -80mV holding potential, indicating larger sodium and delayed-rectifier potassium conductances in the type I neurons. On the other hand, the characteristic large AHP and longer latency was consistent among type II neurons. It is known that calcium-activated potassium channels contribute to I_{AHP} and regulate firing frequency, and A-type potassium currents (I_A) was known to both prolong the spike latency and enhance the amplitude of AHP (D'Angelo et al., 1998; Shibata et al., 2000). As large conductance Ca^{2+} activated K^+ channels and Kv4.2 channels were shown to be present in the murine spiral ganglion (Adamson et al., 2002b), our results further suggest that type I and type II neurons may possess distinct firing capabilities with differential levels of K_{Ca} channels and A-type K channels.

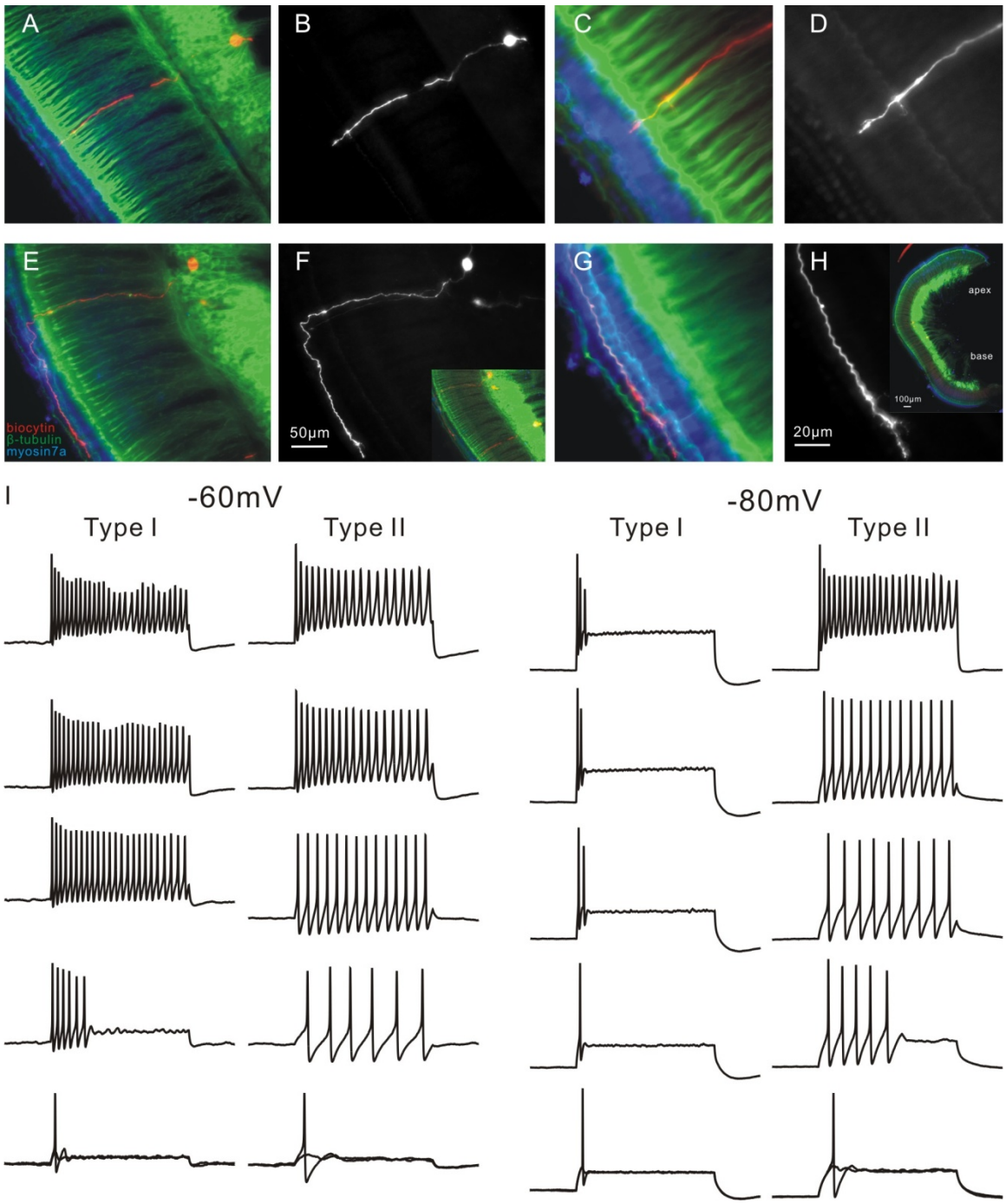

Figure 5.3: Recordings from type I and type II neurons in the acute OC-SGN preparation. A-H, Low (**A-B, E-F**) and high (**C-D**) magnification image of recorded type I (**A-D**) and type II (**E-H**) neurons in the middle region of a P7 OC-SGN preparation. Recorded neurons were highlighted by biocytin filling, showing the process trajectory (**B, D**) and postsynaptic terminals (**D,H**). The peripheral process of a type II neuron extended to the outer hair cell region and turned towards the base. **E,F insets**, Low magnification images of the preparation. **I**, Intrinsic firing feature of the corresponding cell under -60mV

and -80mV holding potentials. For each recording paradigm, traces for voltage steps from threshold to AP max are shown.

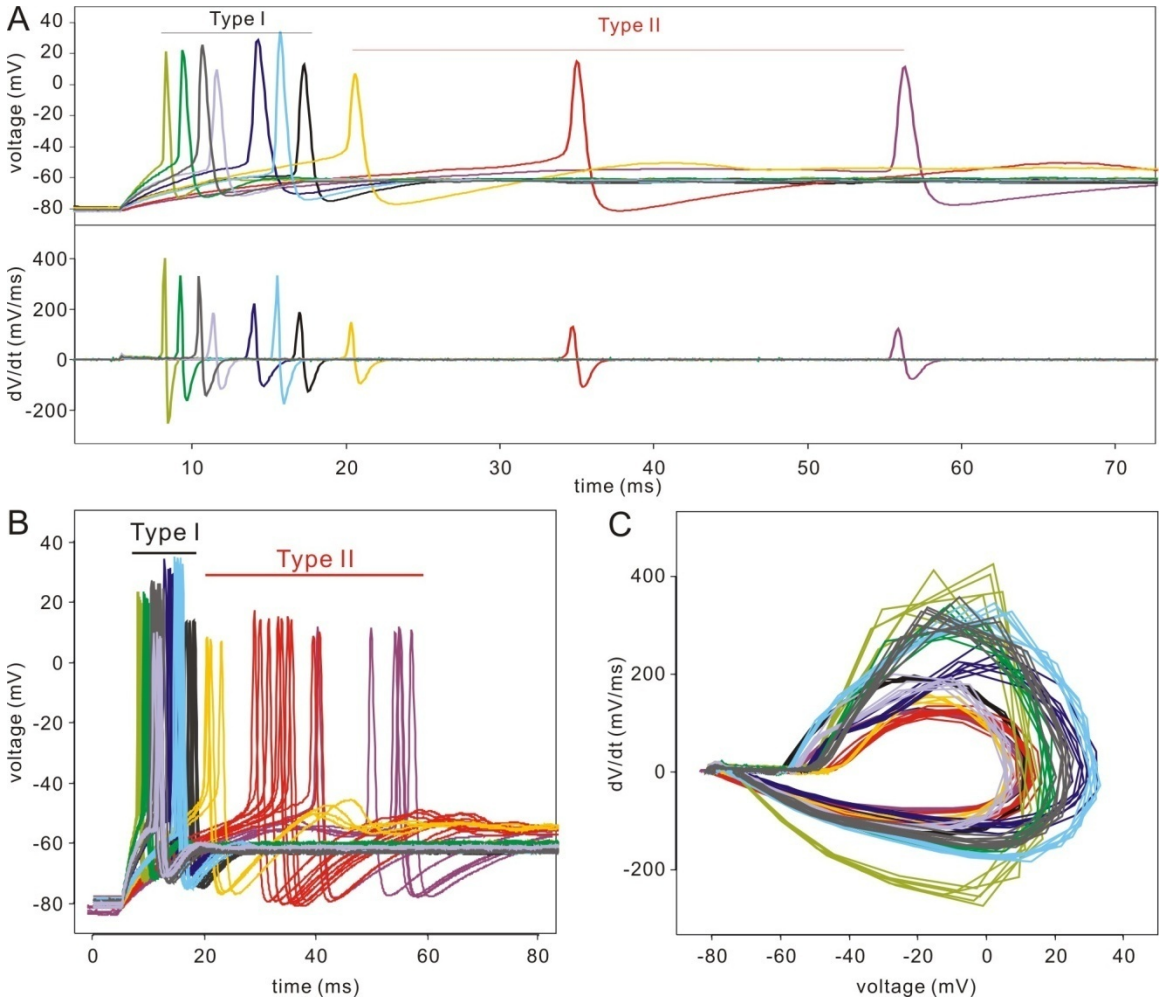

Figure 5.4: Distinct intrinsic firing features of type I and type II spiral ganglion neurons. A, Examplar traces of locally-evoked action potentials (upper panel) with corresponding rate of voltage change (dV/dt, lower panel) for nine different neurons. The innervations patterns of all recorded cells were validated with biocytin staining. **B**, Evoked-action potentials from the same neuron showed consistent profiles with some jitter. **C,** Phase plots of the action potentials in **B**. The same color codes apply to all panels. Two type II recordings (red and purple) and one type I recording (black) were collected with 1kHz low pass filter, while the rest recordings were filtered under 5kHz setting.

Synaptically-driven Events in Spiral Ganglion Neuron Somata

In addition to the characterization of intrinsic firing properties, the acute preparation also

provides opportunities to examine the neuronal responses in more physiological conditions. As the hair cell region remains intact in the acute preparation, it is possible that some hair cells demonstrate active transduction channels and remain synaptically connected. We explored the first possibility by utilizing FM1-43, a vital dye used as an indicator for hair bundle function because it permeates hair cells through mechanotransduction channels on the stereocilia (Meyers et al., 2003). When FM1-43 was applied to the bath of an acute OC-SGN preparation of Thy1-YFP mouse, stereocilia of some outer hair cells and inner hair cells were labeled by fluorescence (Fig. 5.5), suggesting that a subset hair cells remained mechanotransductive in the preparation.

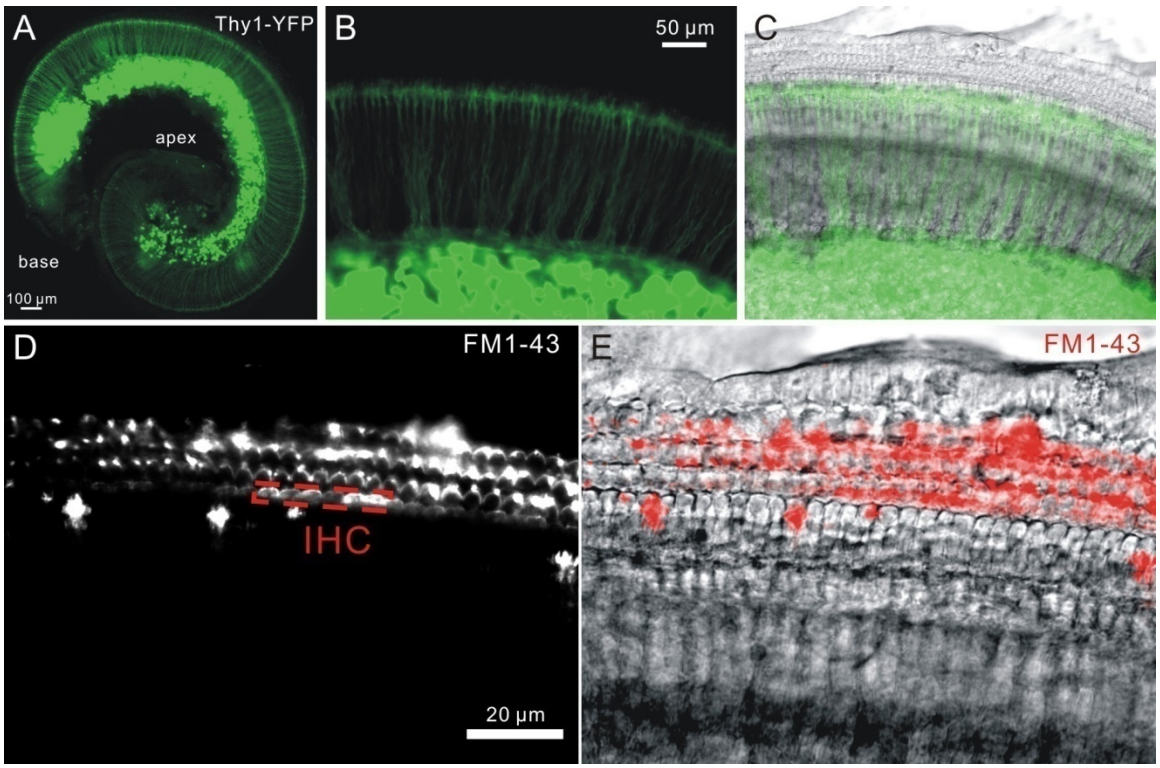

Figure 5.5: Hair cells may remain mechanotransductive in the acute OC-SGN preparation. A, Low magnification image of a Thy1-YFP cochlear whole-mount. Green

fluorescence in spiral ganglion neurons revealed the intact innervations. **B-C**, Fluorescent and merged bright field image (**C**) with high magnification of the same sample as in **A**. **D-E**, FM1-43 vital dye staining of the same preparation as in **A-C**. Three rows of outer hair cell sterocillia and one row of inner hair cell sterocillia could be observed in parts of the organ of Corti.

AMPA-receptor mediated excitatory postsynaptic currents (EPSCs) with unusually large amplitudes (Glowatzki and Fuchs, 2002) presumably evoke action potentials at proximal heminodes in type I spiral ganglion neurons (Hossain et al., 2005; Rutherford et al., 2012). To reach their central targets, these action potentials must first travel through the cell soma. Indeed, invading action potentials and putative excitatory post synaptic potentials (EPSPs) were observed in the somata of spiral ganglion neurons under current clamp mode. The invading action potentials inflected rapidly at voltage levels close to the holding potential, thus were distinctive from the action potentials generated by local injection of currents, in which an exponential rise phase preceded the inflection (Fig. 5.6B, black and dark gray traces). The putative EPSPs displayed characteristic exponential rise and decay (Fig. 5.6C, arrows). The occurrence frequency of invading spikes and EPSPs was not correlated with the holding potential, but their amplitude and profile may be shaped by the baseline membrane voltage. A fast afterdepolarization phase was observed immediately after the invading action potential under -80mV holding potential (Fig. 5.6C, upper panel), while the same neuron display increasing amplitude of afterhyperpolarization when the baseline potential was depolarized to -70mV and -60mV (Fig. 5.6C, middle and lower panels). The voltage-related features of after potentials may reflect the kinetics and reversal potential of local potassium conductances. Synaptic

potentials were larger at a more hyperpolarized baseline (Fig. 5.6C, arrows), consistent with the increase of driving force through the AMPA receptor with hyperpolarization. In contrast, the oscillation of membrane potential was more potent at -60mV, possibly due to the activation of voltage-dependent channels at the relatively depolarized potential (Fig. 5.6C, lower traces in each panel).

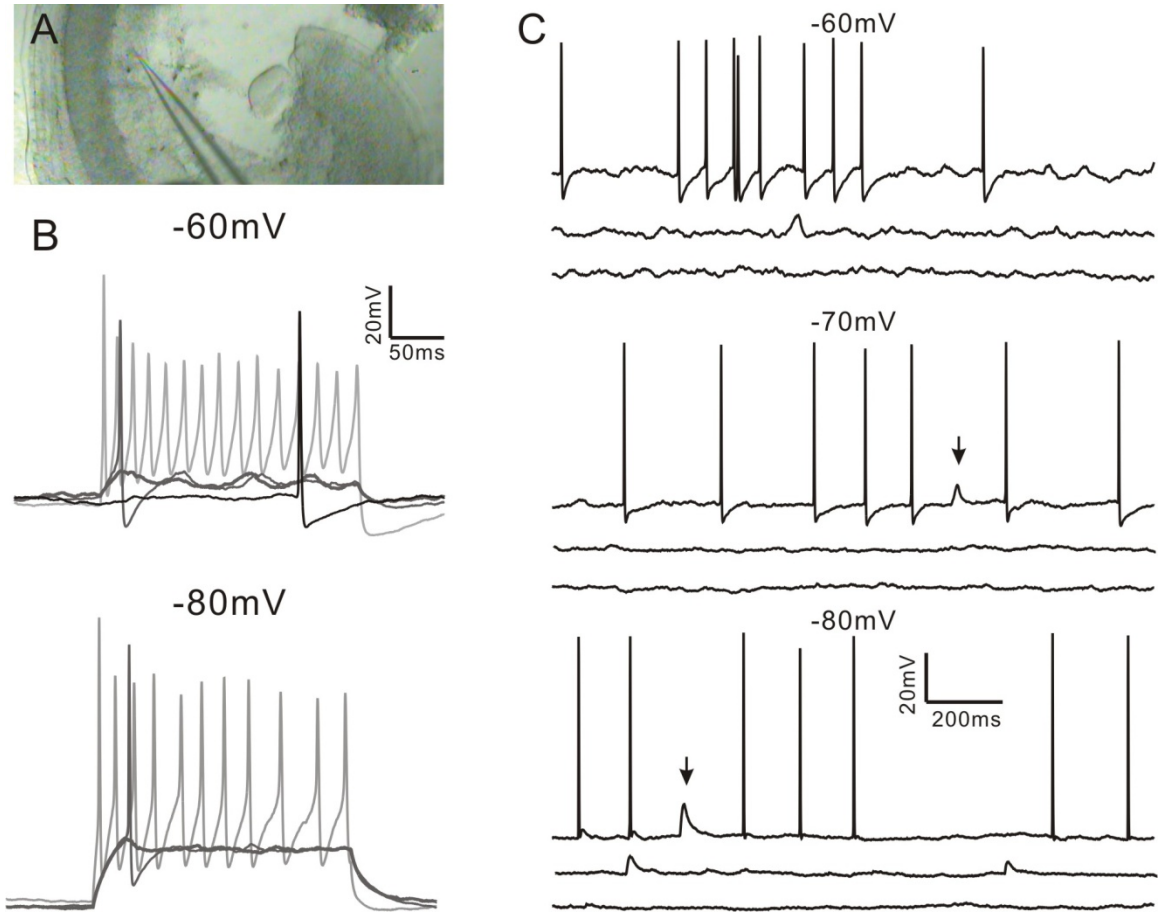

Figure 5.6: Invading action potentials in the somata of spiral ganglion neurons. **A**, Image of the recording electrode attached to a neuron in the mid-cochlear region. **B**, Intrinsic firing patterns of the neuron in **A**. Sub-threshold (thick dark gray line), supra-threshold (thin dark gray line) and AP max (light gray line) traces from -60mV and -80mV holding potentials were shown as overlay. Invading action potential was observed at -60mV without further depolarization (black trace). **C**, Recordings from different holding potentials without current injection from the same neuron as in **A-B**. Arrows, putative EPSP.

To further identify the putative synaptic activity, we examined the whole cell currents recorded from somata of spiral ganglion neurons in the acute OC-SGN preparation. Consistent with the presence of invading action potentials and putative EPSPs in the current clamp recordings, both action currents and putative post synaptic currents (PSCs) were observed under voltage clamp mode (Fig. 5.7D). The amplitude of putative EPSCs became consistently smaller with more depolarized holding potentials, indicating a depolarizing reversal potential of these currents. Bath application of the AMPA and kainate receptor blocker DNQX (6,7-dinitroquinoxaline-2,3-dione) abolished both action currents and putative PSCs (Fig. 5.5E), suggesting that the observed synaptic activity was mediated by glutamate receptors.

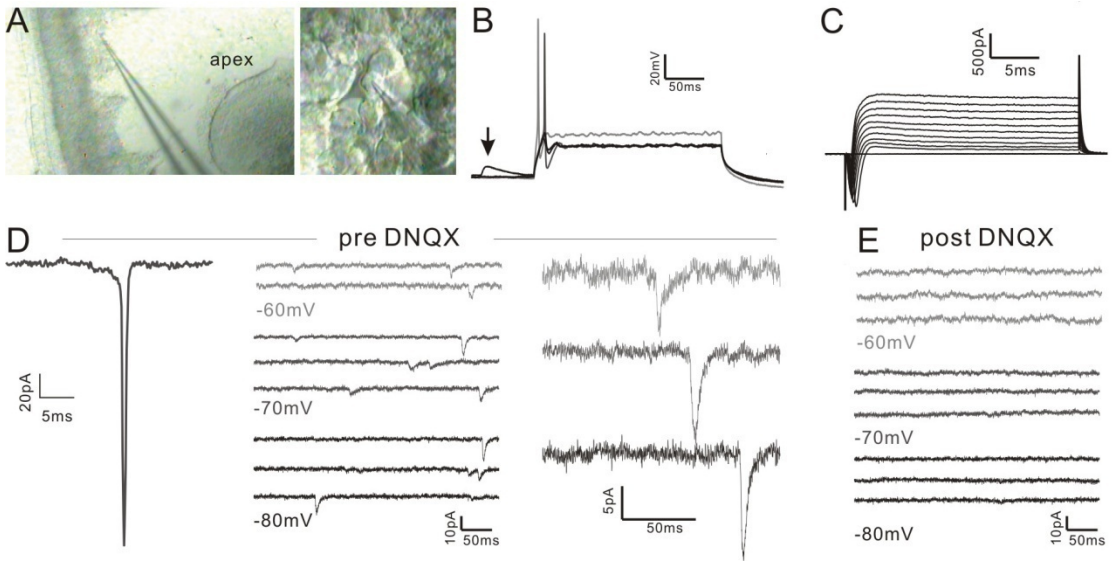

Figure 5.7: Putative synaptic currents were DNQX sensitive. A, Low (left) and high (right) magnification images of the recording pipette patched on a neuron in the basal turn of a P1 acute OC-SGN preparation. **B**, Current-clamp recordings from -80mV holding potential showed sub-threshold (black), supra-threshold (dark gray) and AP max (light gray) traces. An example of EPSP was observed on the baseline of one sub-threshold trace (arrow). **C**, Depolarization of -70mV~50mV square pulses from -80mV holding potential revealed inward and outward whole cell currents in voltage-clamp mode. **D**,

Examples of putative EPSCs and action currents recorded in voltage-clamp configuration under -80mV (black), -70mV (dark gray) and -60mV (light gray) holding potentials. Invading action currents were observed from -70mV holding potential. **E**, putative EPSCs were blocked by application of DNQX (final concentration ~10μM) in the bath.

The somata of spiral ganglion neurons exhibited invading action potentials and synaptic events in an episodic manner. The invading action potentials were unevenly distributed over the time course of the recording, often spaced by long intervals with limited to no activity. In an exemplar recording from a P6 animal, 14 successive current clamp traces with 400ms duration and 100ms inter-sweep-interval demonstrated that the action potentials and synaptic potentials were grouped into active periods (Fig. 5.8A). This observation is consistent with previous reports of extracellular recording on spiral ganglion neurons of pre-hearing rats and mice (Tritsch et al., 2010; Wong et al., 2013). The waveform profiles of the invading action potentials and synaptic potentials were highly diverse among recordings made from age-matched samples. Action potentials could precede or succeed complex EPSP waveforms, indicating temporal overlap of sub-threshold and supra-threshold synaptic events (Fig. 5.8A). While single action potentials were frequently observed, there were also instances of high frequency multi-spike bursts (Fig. 5.8B). A voltage clamp recording from a P0 animal showed combined postsynaptic and action currents, which were entirely blocked by bath application of DNQX (Fig. 5.8C).

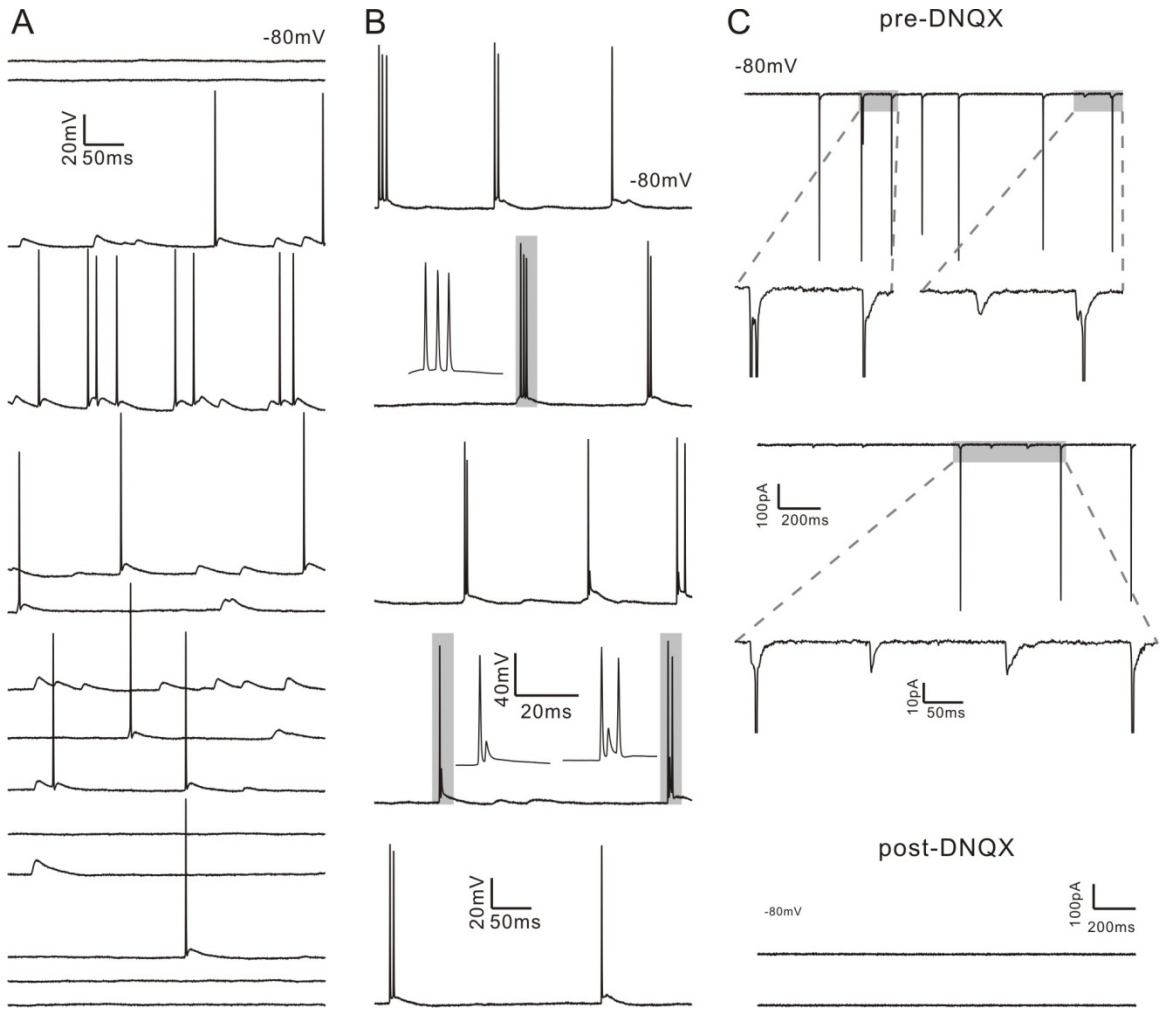

Figure 5.8: Patterns of synaptically-driven events in spiral ganglion neuron somata. **A**, Successive current clamp traces from a P6 spiral ganglion neuron somatic recording. **B**, An example P6 recording showing the burst waveform profiles. Portions of the traces in gray boxes were shown in high resolution in insets. **C**, Voltage clamp traces from a P0 spiral ganglion neuron. Complex waveforms of synaptic and action currents were blocked by DNQX (bath applied, final concentration ~10μM).

Spike generation at the postsynaptic membrane of type I neurons was found to have a high success rate and small temporal jitter (Rutherford et al., 2012). In contrast, as described earlier in this chapter, the intrinsic membrane properties of spiral ganglion neurons were highly diverse. As action potentials travel through the spiral ganglion

neurons into the central nervous system, we hypothesized that the timing and waveform of the action potentials is shaped by local membrane properties at spiral ganglion neuron somata, thus, adding another dimension to the information encoded by the auditory nerve. To address this question, we compared the detailed profiles of locally-evoked action potentials to that of invading action potentials and EPSPs in spiral ganglion neuron somata.

Eight recordings from P6-7 neurons were included in this analysis. Locally-evoked action potentials of each neuron showed differences in spike latency, amplitude, threshold, onset kinetics and rate of voltage change in both the depolarization and the repolarization phases (Figure 5.9A-B). Although not unexpectedly intra-recording jitter was observed, locally-evoked action potentials recorded from each neuron were grouped and displayed profiles distinctive from each other (Fig. 5.9C). The latency of these locally-evoked action potentials all fall in the interval between 5 and 25 ms, consistent with the latency range of the validated type I neurons (Fig. 5.4A-B). Invading action potentials recorded from the same cells showed more rapid onset and larger net currents than the locally-evoked action potentials. While in all invading action potential recordings, the membrane potential increased abruptly at the onset of the spike, three out of the eight recordings exhibited an additional component, during which the rate of voltage change decreased after an initial rapid onset and then increase again (Fig. 5.9E-F). This phase resembled the EPSP leading phase in recordings obtained from type I peripheral terminal (Rutherford et al., 2012), and will be discussed in more details later.

Interestingly, when the general profiles of locally-evoked action potentials were compared to their invading counterparts, similar inter-recording difference could be recognized. Moreover, this repertoire of action potential kinetics among different cells was not reiterated in the comparison of EPSP kinetics, suggesting that the locally-evoked and the invading action potentials may be shaped by the same set of local ion channels, the properties of which were separated from the passive electrical properties of the neuron and the receptor mediated synaptic potentials.

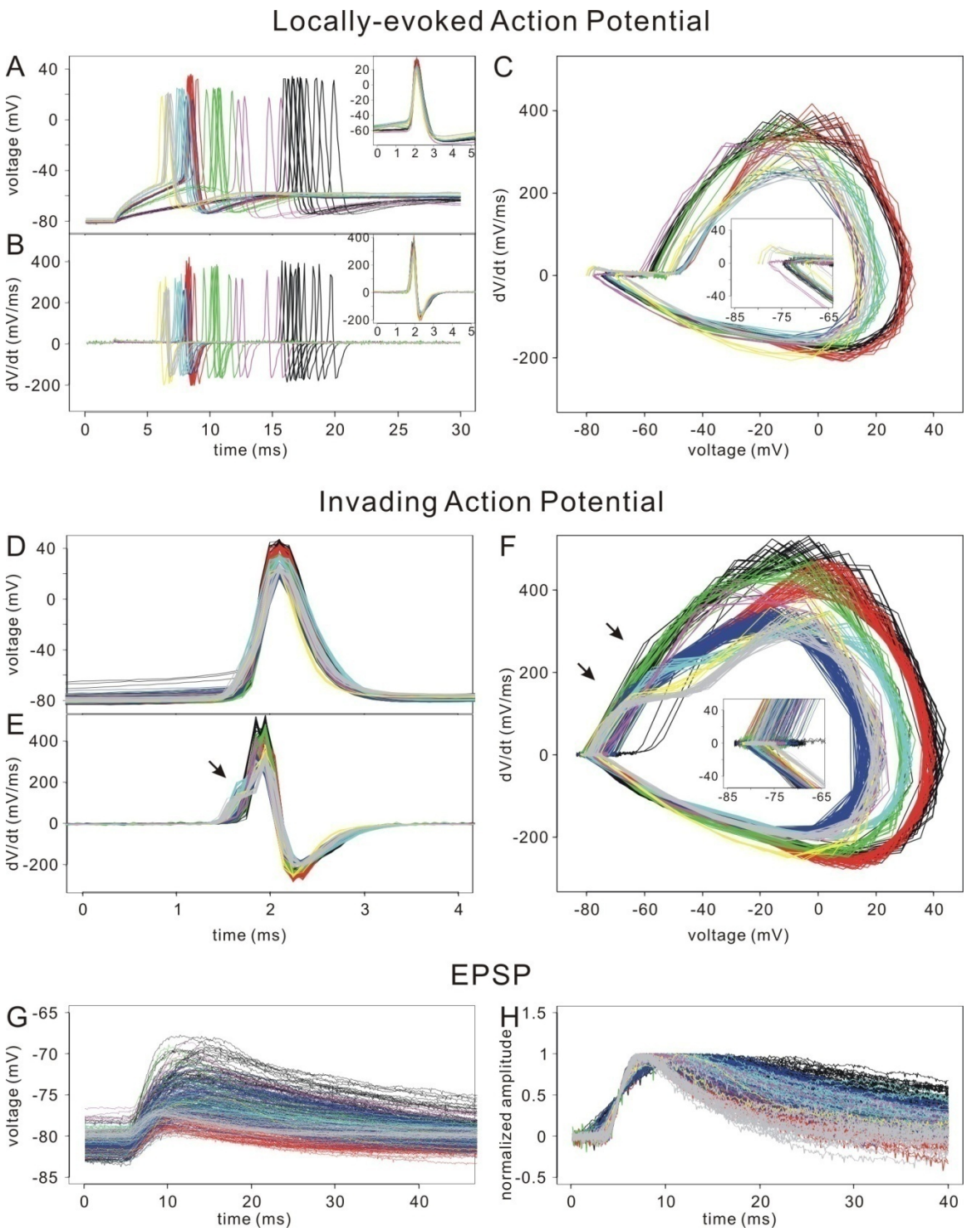

Figure 5.9: Comparison of local and invading potentials in the spiral ganglion somata. Locally-evoked action potentials, invading action potentials and EPSPs were recorded from seven P6-7 neuronal somata. Recordings made from each cell were color-coded accordingly. **A-B,** Action potential and rate of voltage change at threshold level were plotted against time from the onset of current injection. **A-B insets**, The same

traces with the peaks of action potential aligned. **C**, Phase plots of the same recordings as in **A-B**. **C Inset**, the initial part of the phase plots were shown in a different scale. **D-E**, Invading action potentials and their corresponding rate of voltage change, with the peaks of action potentials aligned in time. Note additional components in the yellow and the cyan traces (arrow). **F**, Phase plots of the invading action potentials in **D-E**. The initial phase in the yellow and the cyan traces could also be observed (arrows). **G**, Overlay of EPSPs recorded from the same cells as in **A-F**. **H**, EPSPs normalized by amplitude and aligned in time according to half-height.

Summary and discussion

In this chapter, we systematically investigated how intrinsic membrane properties shape electrogenic transmission through the soma of spiral ganglion neurons. Because this is an obligatory pathway through these bipolar neurons, it is imperative to understand their role in peripheral auditory encoding. The acute OC-SGN preparation with its intact synaptic connections to hair cell receptors offered the opportunity to compare invading action potentials generated at the periphery to those evoked from local constant current injection. We first validated that the diverse intrinsic firing features of type I spiral ganglion neurons reported in cultured neurons were also present acutely. We then defined the distinct membrane properties characteristic of type II neurons, which were consistent with a previous report from the laboratory (Reid et al., 2004). Finally, we characterized the organ of Corti generated EPSPs and invading action potentials (never observed in spiral ganglion neuron cultures) and compared them to locally-evoked action potentials at neuronal cell bodies. The observation that invading action potentials also varied among different neurons with features similar to locally-evoked action potentials supports the

role of spiral ganglion neuron cell somata actively contributing to auditory information encoding.

While these conclusions could have far reaching functional implication, we must consider that most of the recordings reported herein were made from preparations of P6-7 pre-hearing animals. Therefore, it is possible that the pattern we observed would be subjected to developmental refinement. In adult mice, a high density of sodium channels were observed at nodes in perisomatic region and heminodes close to the organ of Corti (Hossain et al., 2005), but the development of nodal structure and myelination patterns of auditory fiber in early postnatal animals still remains unclear (Schwartz et al., 1983; Toesca, 1996). Invading action potentials at neuron somata were observed as early as P0 in the acute preparation, suggesting that the nodes may have already started to form at this stage.

It has been well-accepted that in post-hearing animals, action potentials were generated at the heminode in the radial segment of the auditory fiber in type I spiral ganglion neurons (Figure 5.10). The same conclusion may hold for younger animals, since we observed that EPSP amplitude was much smaller than the voltage required to trigger a local action potential, suggesting that all EPSP waveforms observed at neuron somata were passively propagated sub-threshold events. When compared to the previous reports of spike features at postsynaptic boutons, the waveforms of invading action potentials at somata may provide further information about the spike initiation in spiral ganglion neurons. As described in the previous section, some somatic recordings showed

rapid onset from the baseline, as one would predict for the relayed action potentials that travel through full nodes to reach the cell soma. In some recordings, on the other hand, a 'notch' was observed in the upshot portion of the action potential phase plot, which was similar to the EPSP leading phase in the phase plots of recordings obtained from the terminal (Figure 5.10). This pattern may indicate that for some spiral ganglion neurons, the action potentials initiated at the heminode were regenerated only after they reached the cell soma. Therefore, differences in waveforms of invading action potentials indicated that the nodal machinery and membrane properties may undergo active tuning during the pre-hearing stage.

In summary, much diversity in the invading action potential profiles was observed in somatic recordings obtained from early postnatal murine spiral ganglion neurons, possibly due to individual difference in the developmental process. Even at this stage, correlation between the waveforms of invading and locally-evoked action potentials was already established. This observation, taken together with the diversity in intrinsic firing features of spiral ganglion neuron somata maintained from early postnatal to post hearing stages (Crozier and Davis, 2014), strongly suggests that auditory information is shaped by the diverse membrane properties of spiral ganglion neurons.

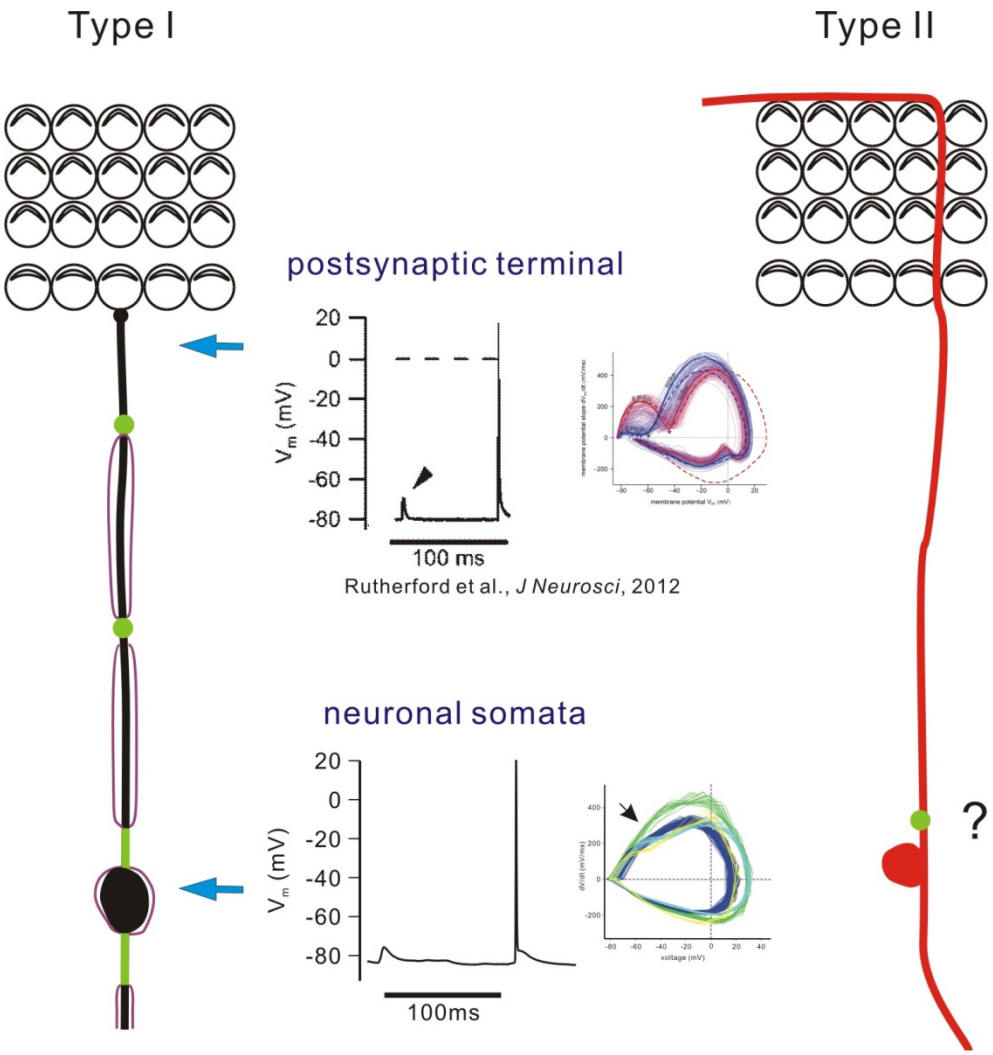

Figure 5.10: A summary of observed activity at type I and type II spiral ganglion somata of P6-7 acute preparation. Both EPSP and invading action potentials were observed in the somata, while the EPSP were significantly slower than that observed at the terminal. In the phase plots, some of the somatic recordings showed an initial phase (arrow) similar to the EPSP waveform in the terminal recordings. Invading action potentials were not observed in the type II neurons.

Chapter 6

Discussion

More than fifty years ago, John von Neumann, arguably one of the most important figures in the development of modern computers and to whom the current 'digital age' owes its existence, composed a lecture note titled 'The Computer and the Brain'. The lecture was never delivered due to the author's deteriorating health, and was published posthumously. In this last work of his, von Neumann provided dazzling insights into the similarity and dissimilarity between the then emerging digital computer and the human brain. He recognized the brain as a mixed system, in the sense that its signal transmission process would alter repetitively between digital and analog modes. Although von Neumann considered the 'character of nervous system' as 'primarily digital', he also noticed that the mixed manner of signal transmission would allow 'general electrical potentials' to play a role alongside the 'digital' action potentials, therefore, 'a nerve cell is more than a single basic active organ' (von Neumann, 1958).

In the past decades, two approaches in the fields of neuroscience have greatly advanced our understanding of how the nervous system carries out its functions. On one hand, system neuroscience and the growing field of circuit neuroscience have unveiled much of the architecture of the nervous system on different levels of organization. On the other hand, thanks to the efforts in molecular and cellular neurobiology that focused on the building block of nervous system, we now know much more about the morphological

and physiological properties of a single neuron than von Neumann did fifty years ago. In the light of current neurophysiology, it is no longer a speculation that a single neuron is much more than a single unit that carries out basic computations (Koch and Segev, 2000). In fact, it is proposed that information content of neural signals may be enriched by the 'analog' subthreshold activity that propagates passively from the dendrites into the somata and axon, where ion channel activity and vesicle release processes could be modulated by depolarization (Clark and Häusser, 2006; Alle and Geiger, 2008; Debanne et al., 2013).

Given its unique innervation pattern and morphological specialization, spiral ganglion in the mammalian cochlea could serve as a model system to examine the 'mixture' of digital and analog signaling process on the neuronal level. As described in the earlier chapters, type I neurons that comprise 95% of the cell population in spiral ganglion form synapses with the inner hair cells in a one-to-one manner. In the first step of auditory signal transmission, the inner hair cells transduce the mechanical energy of sound wave into neurotransmitter release at the powerful ribbon synapse (Glowatzki et al., 2008). Due to the large amplitude of synaptic currents and the proximity of the heminode to the synapses, action potentials are initiated in the radial fibers close to foramina nervosa where the unmyelinated segments of type I processes enter the organ of Corti. Therefore, the neural signal is 'digitized' almost immediately after synaptic transmission and would travel along the myelinated processes of the bipolar type I neurons in the form of action potentials, going pass the somata on their way to the cochlear nucleus. In

perspective of action potential propagation, the majority part of a type I spiral ganglion neuron central to the heminode would resemble the axonal compartment of a hippocampal neuron, where a 'hybrid code' of analog and digital signaling was observed (Alle and Geiger, 2006). In contrast to the hippocampal axons, however, spiral ganglion neurons somata are conveniently accessible to electrophysiological investigations.

In this study, we started out with a characterization of the diversity of spiral ganglion subpopulations in isolated cultures. Our results revealed that, in addition to the known morphological dichotomy between type I and type II neurons and the tonotopic gradient of membrane properties and synaptic protein distribution from the apex to the base, spiral ganglion neurons also displayed local heterogeneity that could be characterized by the distribution patterns of the calcium binding proteins calretinin and calbindin (Chapter 3). However, it remains unclear at this stage how this new dimension of complexity could be related to the intrinsic features of the auditory afferents. When we examine the membrane responses in the somata of spiral ganglion neurons utilizing the acute OC-SGN preparation (Chapter 5), both actively regenerated action potentials and passively propagated EPSPs were observed, and the invading action potentials shared kinetic features with locally-evoked action potentials in the same neuron.

It is evident from our results that, the type I spiral ganglion neuron somata, like the mossy fiber axons in the hippocampus, receive both digital and analog signal inputs. Future experiments are required to further investigate whether the EPSPs that arrive in

the somata change the presynaptic properties or trigger a long term modulation of the general status of the neuron. Fortunately the accessibility of spiral ganglion neuron somata would greatly facilitate this investigation. Our results also suggested that, even the 'digital' information, i.e., the invading action potentials, could be filtered, shaped or fine-tuned by local conductances in the somata. Based on the known heterogeneity of spiral ganglion neuron membrane properties, it is conceivable that the spiral ganglion uses a population code to represent the rich details of auditory information. In this view, within each frequency region along the apex-base tonotopic gradient, neurons receiving the same hair cell inputs may convey different neural signals due to their diverse local conductances. This population code would be superimposed on the tonotopic gradient of ion channel distribution and firing features, which indicates a general trend of higher levels of ion channel density and faster kinetics in the basal compared to the apex (Figure 6.1). Moreover, given the repertoire of ion channel types present in the spiral ganglion, firing patterns of spiral ganglion neurons within the same local group can be further diversified. Characterization of spiral ganglion neuron membrane properties, when paralleled by investigations into the propagation of synaptically-driven action potentials, may shed some light on both the nature of mixed analog/digital signaling in general, and the peripheral encoding of auditory information in particular.

The heterogeneous nature of the spiral ganglion also has potential clinical implications. As we have shown in chapter 4 of this dissertation, progresses have already been made towards using cell replacement to treat sensorineural hearing loss.

Neuronal-like phenotype can be induced in cochlear epithelial cells with overexpression of neurogenic transcription factors Ascl1 and NeuroD1, but the membrane properties of the induced neuronal-like cells were still immature compared to endogenous spiral ganglion neurons. Other cochlea specific downstream factors such as Gata3 and Tbx1 may be required for a more refined phenotype (Appler and Goodrich, 2011). As the heterogeneity among membrane properties of spiral ganglion neurons may be essential for their functions, cell replacement approaches will have to take it into account. To remedy the loss of spiral ganglion neurons, membrane properties of induced cell types will have to span the same broad range as observed in the neurons. Therefore, further characterization of how physiological heterogeneity is established during the development of spiral ganglion will be a crucial step towards replacing it in damaged cochlea.

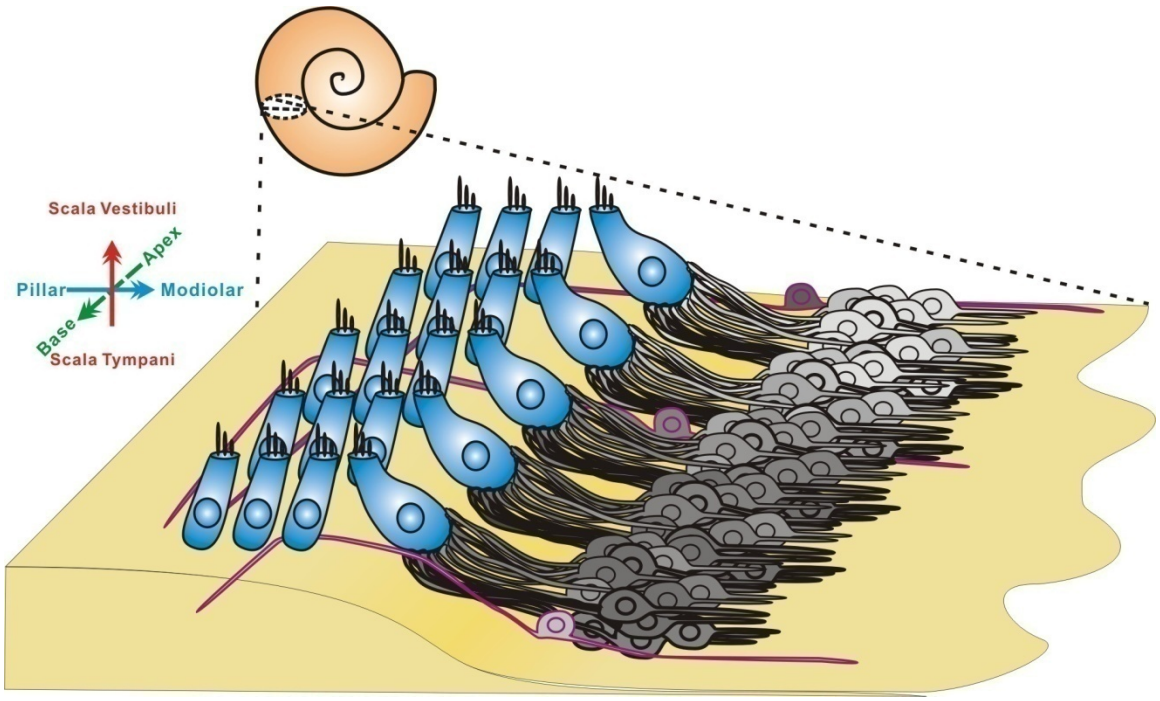

Figure 6.1: Local heterogeneity within the spiral ganglion may form a population code. Schematic of the spiral ganglion and the organ of Corti showing local heterogeneity superimposed on a tonotopic gradient. Gray scales represent levels of ion channel density. Type I spiral ganglion neurons receiving inputs from the same inner hair cell receptor may convey different information due to their different ion channel compositions.

Appendix

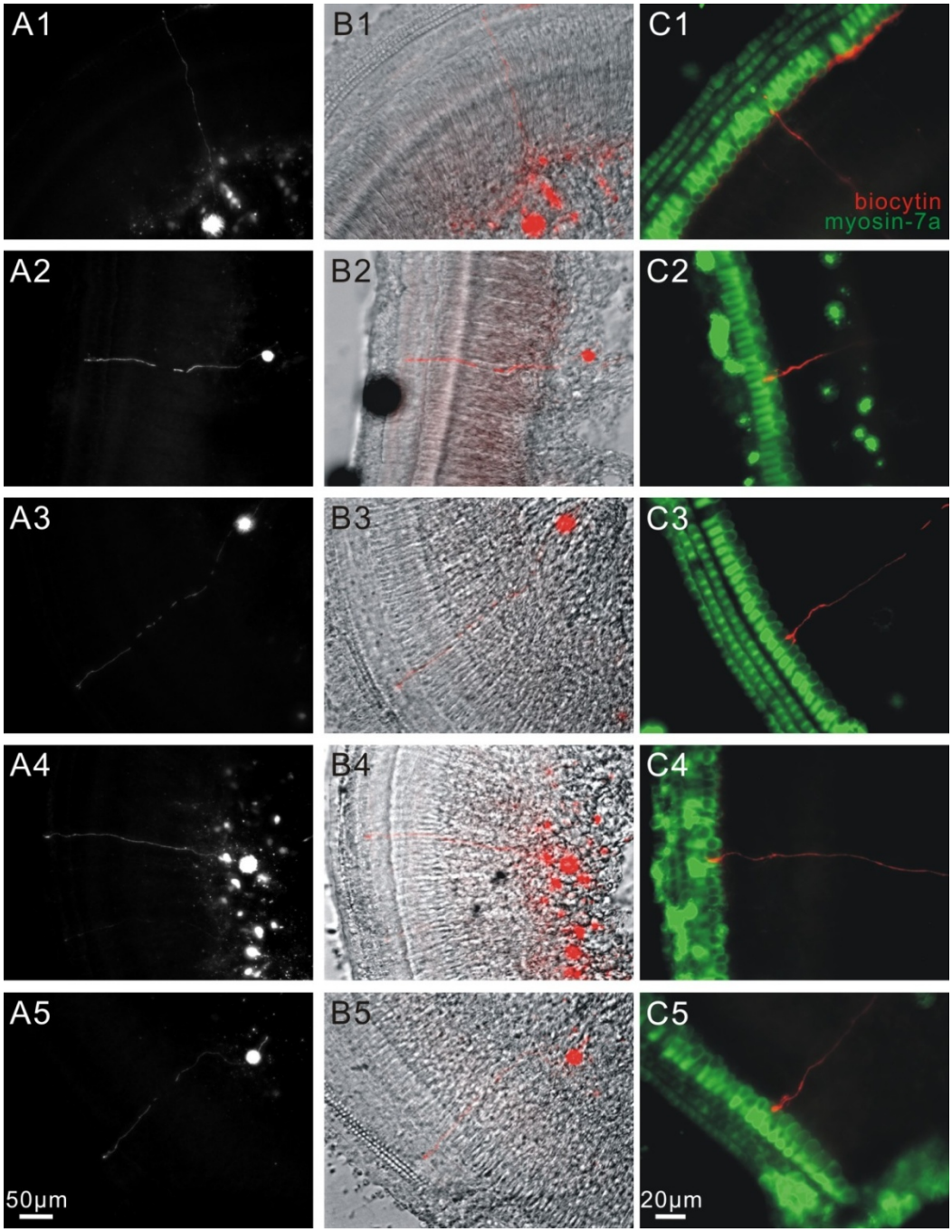

Figure A.1: Innervation patterns of type I afferent terminal in the cochlea. Images of biocytin filling (**A**), bright field (**B**) and co-labeling of biocytin and the hair cell marker Myosin-7a (**C**) of five different neurons in the acute preparation of P6-7 OC-SGN. Some process ending showed multiple branches (1-3).

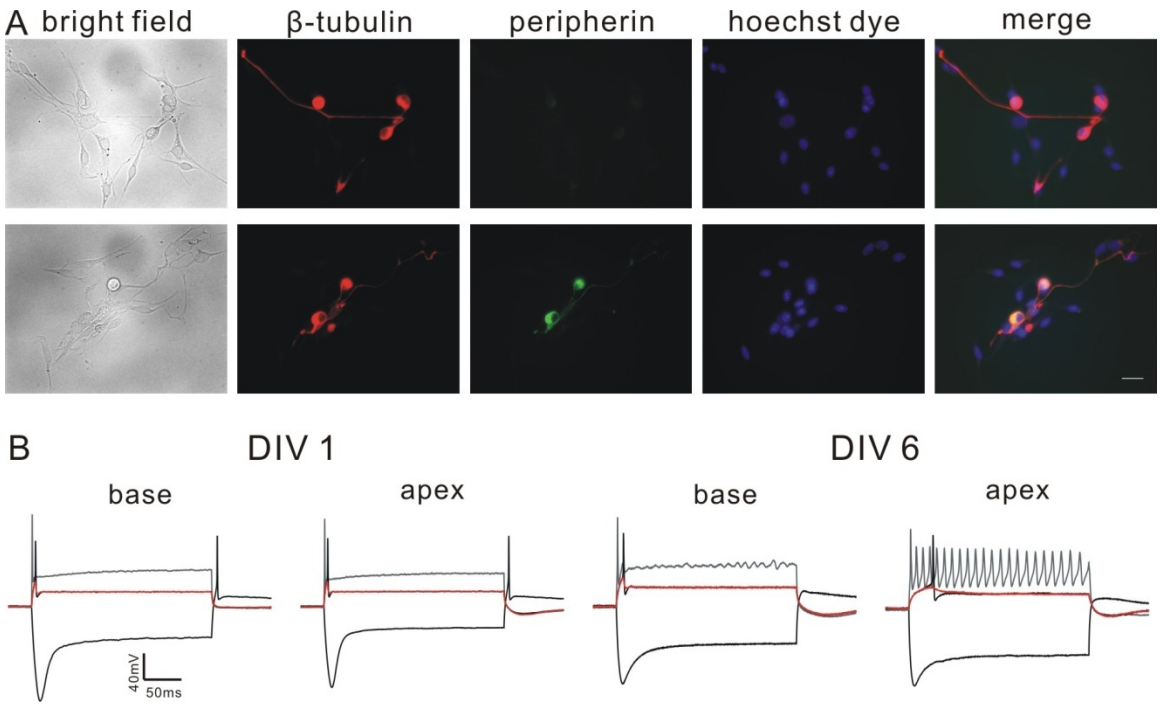

Figure A.2: Dissociated culture of spiral ganglion neurons. A, Dissociated cultures of P6 mouse spiral ganglion neurons were fixed using methanol on DIV1 and stained with antibodies against the neuronal marker β-III-tubulin, type II spiral ganglion neuron marker peripherin. Presence of the non-neuronal cell types in the same dish can be observed by bright field view and the Hoechst dye nuclei staining. Both type I (upper panels) and type II (lower panels) are observed. Scale bar, 20μm, applied to all panels. **B**, Recordings were made on different days *in vitro* from dissociated cultures of P6-P7 spiral ganglion neurons. Tonotopic difference of firing accommodation more resemble the previous results from neuronal explant cultures were observed on DIV6. Sub-threshold (red), supra-threshold, AP_{max} (gray) and hyperpolarization sag traces were shown for each recording from -80mV holding potential. Scale bars applied to all panels.

Bibliography

Adamson CL, Reid M a, Davis RL (2002a) Opposite actions of brain-derived neurotrophic factor and neurotrophin-3 on firing features and ion channel composition of murine spiral ganglion neurons. J Neurosci 22:1385–1396.

Adamson CL, Reid MA, Mo Z-L, Bowne-English J, Davis RL (2002b) Firing features and potassium channel content of murine spiral ganglion neurons vary with cochlear location. J Comp Neurol 447:331–350.

Alle H, Geiger JRP (2006) Combined analog and action potential coding in hippocampal mossy fibers. Science (80-) 311:1290–1293.

Alle H, Geiger JRP (2008) Analog signalling in mammalian cortical axons. Curr Opin Neurobiol 18:314–320.

Angelo K, Rancz EA, Pimentel D, Hundahl C, Hannibal J, Fleischmann A, Pichler B, Margrie TW (2012) A biophysical signature of network affiliation and sensory processing in mitral cells. Nature 488:375–378.

Appler JM, Goodrich L V (2011) Connecting the ear to the brain: Molecular mechanisms of auditory circuit assembly. Prog Neurobiol 93:488–508.

Berglund AM, Ryugo DK (1987) Hair cell innervation by spiral ganglion neurons in the mouse. J Comp Neurol 255:560–570.

Bermingham-McDonogh O, Reh TA (2011) Regulated reprogramming in the regeneration of sensory receptor cells. Neuron 71:389–405.

Bizley JK, Walker KMM (2010) Sensitivity and selectivity of neurons in auditory cortex to the pitch, timbre, and location of sounds. Neuroscientist 16:453–469.

Brown MC (1994) Antidromic responses of single units from the spiral ganglion. J Neurophysiol 71:1835–1847.

Burgess BJ, Adams JC, Nadol JB (1997) Morphologic evidence for innervation of Deiters' and Hensen's cells in the guinea pig. Hear Res 108:74–82.

Chen C (1997) Hyperpolarization-activated current (Ih) in primary auditory neurons. Hear Res 110:179–190.

Cheung WT, Richards DE, Rogers JH (1993) Calcium binding by chick calretinin and rat calbindin D28k synthesised in bacteria. Eur J Biochem 215:401–410.

Clark B, Häusser M (2006) Neural coding: hybrid analog and digital signalling in axons. Curr Biol 16:R585–R588.

Crozier RA, Davis RL (2014) Unmasking of Spiral Ganglion Neuron Firing Dynamics by Membrane Potential and Neurotrophin-3. J Neurosci 34:9688–9702.

D'Angelo E, De Filippi G, Rossi P, Taglietti V (1998) Ionic mechanism of electroresponsiveness in cerebellar granule cells implicates the action of a persistent sodium current. J Neurophysiol 80:493–503.

Davis RL (2003) Gradients of Neurotrophins, Ion Channels, and Tuning in the Cochlea. Neuroscientist 9:311–316.

Davis RL, Liu Q (2011) Complex primary afferents: What the distribution of electrophysiologically-relevant phenotypes within the spiral ganglion tells us about peripheral neural coding. Hear Res 276:34–43.

Debanne D, Bialowas A, Rama S (2013) What are the mechanisms for analogue and digital signalling in the brain? Nat Rev Neurosci 14:63–69.

Dechesne CJ, Rabejac D, Desmadryl G (1994) Development of calretinin immunoreactivity in the mouse inner ear. J Comp Neurol 346:517–529.

Dechesne CJ, Thomasset M (1988) Calbindin (CaBP 28kDa) appearance and distribution during development of the mouse inner ear. J Comp Neurol 40:233–242.

DeFelipe J (1997) Types of neurons, synaptic connections and chemical characteristics of cells immunoreactive for calbindin-D28K, parvalbumin and calretininin the neocortex. J Chem Neuroanat 14:1–19.

DeFelipe J, González-Albo MC, Del Río MR, Elston GN (1999) Distribution and patterns of connectivity of interneurons containing calbindin, calretinin, and parvalbumin in visual areas of the occipital and temporal lobes of the macaque monkey. J Comp Neurol 412:515–526.

Dhawale AK, Hagiwara A, Bhalla US, Murthy VN, Albeanu DF (2010) Non-redundant odor coding by sister mitral cells revealed by light addressable glomeruli in the mouse. Nat Neurosci 13:1404–1412.

Dumas TC, Powers EC, Tarapore PE, Sapolsky RM (2004) Overexpression of calbindin D(28k) in dentate gyrus granule cells alters mossy fiber presynaptic function and impairs hippocampal-dependent memory. Hippocampus 14:701–709.

Faas GC, Mody I (2012) Measuring the kinetics of calcium binding proteins with flash photolysis. Biochim Biophys Acta 1820:1195–1204.

Fechner FP, Nadol JB JR, Burgess BJ, Brown MC (2001) Innervation of supporting cells in the apical turns of the guinea pig cochlea is from type II afferent fibers. J Comp Neurol 429:289–298.

Flores-Otero J, Davis RL (2011) Synaptic proteins are tonotopically graded in postnatal and adult type I and type II spiral ganglion neurons. J Comp Neurol 519:1455–1475.

Flores-Otero J, Xue HZ, Davis RL (2007) Reciprocal regulation of presynaptic and postsynaptic proteins in bipolar spiral ganglion neurons by neurotrophins. J Neurosci 27:14023–14034.

Froud KE, Wong ACY, Cederholm JME, Klugmann M, Sandow SL, Julien J-P, Ryan AF, Housley GD (2015) Type II spiral ganglion afferent neurons drive medial olivocochlear reflex suppression of the cochlear amplifier. Nat Commun 6:7115.

Fryatt AG, Vial C, Mulheran M, Gunthorpe MJ, Grubb BD (2009) Voltage-gated sodium channel expression in rat spiral ganglion neurons. Mol Cell Neurosci 42:399–407.

Gall D, Roussel C, Susa I, D'Angelo E, Rossi P, Bearzatto B, Galas MC, Blum D, Schurmans S, Schiffmann SN (2003) Altered neuronal excitability in cerebellar granule cells of mice lacking calretinin. J Neurosci 23:9320–9327.

Gardner EP, Martin JH (2000) Coding of sensory information. In: Principles of neural science, 4th ed. (Kandel ER, Schwartz JH, Jessell TM, eds). New York: McGraw-Hill.

Glowatzki E, Fuchs PA (2002) Transmitter release at the hair cell ribbon synapse. Nat Neurosci 5:147–154.

Glowatzki E, Grant L, Fuchs P (2008) Hair cell afferent synapses. Curr Opin Neurobiol 18:389–395.

Gollisch T, Meister M (2010) Eye smarter than scientists believed: neural computations in circuits of the retina. Neuron 65:150–164.

Hafidi A (1998) Peripherin-like immunoreactivity in type II spiral ganglion cell body and projections. Brain Res 805:181–190.

Haverkamp S, Wässle H (2000) Immunocytochemical Analysis of the Mouse Retina. J Comp Neurol 424:1–23.

Hiel H, Navaratnam DS, Oberholtzer JC, Fuchs P a. (2002) Topological and Developmental Gradients of Calbindin Expression in the Chick's Inner Ear. J Assoc Res Otolaryngol 3:1–15.

Hossain WA, Antic SD, Yang Y, Rasband MN, Morest DK (2005) Where is the spike generator of the cochlear nerve? Voltage-gated sodium channels in the mouse cochlea. J Neurosci 25:6857–6868.

Huang L-C, Thorne PR, Housley GD, Montgomery JM (2007) Spatiotemporal definition of neurite outgrowth, refinement and retraction in the developing mouse cochlea. Development 134:2925–2933.

Inoue T, Matsubara A, Maruya S, Yamamoto Y, Namba A, Sasaki A, Shinkawa H (2006) Localization of dopamine receptor subtypes in the rat spiral ganglion. Neurosci Lett 399:226–229.

Järlebark LE, Housley GD, Thorne PR (2000) Immunohistochemical localization of adenosine 5'-triphosphate-gated ion channel P2X(2) receptor subunits in adult and developing rat cochlea. J Comp Neurol 421:289–301.

Jones JM, Montcouquiol M, Dabdoub A, Woods C, Kelley MW (2006) Inhibitors of differentiation and DNA binding (Ids) regulate Math1 and hair cell formation during the development of the organ of Corti. J Neurosci 26:550–558.

Kandler K, Clause A, Noh J (2009) Tonotopic reorganization of developing auditory brainstem circuits. Nat Neurosci 12:711–717.

Keithley EM, Schreiber RC (1987) Frequency map of the spiral ganglion in the cat. J Acoust Soc Am 81:1036–1042.

Kelley MW (2006) Regulation of cell fate in the sensory epithelia of the inner ear. Nat Rev Neurosci 7:837–849.

Kevetter G (2002) Molecular probes of the vestibular nerve II. Characterization of neurons in Scarpa's ganglion to determine separate populations within the nerve. Brain Res 928:18–29.

Khalifa SAM, Friberg U, Illing RB, Rask-Andersen H (2003) Synaptophysin immunohistochemistry in the human cochlea. Hear Res 185:35–42.

Khan KM, Drescher MJ, Hatfield JS, Khan A-M, Drescher DG (2002) Muscarinic receptor subtypes are differentially distributed in the rat cochlea. Neuroscience 111:291–302.

Kiang NYS (1965) Discharge patterns of single fibers in the cat's auditory nerve. Cambridge: MIT press.

Kim WY, Fritzsch B, Serls A, Bakel LA, Huang EJ, Reichardt LF, Barth DS, Lee JE (2001) NeuroD-null mice are deaf due to a severe loss of the inner ear sensory neurons during development. Development 128:417–426.

Klapstein GJ, Vietla S, Lieberman DN, Gray P a, Airaksinen MS, Thoenen H, Meyer M, Mody I (1998) Calbindin-D28k fails to protect hippocampal neurons against ischemia in spite of its cytoplasmic calcium buffering properties: evidence from calbindin-D28k knockout mice. Neuroscience 85:361–373.

Koch C, Segev I (2000) The role of single neurons in information processing. Nat Neurosci 3:1171–1177.

Leake PA, Snyder RL, Merzenich MM (1992) Topographic organization of the cochlear spiral ganglion demonstrated by restricted lesions of the anteroventral cochlear nucleus. J Comp Neurol 320:468–478.

Leake PA, Synder RL (1989) Topographic organization of the central projections of the spiral ganglion in cats. J Comp Neurol 281:612–629.

Leonard RB, Kevetter GA (2002) Molecular probes of the vestibular nerve. I. Peripheral termination patterns of calretinin, calbindin and peripherin containing fibers. Brain Res 928:8–17.

Li GQ, Eatock RA (2013) A constitutive null mutation for calretinin has no effect on excitability of vestibular ganglion neurons. In: Abstracts of the 36th Annual Midwinter meeting of the Association of Research for Otolaryngology, pp 117.

Liberman MC (1978) Auditory-nerve response from cats raised in a low-noise chamber. J Acoust Soc Am 63:442–455.

Liberman MC (1982) Single-neuron labeling in the cat auditory nerve. Science (80-) 216:1239–1240.

Liberman MC (1991) Central projections of auditory-nerve fibers of differing spontaneous rate. I. Anteroventral cochlear nucleus. J Comp Neurol 313:240–258.

Liu Q, Davis RL (2007) Regional specification of threshold sensitivity and response time in CBA/CaJ mouse spiral ganglion neurons. J Neurophysiol 98:2215–2222.

Liu Q, Lee E, Davis RL (2013) Heterogeneous intrinsic excitability of murine spiral ganglion neurons is determined by Kv1 and HCN channels.

Liu Q, Lee E, Davis RL (2014) Heterogeneous intrinsic excitability of murine spiral ganglion neurons is determined by Kv1 and HCN channels. Neuroscience 257:96–110.

Liu Q, Manis P, Davis RL (2012) Heterogeneous distribution of Ih and HCN channels in murine spiral ganglion neurons. Abstr Assoc Res Otolaryngol 35:1026.

Liu W, Davis RL (2014) Calretinin and calbindin distribution patterns specify subpopulations of type I and type II spiral ganglion neurons in postnatal murine cochlea. J Comp Neurol 522:2299–2318.

Lv P, Wei D, Yamoah EN (2010) Kv7-type channel currents in spiral ganglion neurons: involvement in sensorineural hearing loss. J Biol Chem 285:34699–34707.

Mann ZF, Kelley MW (2011) Development of tonotopy in the auditory periphery. Hear Res 276:2–15.

Markram H, Toledo-Rodriguez M, Wang Y, Gupta A, Silberberg G, Wu C (2004) Interneurons of the neocortical inhibitory system. Nat Rev Neurosci 5:793–807.

Marmigère F, Ernfors P (2007) Specification and connectivity of neuronal subtypes in the sensory lineage. Nat Rev Neurosci 8:114–127.

McLean WJ, Smith KA, Glowatzki E, Pyott SJ (2009) Distribution of the Na,K-ATPase alpha subunit in the rat spiral ganglion and organ of corti. J Assoc Res Otolaryngol 10:37–49.

Meyer AC, Frank T, Khimich D, Hoch G, Riedel D, Chapochnikov NM, Yarin YM, Harke B, Hell SW, Egner A, Moser T (2009) Tuning of synapse number, structure and function in the cochlea. Nat Neurosci 12:444–453.

Meyers JR, MacDonald RB, Duggan A, Lenzi D, Standaert DG, Corwin JT, Corey DP (2003) Lighting up the senses: FM1-43 loading of sensory cells through nonselective ion channels. J Neurosci 23:4054–4065.

Ming G-L, Brüstle O, Muotri A, Studer L, Wernig M, Christian KM (2011) Cellular reprogramming: recent advances in modeling neurological diseases. J Neurosci 31:16070–16075.

Mo Z li, Davis RL (1997) Endogenous Firing Patterns of Murine Spiral Ganglion Neurons. J Neurophysiol:1294–1305.

Mojumder DK, Wensel TG, Frishman LJ (2008) Subcellular compartmentalization of two calcium binding proteins, calretinin and calbindin-28 kDa, in ganglion and amacrine cells of the rat retina. Mol Vis 14:1600–1613.

Mou K, Adamson CL, Davis RL (1998) Time-Dependence and Cell-Type Specificity of Synergistic neurotrophin Actions on Spiral Ganglion Neurons. J Comp Neurol 402:129–139.

Müller M, von Hünerbein K, Hoidis S, Smolders JWT (2005) A physiological place-frequency map of the cochlea in the CBA/J mouse. Hear Res 202:63–73.

Nägerl UV, Novo D, Mody I, Vergara JL (2000) Binding kinetics of Calbindin-D28k determinedby flash photolysis of caged Ca. Biophys J 79:3009–3018.

Nayagam BA, Muniak MA, Ryugo DK (2011) The spiral ganglion: connecting the peripheral and central auditory systems. Hear Res 278:2–20.

Nishimura K, Weichert RM, Liu W, Davis RL, Dabdoub A (2014) Generation of induced neurons by direct reprogramming in the mammalian cochlea. Neuroscience 275:125–135.

Pack AK, Slepecky NB (1995) Cytoskeletal and calcium-binding proteins in themammalian organ of Corti: cell type-specific proteins displaying longitudinal and radial gradients. Hear Res 91:119–135.

Pang ZP, Yang N, Vierbuchen T, Ostermeier A, Fuentes DR, Yang TQ, Citri A, Sebastiano V, Marro S, Südhof TC, Wernig M (2011) Induction of human neuronal cells by defined transcription factors. Nature 476:220–223.

Puligilla C, Dabdoub A, Brenowitz SD, Kelley MW (2010) Sox2 induces neuronal formation in the developing mammalian cochlea. J Neurosci 30:714–722.

Reale RA, Imig TJ (1980) Tonotopic organization in auditory cortex of the cat. J Comp Neurol 192:265–291.

Reed-Geaghan EG, Maricich SM (2011) Peripheral somatosensation: a touch of genetics. Curr Opin Genet Dev 21:240–248.

Reid MA, Flores-Otero J, Davis RL (2004) Firing patterns of type II spiral ganglion neurons in vitro. J Neurosci 24:733–742.

Robertson D (1984) Horseradish peroxidase injection of physiologically characterized afferent and efferent neurones in the guinea pig spiral ganglion. Hear Res 15:113–121.

Robles L, Ruggero MA (2001) Mechanics of the mammalian cochlea. Physiol Rev 81:1305–1352.

Romand R, Sobkowicz H, Emmerling M, Whitlon D, Dahl D (1990) Patterns of neurofilament stain in the spiral ganglion of the developing and adult mouse. Hear Res 49:119–125.

Rouaux C, Arlotta P (2013) Direct lineage reprogramming of post-mitotic callosal neurons into corticofugal neurons in vivo. Nat Cell Biol 15:214–221.

Rouiller EM, Cronin-Schreiber R, Fekete DM, Ryugo DK (1986) The central projections of intracellularly labeled auditory nerve fibers in cats: an analysis of terminal morphology. J Comp Neurol 249:261–278.

Ruggero MA (1992) Physiology and coding of sound in the auditory nerve. In: The Mammalian auditory pathway: Neurophysiology (Popper AN, Fay RR, eds), pp 34–93. New York: Springer-Verlag.

Rutherford MA, Chapochnikov NM, Moser T (2012) Spike Encoding of Neurotransmitter Release Timing by Spiral Ganglion Neurons of the Cochlea. J Neurosci 32:4773–4789.

Ryugo DK (1992) The auditory nerve: peripheral innervation cell body:morphology. In: The mammalian auditory pathway: neuroanatomy (Popper AN, Fay RR, Webster DB, eds). New York: Springer-Verlag.

Ryugo DK, Rouiller EM (1988) Central projections of intracellularly labeled auditory nerve fibers in cats: morphometric correlations with physiological properties. J Comp Neurol 271:130–142.

Schurmans S, Schiffmann SN, Gurden H, Lemaire M, Lipp HP, Schwam V, Pochet R, Imperato A, Böhme G a, Parmentier M (1997) Impaired long-term potentiation induction in dentate gyrus of calretinin-deficient mice. Proc Natl Acad Sci U S A 94:10415–10420.

Schwaller B, Meyer M, Schiffmann S (2002) "New" functions for "old" proteins: the role of the calcium-binding proteins calbindin D-28k, calretinin and parvalbumin, in cerebellar physiology. Studies with knockout mice. Cerebellum 1:241–258.

Schwartz AM, Parakkal M, Gulley RL (1983) Postnatal development of spiral ganglion cells in the rat. Am J Anat 167:33–41.

Shibata R, Nakahira K, Shibasaki K, Wakazono Y, Imoto K, Ikenaka K (2000) A-type K+ current mediated by the Kv4 channel regulates the generation of action potential in developing cerebellar granule cells. J Neurosci 20:4145–4155.

Slepecky NB (1996) Structure of the mammalian cochlea. In: The cochlea (Dallos P, Popper AN, Fay RR, eds). New York: Springer-Verlag.

Taberner AM, Liberman MC (2009) Response Properties of Single Auditory Nerve Fibers in the Mouse. J Neurophysiol 93:557–569.

Takahashi K, Yamanaka S (2006) Induction of pluripotent stem cells from mouse embryonic and adult fibroblast cultures by defined factors. Cell 126:663–676.

Toesca A (1996) Central and peripheral myelin in the rat cochlear and vestibular nerves. Neurosci Lett 221:21–24.

Tritsch NX, Rodríguez-Contreras A, Crins TTH, Wang HC, Borst JGG, Bergles DE (2010) Calcium action potentials in hair cells pattern auditory neuron activity before hearing onset. Nat Neurosci 13:1050–1052.

Verheugen J a, Fricker D, Miles R (1999) Noninvasive measurements of the membrane potential and GABAergic action in hippocampal interneurons. J Neurosci 19:2546–2555.

Vierbuchen T, Ostermeier A, Pang ZP, Kokubu Y, Südhof TC, Wernig M (2010) Direct conversion of fibroblasts to functional neurons by defined factors. Nature 463:1035–1041.

Von Békésy G (1970) Travelling waves as frequency analysers in the cochlea. Nature 225:1207–1209.

Von Neumann J (1958) The computer and the brain. New Haven, CT: Yale University Press.

Wässle H (2004) Parallel processing in the mammalian retina. Nat Rev Neurosci 5:747–757.

Wei D, Jin Z, Järlebark L, Scarfone E, Ulfendahl M (2007) Survival, synaptogenesis, and regeneration of adult mouse spiral ganglion neurons in vitro. Dev Neurobiol 67:108–122.

Weisz C, Glowatzki E, Fuchs P (2009) The postsynaptic function of type II cochlear afferents. Nature 461:1126–1129.

Wong AB, Jing Z, Rutherford MA, Frank T, Strenzke N, Moser T (2013) Concurrent maturation of inner hair cell synaptic Ca2+ influx and auditory nerve spontaneous activity around hearing onset in mice. J Neurosci 33:10661–10666.

Zhou Q, Brown J, Kanarek A, Rajagopal J, Melton DA (2008) In vivo reprogramming of adult pancreatic exocrine cells to beta-cells. Nature 455:627–632.